A comprehensive understanding on the anionic redox chemistry of high-voltage cathode materials for high-energy-density lithium-ion batteries†

Qingyuan Li, ‡[a] Dong Zhou,‡[b] Mihai Chu,[c] Zhongqing Liu,[d] Liangtao Yang, [e] Wei Wu,[e] De Ning,[e] Wenyuan Li, [a] Xingbo Liu, [a] Jie Li, *[c] Stefano Passerini *[fh] and Jun Wang *[g]

The electrification of transportation is an important contributor to reducing global carbon dioxide emissions. However, this progress is constrained by anxiety regarding the driving range of vehicles, which is well recognized to originate from the low specific energy of the employed state-of-the-art energy storage devices. Therefore, further promoting the specific energy of lithium-ion batteries (LIBs) is an inevitable need, where the development of cathode materials with high energy densities, *i.e.* high specific capacity and/or high working voltage, is essential. Accordingly, numerous research efforts are ongoing worldwide, where several materials stand out, including $LiCoO_2$ (LCO), Ni-rich oxides and Li-rich cathodes, mainly because of their potential to deliver high capacities when operating at high voltages. However, the elevated operating voltage turns out to be a double-sided sword for these materials as achieving high specific capacity is always accompanied by the oxygen redox process, which shows unsatisfactory reversibility and has a significant impact on their structure stability and electrochemical performance. Consequently, understanding the failure mechanism of anionic redox chemistry and finding solutions to this issue are crucial for realizing the practical application of these high-voltage materials. Although many studies have been reported on the anionic redox chemistry of different materials, the corresponding reviews have predominantly focused on Li-rich cathode materials. Hence, the reviews on high-voltage LCO and Ni-rich oxides remain incomplete, and a unified understanding of their behavior at high voltages has not been established yet. This lack of comprehensive understanding has hindered the further development and application of high-voltage cathode materials. Thus, this review highlights the similarities and differences in the anionic redox chemistry of LCO, Li-rich and Ni-rich high-voltage cathode materials, emphasizing on a unified mechanistic picture and the related challenges and countermeasures. We aim to provide an outlook for future guidelines in material exploration with anionic redox chemistry, thus unlocking the full potential of high-voltage LIBs for diverse applications.

1. Introduction

High-voltage cathode materials have emerged as crucial components of next-generation lithium-ion batteries (LIBs), and their utilization can advance the performance of LIBs, thus facilitating the development of long-lasting powerful batteries with high energy density.[1,2] One key research focus within this domain is the anionic (oxygen) redox chemistry, commonly

[a] Benjamin M. Statler College of Engineering & Mineral Resources, West Virginia University, Morgantown, WV, 26506, USA
[b] School of Advanced Energy, Shenzhen Campus of Sun Yat-sen University, Shenzhen, 518107, P. R. China
[c] Department of Energy, Politecnico di Milano, Via Lambruschini 4, Milano, 20156, Italy. E-mail: jie1.li@polimi.it
[d] Sodium Innovation Material Technology (SIMT) Co., Ltd., Wuxi, 214142, P. R. China
[e] Shenzhen Institutes of Advanced Technology, Chinese Academy of Sciences, Shenzhen, 518055, P. R. China
[f] Austrian Institute of Technology (AIT), Center for Transport Technologies, Giefinggasse 2, Wien, 1210, Austria. E-mail: stefano.passerini@ait.ac.at
[g] School of Innovation and Entrepreneurship, Southern University of Science and Technology, Shenzhen, 518055, P. R. China. E-mail: wangj9@sustech.edu.cn
[h] Karlsruhe Institute of Technology (KIT), Helmholtz Institute Ulm (HIU), Helmholtzstr. 11, Ulm, 89081, Germany

‡ These authors contributed equally to this work.

appearing at high voltages, which leads to relatively poor reversiblility.[3 6] Thus, understanding the intricacies of the related reactions and finding effective strategies to promote their electrochemical performance are essential for the rational design of high-voltage cathode materials.[7 10]

In recent years, considerable efforts have been directed towards elucidating the reaction mechanisms governing the oxygen redox process in high-voltage LIB cathodes.[11 14] The discovery and analysis of these underlying details are instrumental in overcoming the challenges such as voltage decay, voltage hysteresis, and capacity fading associated with high-voltage operation. A systematic summary of the most recent mechanistic research advances and issues faced by high-voltage LIB cathodes toward their commercialization is important to accelerate their development. Unfortunately, this is still lacking as most relevant review articles focus on the anionic redox mechanism of Li-rich cathodes,[3,4] while scarce information on the anionic redox characteristics in the other two high-voltage cathode material families (LCO and Ni-rich oxides) are available. This originates from the controversy in the detailed reaction mechanisms of anionic redox reactions in LCO.[15 17] In addition, there is no in-depth overview on the interrelationship among mechanisms from different materials and the various mechanisms from an individual material. For example, the Li–O–Li configuration in high-voltage Li-rich cathode materials can act as a messenger for the anionic redox process, while the O_2 molecule in the crystal bulk is the cause of voltage hysteresis in Li-rich cathodes.[11,18] However, similar mechanistic studies in

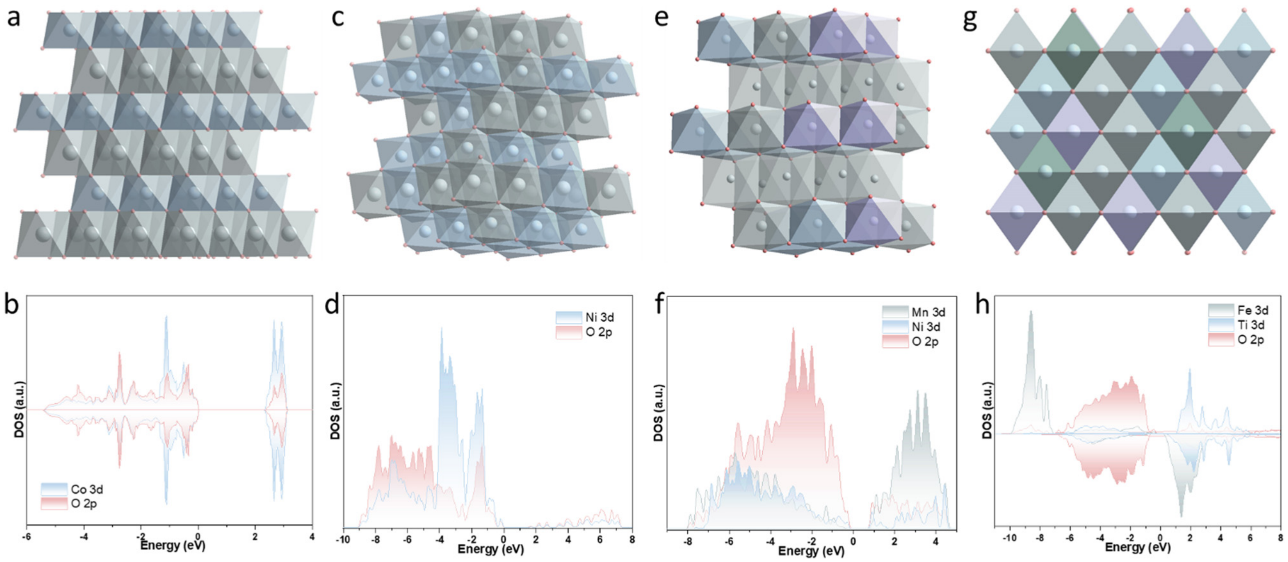

Fig. 1 Crystal structures and electronic structures of LCO (a) and (b), Ni-rich (LNO) (c) and (d), layered Li-rich (e) and (f) and cation-disordered rock-salt Li-rich (g) and (h). In the crystal structure images, light blue dots represent the transition metal cobalt (a), nickel (c) and (e) and iron (g); grey dots represent Li; and light purple dots represent transition metal manganese (e) and titanium (g). Panel (b) Reproduced with permission.[20] Copyright 2022, Wiley. Panel (d) Reproduced with permission.[23] Copyright 2023, Springer Nature. Panel (f) Reproduced with permission.[24] Copyright 2021, Springer Nature. Panel (h) Reproduced with permission.[25] Copyright 2021, Springer Nature.

Li-rich cathodes are rarely mapped in the other two types of high-voltage cathode materials.

Therefore, herein, we present a timely review and integrate the mechanistic advances of anionic redox chemistry in these three high-voltage cathode material families, including their commonalities and differences, to supply a unified picture of the anionic redox reaction path. Initially, the structural characteristics and latest redox mechanisms of high-voltage LCO, Li-rich and Ni-rich cathode materials are introduced. Then, the challenges and strategies to address them are described based on their respective characteristics. Lastly, high-throughput calculations for the design of high-voltage cathode materials are emphasized. We believe that this review will serve as a guideline in the future development of high-voltage cathodes with anionic redox activities for high-energy-density LIBs, supporting the acceleration of their practical application.

2. Structural characteristics of high-voltage cathode materials

LCO, with an α-$NaFeO_2$ layered structure and $R\bar{3}m$ space group, was first reported in 1958. It has an O3-type cubic-close-packed framework with Li and Co ions separately located in alternate layers (Fig. 1a).[19] LCO has a relatively simple band structure (Fig. 1b),[20] with its conduction and valence bands being mainly formed by the mixing of Co 3d and O 2p orbital. This results in a relatively high electronic conductivity, facilitating rapid electron migration inside LCO during the charge and discharge processes. LCO was utilized as the cathode material for the first commercialized LIBs in 1991. However, although its theoretical capacity reached 274 mA h g^{-1}, the charging voltage in practical applications is generally controlled at ≈4.2 V, ultimately leading to a sharp decline in capacity to 140 mA h g^{-1} because of the structural instability and irreversible oxygen redox process occurring at high voltages. Therefore, efforts to advance the practical capacity of LCO materials, raising their upper cut-off voltage, are still ongoing. For example, by increasing the cut-off voltage to 4.6 V, the discharge capacity of LCO was improved to 161 mA h g^{-1} in 2011,[21] and then a substantial increase in capacity to more than 190 mA h g^{-1} was achieved by La and Al co-modification in 2018.[22]

Taking layered LCO as the parental archetype, Co-free Ni-rich oxide ($LiNiO_2$, LNO) was studied as a cathode material in 1993. Differing from LCO, Li/Ni mixing is observed in LNO material (see Fig. 1c).[26] Its electronic structure also varies compared with LCO (Fig. 1d). The interaction of its Ni 3d with O 2p orbitals is weaker, and thus LNO can deliver a higher capacity than LCO within the same voltage range.[23] However, LNO has not been implemented in commercial cells due to its poor compatibility with the conventional electrolyte and the collapse of its bulk structure during delithiation. In 2001, Ohzuku and Makimura first reported the synthesis of $LiNi_{1/3}Co_{1/3}Mn_{1/3}O_2$ layered oxide, which displayed a reversible capacity exceeding 200 mA h g^{-1} in the voltage range of 3.5–5.0 V, although with a poor cycling performance.[27] Subsequently, ternary layered oxides $LiMO_2$ (M: metal, M = Ni, Co, Mn), the so-called NCM cathodes, were extensively studied. The high Ni content (Ni-rich) cathode materials show great promise because of their high practical capacities delivered even at lower upper cut-off voltages (*e.g.* 4.3 V). Similar to LNO, a common issue in NCM materials is the strong Li/Ni mixing originating from the migration of highly active Ni^{3+} or Ni^{2+} into the Li layers, especially at high voltage. Li/Ni mixing facilitates the formation of the rock-salt phase, which can prevent the diffusion of Li ions and degrade the performance. In general, within the same operating voltage range, ternary cathode materials with a low nickel content show better cycle stability, while that with high nickel contents have higher capacity, but at the cost of structural stability and cycle life. It is worth noting that Co^{3+} in the low spin state ($t_{2g}^6e_g^0$) without unpaired electrons is beneficial to suppress Li/Ni mixing in Ni-rich cathode materials due to the reduction in magnetic frustration.[28] Therefore, retaining the appropriate state of cobalt in Ni-rich cathode materials is conducive to enhancing the battery performance.

Besides the materials with the shared formula of $LiMO_2$, another type of layered cathodes, the so-called layered manganese-based Li-rich oxides (LM-LROs), has also been studied intensively as high voltage cathode materials. LM-LROs can be seen as an intimate mixture of two oxides, Li_2MnO_3 (space group: $C2/m$) and $LiMO_2$ (space group: $R\bar{3}m$) phases, both belonging to an α-$NaFeO_2$ structure. They are detected in the same region (Fig. 1e) given that the (001) interplanar spacing of monoclinic Li_2MnO_3 and the (003) interplanar spacing of trigonal $LiMO_2$ are both ≈ 4.7 Å.[29] Based on experimental results, researchers have proposed two models to explain the complex structure of LM-LROs. One view proposes LM-LRO as a single-phase solid solution (single monoclinic structure[30] or pure hexagonal phase[31]). The other expresses the material according to the structural formula $xLi_2MnO_3{\cdot}(1-x)LiMO_2$. Due to the presence of a hexagonal $LiMn_6$ honeycomb superstructure in transition metal layers, some weak and broad peaks can be observed in the 2θ range of 20–30° in the X-ray diffraction (XRD) pattern of this type of material, proving the existence of the Li_2MnO_3 structure.[32,33] LM-LROs exhibit a more complex electronic structure, often composed of the mixing of transition metal and oxygen bands, as shown in Fig. 1f, in which the transition metals are represented by Mn and Ni.[24] Furthermore, due to the presence of multiple oxidation states, they display a significant contribution from oxygen ions to the electronic structure, which is crucial for their high capacity during electrochemical cycling. The high capacity of LM-LROs was first disclosed by Lu *et al.* in 2001 during their study on $Li_{1.1}Ni_{0.3}Mn_{0.6}O_2$,[34] from which 220 mA h g^{-1} was delivered in the voltage range of 2.0–4.6 V at 55 °C. Then, the capacity was further increased gradually by tailoring the material composition, including Li content, choice of transition metals and their ratio. Recent work on an O2-type layered $Li_{1.25}Co_{0.25}Mn_{0.50}O_2$ reported a reversible capacity of >400 mA h g^{-1} and energy density of ≈ 1360 W h kg^{-1} when the electrode was cycled in the voltage range of 2.0–4.8 V.[35] However, the inherent complexity of these oxides results in structural instability during cycling, which negatively impacts their performance. Other layered Li-rich oxides employing 4d or 5d transition metals, such as Li_2IrO_3,[36,37] Li_2RuO_3[38] and Li_2MoO_3,[39] have also been developed because of the inherent simplicity of their structure and composition. In this case, although their high cost prevents their commercial application, studies on these materials are beneficial for enriching the knowledge on the electrochemical reaction mechanisms in layered Li-rich oxide cathode materials. In general, all layered Li-rich oxides suffer from the problems of continuous voltage decay and hysteresis during cycling, which need to urgently be addressed. Given the structural complexity discussed above, to facilitate the subsequent analysis of the reaction mechanisms in LM-LROs, herein we adopt the widely accepted two-phase coexistence model, represented as $xLi_2MnO_3{\cdot}(1-x)LiMO_2$.

Finally, in addition to ordered layered Li-rich oxides, cation-disordered rock-salt transition metal oxides (DRXs) also show potential to be employed as high-voltage cathodes. DRXs are receiving increasing attention due to their improved structural stability (*vs.* ordered layered Li-rich oxides) during electrochemical cycling.[40 47] They have a similar chemical composition to the conventional LM-LROs, with the chemical formula of $Li_{1+x}M_{1-x}O_2$. The difference is that the cations of DRXs are in a disordered arrangement between the Li and M sublattice sites.[41,48] DRXs form an NaCl-like structure with the $Fm\bar{3}m$ space group, where the anions occupy the 4*b* sites in the face-centered cubic sublattice, and the cations (Li and TM) are randomly distributed at the 4*a* sites, as displayed in Fig. 1g ($Li_{1.17}Ti_{0.33}Fe_{0.5}O_2$ is presented as an example).[25,49] It has long been considered that oxides with this close-packed structure are electrochemically inert due to their lack of Li^+ diffusion channels.[49] Also, the complex electronic structure and strong localization effect resulting from the disordered arrangement of cations further restrict the movement of charge carriers (Fig. 1h).[25] Interestingly, this traditional perception was broken by a study on $Li_{1.211}Mo_{0.467}Cr_{0.3}O_2$ DRX, which demonstrated a high specific capacity of ≈ 266 mA h g^{-1} and a high energy density of ≈ 660 W h kg^{-1}.[41] To explain this anomaly, Ceder *et al.* proposed the percolation theory of Li^+ ion transmission in DRXs by *ab initio* computations.[50,51] According to this theory, 0/1/2-M is used to represent the number of M in the MO_6 octahedron that shares faces with the activated tetrahedral sites.[41] Given that in DRXs, the Li^+ ions generally hop from the LiO_6 octahedron to the tetrahedral vacancy, and then to the adjacent octahedral position (*o*–*t*–*o*) during delithiation, obviously DRXs with 0-M and 1-M channels are electrochemically active. The 0-M channel offers the smallest Li^+ ion migration barrier compared to the 1-M and 2-M channels due to the slightest electrostatic repulsion between the activated tetrahedral Li^+ and face-shared octahedral Li^+ ions. The percolation theory broadens the understanding of Li^+ ion diffusion, indicating that especially the 0-M channel plays a decisive role in DRXs. Therefore, the formation of a percolation network with 0-M channel is extremely important for this type of material. Monte Carlo simulations illustrated that a percolation network with 0-M channel could only be formed when the lithium content exceeded 1.09 in non-high entropy $Li_{1+x}M_{1-x}O_2$ DRXs.[41]

Obviously, the material structure, voltage range, current density, *etc.* strongly influence the electrochemical performance of the aforementioned high-voltage cathode materials, as summarized in Table 1. To deeply understand the origins of their different electrochemical behaviors, a good understanding of their working mechanism can play a key role, which will be discussed in the following section.

3. Working mechanisms of various high-voltage cathode materials

3.1 Working mechanisms of high-voltage Li-rich cathodes

High-voltage LM-LROs can deliver ultra-high specific capacities, which even exceed the theoretical capacities calculated based on the conventional cationic redox. Therefore, this has inspired numerous fundamental studies, and a range of working mechanisms has been proposed, such as oxygen release, formation of oxygen radicals and surface reactions.[29,70 74] Among the different mechanisms, there is a widely accepted concept, *i.e.*, the participation of oxygen redox in the charge compensation. A certain aspect of the Li_2MnO_3 activation process during charging has been explained. However, due to the structural and compositional complexities of LM-LROs, the understanding of charging at high voltage, in particular, the relationship between high capacity and structural stability still needs further study. In the case of the Co-free $0.5Li_2MnO_3{\cdot}0.5LiMn_{0.5}Ni_{0.5}O_2$ cathode material, prior to the charging plateau (typically 4.5 V), Li^+ ions are predominantly extracted from the $LiMn_{0.5}Ni_{0.5}O_2$ layered structure, accompanied by the oxidation of Ni^{2+} and potentially the oxidation of a minor residual amount of Mn^{3+}. Beyond 4.5 V, further delithiation occurs within the Li_2MnO_3 structure, accompanied by the migration of Mn, with charge compensation primarily facilitated through the redox activity of oxygen ions. During the initial discharge, Li^+ ions intercalate back to the lattice, and the activated transition metals are reduced, *e.g.*, Ni^{4+} to Ni^{2+}. Meanwhile, partial Mn^{4+} in the structure decreases to Mn^{3+}, together with, in principle, only one Li^+ per formula inserting into the delithiated structure, while the electrochemical activation process removes more than one Li, which means capacity loss and low coulombic efficiency. It is worth noting that in most LM-LROs, the 2nd charge voltage is obviously different from the initial one at a low current density, demonstrating that the activation of the material only occurs during the initial cycle.

Despite its unsatisfactory reversibility, the oxygen redox clearly contributes to the super-high capacities of LM-LROs.[75] This is actually the general case in high-voltage Li-rich oxides, not only in LM-LROs but also in DRXs and others, when the applied cut-off voltage is higher than 4.5 V. Thus, the M–O covalency needs to be deeply discussed to elucidate the origin of the oxygen redox in high-voltage Li-rich oxides. In the case of the M octahedral coordination, as illustrated in Fig. 2a, the d orbitals of the central transition metal ions are split into e_g and t_{2g} bands. The interaction between the e_g band and the ligand p orbitals results in the formation of an e_g bonding state with a

Table 1 Comparative analysis of the electrochemical performance of high-voltage cathodes with different structures

Optimized cathode	Structure	Voltage range (V)	Energy density (W h kg^{-1})	Current density (mA g^{-1})	Highest capacity (mA h g^{-1})	Cycle No.	Capacity retention (%)	Ref.
$Li_{1.2}Mn_{0.6}Ni_{0.2}O_2$	O3 layered	2.0–4.8	≈900	250	201	200	100	52
$Li_{1.20}Ni_{0.36}Mn_{0.44}O_2$		2.0–4.7	≈800	67	221	200	84.8	53
$Li_{1.2}Mn_{0.6}Ni_{0.2}O_2$		2.0–4.8	≈900	250	257	200	92	54
$Li_{1.2}Mn_{0.54}Ni_{0.13}Co_{0.13}O_2$		2.0–4.8	≈980	25	282.1	100	97.6	55
$Li_{1.2}Mn_{0.54}Ni_{0.13}Co_{0.13}O_2$		2.1–4.6	—	250	≈235	400	80	56
$Li_{1.17}Ni_{0.21}Mn_{0.55}Co_{0.07}O_2$		2.0–4.8	800.4	50	242.1	700	96.5	57
$Li_{1.25}Co_{0.25}Mn_{0.5}O_2$	O2 layered	2.0–4.8	1360	80	225	50	90	35
$Li_{1.1}Ni_{0.21}Mn_{0.65}Al_{0.04}O_2$		2.0–4.7	836	67	248	50	96	58
$Li_x(Li_{0.15}Ni_{0.23}Mn_{0.62})O_2$		2.0–4.6	660.9	20	220	100	89	59
$Li_{1.05}Mn_{0.85}Ti_{0.1}O_2$	Rock-salt	1.5–5.0	826	20	288.6	100	85	60
$Li_{1.2}Mn_{0.6}Ti_{0.2}O_{1.8}F_{0.2}$		1.5–4.8	754	16.05	251	200	82	61
$Li_{1.2}Cr_{0.4}Mn_{0.4}O_2$		2.0–4.6	>1100	20	>360	30	—	62
$LiNi_{0.82}Mn_{0.10}Co_{0.08}O_2$	O3 layered	2.0–4.7	≈893	—	235	100	92	63
$LiNi_{0.8}Mn_{0.1}Co_{0.1}O_2$		2.5–4.5	800	100	≈202	200	75.3	64 and 65
$LiNi_{0.82}Co_{0.15}Mn_{0.03}O_2$		2.8–4.7	≈842	200	168.35	80	72	66
$LiCo_{1-x-y-z}Al_xMg_yZr_zO_2$	O3 layered	3.0–4.6	≈685	400	≈175	1400	80	67
$LiMg_xNi_{1-x}PO_4$@LCO		3.0–4.7	≈858	137	220	200	78	68
$LiCoO_2$		2.8–4.4	≈695	—	≈180	500	97	69

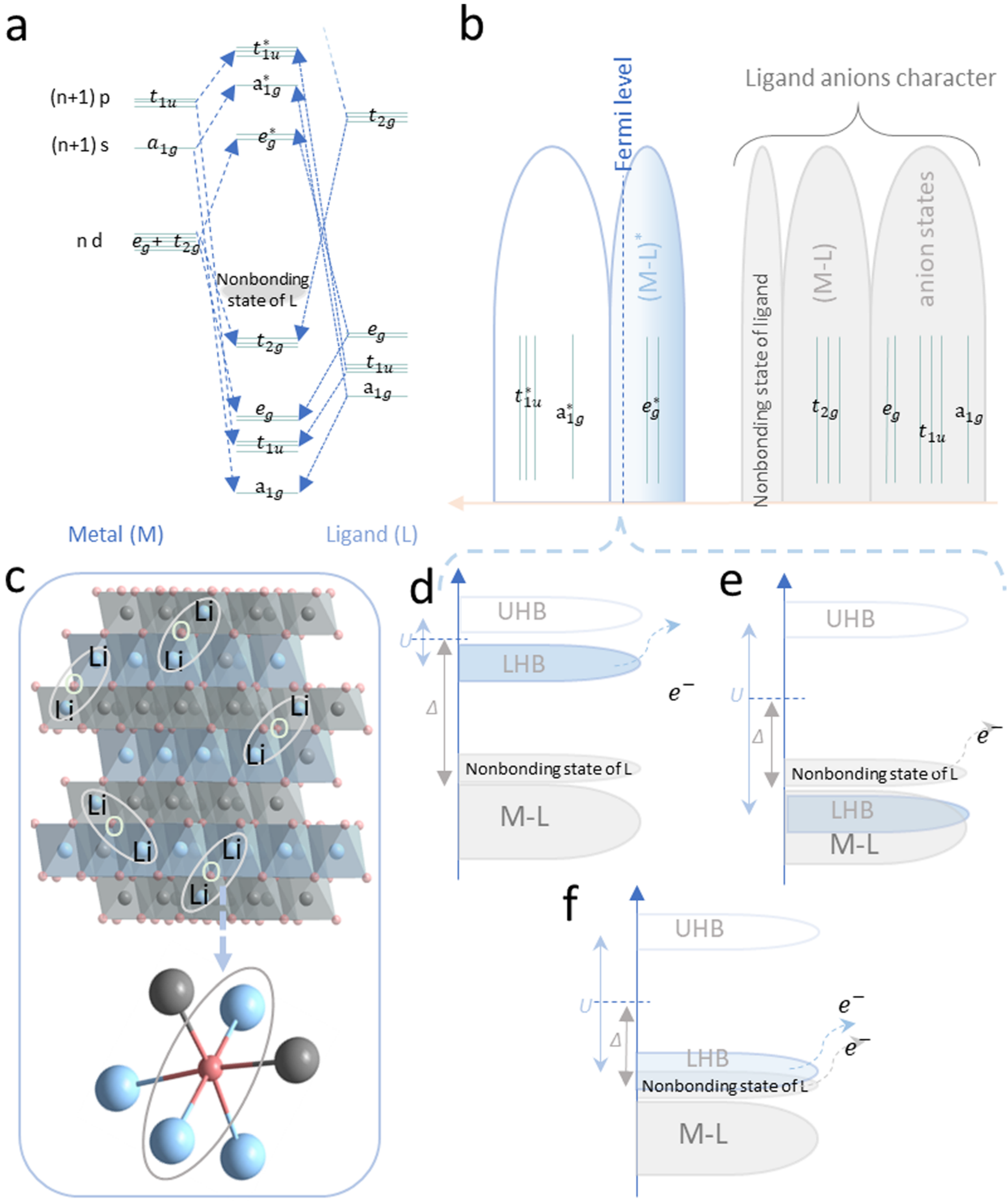

Fig. 2 (a) Band structures of a typical octahedral complex. (b) Schematic of band structure of transition metal oxide. (c) Li–O–Li crystal structure formed by the mixed arrangement of lithium and transition metals causing anionic redox reactions. (d)–(f) Schematic of three subdivided band structures, and their corresponding representative crystal structures when Mott–Hubbard splitting is introduced. Term U is the d–d Coulomb repulsion and term Δ denotes the charge transfer. They represent the anion-free redox mechanism, irreversible anionic redox mechanism, and reversible anionic redox mechanism, respectively.

lower energy and e_g^* anti-bonding state with a higher energy. In addition, there is usually an existing nonbonding state due to the lack of direct overlap between the t_{2g} band and ligand p orbital. Furthermore, the $(n + 1)$ s and $(n + 1)$ p states of the central transition metals will overlap with the p orbitals of the ligand to form a_{1g} and t_{1u} bands. In short, the nonbonding state, bonding e_g, a_{1g} and t_{1u} bands are commonly considered to have ligand characteristics due to their higher electronegativity and lower energy. More specifically, as shown in Fig. 2b, the degenerate Fermi level is split into two similar energy bands, the ligand O 2p band (grey) and the M d band (light blue), due to the covalent nature of M–O, where holes higher than the Fermi level and electrons lower than the Fermi level can form a redox pair. In covalent transition metal oxides containing alkali metals or alkaline earth metal elements, the overlap of the ligand O 2p band and M d bands will result in the formation of bonding bands (M–L) and anti-bonding bands (M–L)*. The energy difference between the bonding band and the anti-bonding band is called the charge transfer term Δ, which is determined by the electronegativity difference between M and the ligand.

In the case of common layered oxides, $LiMO_2$, the redox reaction is only related to the anti-bonding band (M–O)* (also called the d band), while the anion does not participate, and thus it is called a cationic redox process. Different from $LiMO_2$, there is a non-bonded state of oxygen in Li-rich oxides. Specifically, the Lewis configuration of O^{2-} contains one 2s and three 2p doublets. In this configuration, the 2s orbital does not have redox activity given that it is deeply buried under the bonding band (M–O). The three 2p orbitals of oxygen have different contributions to the formation of M–O bonds, according to the configuration of transition metal oxides. In the common layered oxides $LiMO_2$ (O/M = 2, molar ratio), all three 2p orbitals participate in bonding with transition metals. In the case of Li_2MnO_3 (O/M = 3, molar ratio), only two 2p orbitals participate in bonding with transition metals and the other 2p orbital is located above the M–O bonding band, *i.e.*, towards Li, but seldom overlaps with the Li 2s orbital. The O non-bonding states become more prevalent; therefore, the O 2p density of states increases as the O/M value increases.[76,77] It is worth noting that the O non-bonding state has different names in the literature, such as "unhybridized" or "orphaned" O 2p state, "O lone-pair", "b_1* state" in C_{2v} point-group symmetry and "Li–O–Li" configuration (Fig. 2c).[3,18,78–81] This is very important because besides the antibonding (M–O)* band in some oxides that contribute to capacity during charge/discharge, the O 2p non-bonding band between the antibonding and bonding bands can also aid in charge compensation. Unlike the antibonding band, these non-bonding bands enable charge compensation without removing electrons from the bonding (M–O) band, thus offering extra reversible capacity.

It should be noted that particular conditions are required to achieve redox between the anti-bonding band and the O 2p non-bonding band. Therefore, in addition to the above-mentioned charge transfer term Δ, another solid-state physics concept is introduced, namely, the d–d Coulomb interaction term U. The d–d Coulomb interaction splits the partially filled anti-bonding band (M–O)* into two parts (called Mott–Hubbard splitting), the empty upper Hubbard bands (UHB) and the filled lower Hubbard bands (LHB), as shown in Fig. 2d–f. It should be noted that U is inversely proportional to the orbital volume and is related to the different d orbitals of different metals. For example, the U value increases from left to right of the periodic table owing to the orbital contraction in the fourth period. Similarly, it becomes smaller for transition metals of the same group from 3d to 5d. The charge transfer Δ is proportional to the electronegativity, for example, the value of Δ will decrease by using S to replace O.[82] Therefore, based on the relative magnitude of the d–d Coulomb interaction U and charge transfer Δ, there are three types of redox reactions between the LHB and O 2p non-bonding band. When $U \ll \Delta$, electrons are completely extracted from the filled LHB during the charging process, which is a typical cation redox reaction for common oxides and fluorides. When $U \gg \Delta$, the electrons are only removed from the O 2p non-bonding band above the filled LHB. Then, the remaining high-activity O^{n-} products are eliminated from the crystal lattice after being reduced by reacting with the electrolyte. This leads to a partly irreversible redox process, such as a change in the plateau for high-voltage Li-rich oxides in the first cycle.[83–87] Although the initial band is modified by the release of O in Li-rich oxides, this is conducive to the reversibility of the redox process and the formation of O–O dimers. Finally, when $U \approx 2\Delta$, the filled LHB and O 2p non-bonding band overlap, enabling both anions and cations to undergo redox reactions to provide capacity. When electrons are removed from these oxides, anion and cation redox reactions will result in unstable, degenerate Fermi levels. Thus, to overcome this instability, the degree of degeneracy would be increased by Jahn–Teller or Peierls distortion. The structural symmetry is reduced to stabilize the $M–O_2{}^{n-}$ reaction during the distortion process by the rearrangement of lattice oxygen and the shortening of the O–O bond length.[78] The distortion of the MnO_6 octahedron has been verified in the literature,[38,84,88] and the stabilizing effect of this superoxide-like O–O dimer can be elucidated by the reduction coupling mechanism.[89]

Doublet *et al.* theoretically clarified the working mechanism of the anionic redox reactions.[77,78] The electrons are removed from the O 2p non-bonding band located above the filled LHB, resulting in the formation of an O–O dimer and highly active O^{n-} substances. Meanwhile, the O 2p non-bonding band splits into σ, π, π* and σ* discrete bands, as shown in Fig. 3, in which the bottom abscissa represents the shortening of the O–O bond length, indicating that $(O–O)^{n-}$ is oxidized or the anion reaction capacity is enhanced (shown on the upper abscissa). In the calculations, there is a principle that the $(O–O)^{n-}$ species is stable provided that its highest occupied state lowers the unoccupied transition metal band. Based on this criterion, the reversibility of the anionic redox can be predicted through the relative magnitude of Δ_{CT} (the difference between UHB and O 2p non-bonding band) and the redox energies of $O^{2-}/(O_2)^{2-}$, $O^{2-}/(O_2)^{-}$ or O^{2-}/O_2. As shown by the purple area in Fig. 3, before the blue mark, $\Delta_{CT} > \Delta^{\sigma}_{O}\ {}_{O}$ (the height of the purple area is greater than that of the gray and green areas), the $(O–O)^{n-}$ product can exist stably. Therefore, the anionic redox reaction

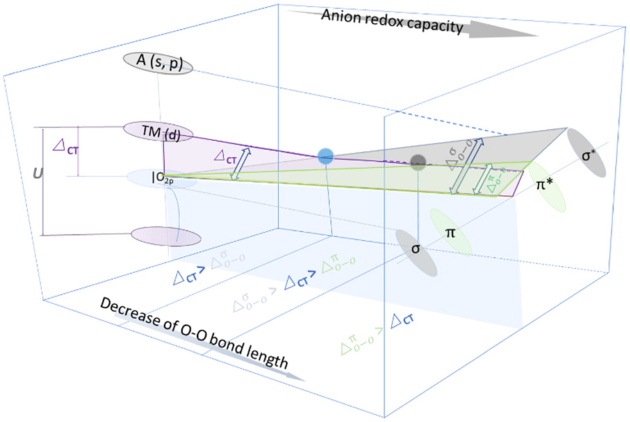

Fig. 3 Anionic redox mechanism with reversible hysteresis and irreversibility in Li-rich oxides.

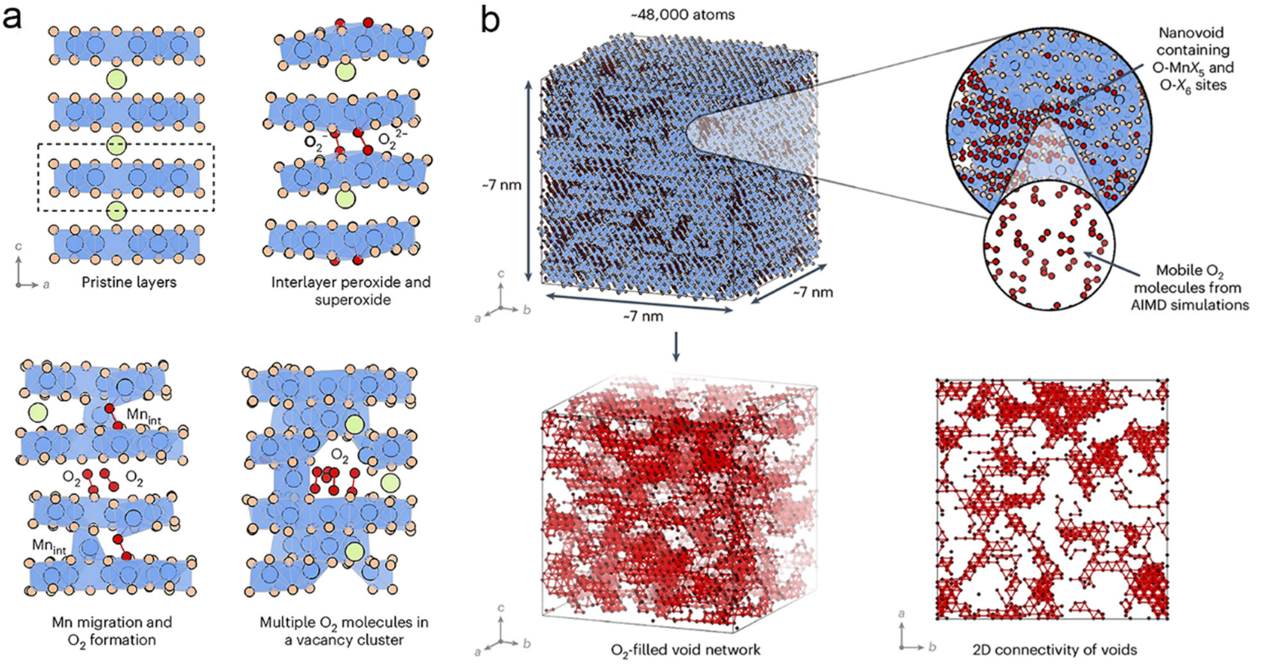

Fig. 4 Formation and transport of oxygen molecules: (a) oxygen molecules formed by the ripple movement of transition metal layers and prior to the migration of the transition metal. (b) 3D and two-dimensional (2D) transport pathways of oxygen molecules in a void network. Reproduced with permission.[99] Copyright 2024, Springer Nature.

is completely reversible according to the reduction coupling mechanism. Between the blue mark and grey round marks, $\Delta^{\sigma}_{O\ O} > \Delta_{CT} > \Delta^{\sigma}_{O\ O}$ (the height of the purple area is greater than that of the green area, but less than that of grey area), the generation of peroxide $(O_2)^{2-}$ is accompanied by voltage hysteresis, mainly because the transition metal cations are reduced first during the discharge process, followed by peroxide reduction. When the O–O bond continues to shorten and the band is located to the right of the grey round mark, $\Delta_{CT} < \Delta^{\sigma}_{O\ O}$, meaning that the height of the purple area is less than that of the green area, oxygen gas is released, accompanied by the reduction of transition metals according to the reduction elimination mechanism.[77]

The above studies discussed the mechanisms of anionic redox reactions. At the same time, the understanding of the final products of anionic redox reactions have gradually been deepened, from the initial peroxides and superoxides to the release of surface oxygen molecules,[89 96] and then the formation of bulk oxygen molecules, which has been widely accepted recently.[11,13,97,98] Islam *et al.* conducted theoretical research on the formation and transport process of oxygen molecules in the bulk phase of Li-rich oxides from kinetic and thermodynamic perspectives.[99] Firstly, it was found that the initial step in the kinetically favorable oxygen redox mechanism is interlayer O–O dimerization rather than Mn migration. This dimerization is facilitated by a ripple-like motion, which reduces the interlayer spacing between the transition metal layers, bringing the distance between certain oxygen layers to less than 1.5 Å, as shown in Fig. 4a. In addition, the theoretical analysis suggested that in the high-voltage delithiation state, the LM-LRO cathode is thermodynamically easy to decompose into manganese oxide and oxygen, regardless if the generated oxygen is released from the surface or trapped inside the crystal structure. The O_2 generated by decomposition fills the newly formed nanovoids, which range in size from approximately 0.5 nm to over 1.5 nm in length, creating a three-dimensional (3D) percolation network that connects 90% to 95% of the oxygen molecules. This network may facilitate the transport of oxygen generated at high voltage through a path that becomes significantly more tortuous compared to its initial state. At the same time, the structure is characterized by large voids filled with numerous O_2 molecules, often connected by narrow channels, which may serve as bottlenecks for oxygen transport, as shown in Fig. 4b.

3.2. Working mechanisms of high-voltage LCO material

Considering the aforementioned mechanism, the absence of non-bonding Li–O–Li configurations in LCO can be attributed to the limited presence of lithium ions within the transition metal layers. Consequently, although an oxygen redox reaction is observed in LCO during the first electrochemical cycle at high voltage, the underlying mechanisms differ significantly from that observed in Li-rich oxides. This distinction arises from the structural disparities between these two classes of cathode materials. Regarding the oxygen redox reactions in LCO, the widely accepted view is the covalence between Co and O.[15,16] This is evident from the band structure, where clear hybridization between Co and O can be observed. Charge redistribution and hybridization occur around the transition metal and O due to the movement of electrons within the hybridized band caused by Li deintercalation.[100] Concurrently, Co^{3+} is oxidized to Co^{4+} with holes in the t_{2g} orbitals, lowering the band gap and increasing the electron delocalization, thus enhancing the electronic conductivity of LCO and improving its rate performance.[101] Additionally, the departure of Li^+ ions leads to the localization of the e_g component within the O 2p hole, shielding the Li^+ charge and enhancing Li^+ diffusion, while the itinerant a_{1g} component can further improve the electronic conductivity.[102]

Researchers have experimentally demonstrated this covalent theory. Long *et al.* confirmed the presence of holes in the Co 3d and O 2p states and the enhancement of Co–O covalency through soft X-ray absorption spectroscopy (XAS).[103] Moreover, at a high charging voltage, lattice oxygen can be oxidized to form peroxo-like species (O_2^{2-}) or superoxide species (O_2^-), eventually releasing oxygen, as demonstrated by electron paramagnetic resonance (EPR)[104] and differential electrochemical mass spectrometry (DEMS).[10,68,105,106] However, it has been argued that this charge compensation arising from covalency is not a true oxygen redox because the high covalency endows the anti-bonding orbital (M–O)* band of O with redox activity, characterized by the participation of only one hybridized band in charge compensation.[3] Moreover, because M–O hybridization exists in all transition metal oxide cathodes, this covalent mechanism cannot fully explain the anion redox process in LCO.

Recently, non-gaseous O_2 molecules, typical products of oxygen redox reactions, were also detected in LCO by resonant inelastic X-ray scattering (RIXS).[17] The results show the appearance of non-elastic peaks similar to oxygen molecules in Li-rich oxides under high voltage charging in the initial electrochemical cycle. However, these peaks have low resolution and large half widths, which are not entirely consistent with previously reported results in Li-rich oxides and some sodium layered oxides. Additionally, given that significant structural rearrangement does not occur in the initial cycle of LCO, thus lacking Li–O–Li configurations, the newly appearing non-elastic peaks still need further confirmation. Although the structure of Co in the transition metal layer of LCO remains intact in the initial cycle, as the electrochemical cycle progresses, LCO transitions from a mixed H1-3 phase to a hexagonal O1 phase. Concurrently, the transition metal layer undergoes distortion, prompting the migration and dissolution of Co. This process leaves behind Co vacancies within the transition metal layer, ultimately resulting in the creation of vacancy-O–Li configurations, which fulfill the requirements of essential O 2p non-bonding states for oxygen redox reactions to occur, similar to the situation in Li-rich oxides. Therefore, it is believed that during long cycling, *i.e.*, with the accumulation of phase transitions at high voltage in LCO, vacancy/Li–O–Li O 2p non-bonding state configurations are created, which can be detected through RIXS as non-elastic peaks similar to O_2 molecules. This underscores the importance of expanding the research scope beyond merely examining alterations in the initial material structure and elucidating mechanistic explanations. It is imperative that investigators also direct their attention toward analyzing changes in stability and mechanistic processes occurring during extended cycling periods. This comprehensive approach will yield a more nuanced understanding of the material behavior and performance over time.

3.3. Working mechanisms of high-voltage Ni-rich materials

The representative charging mechanisms of oxygen redox in Ni-rich cathode materials at high voltages are M–O covalency and oxygen hole mechanisms.[107–109] The decrease in coordination between the transition metal and O leads to the redistribution of the energy states near the top of the valence band, stemming from the enhancement in the O 2p non-bonding orbitals, consequently manifesting oxygen redox reactions. Although this mechanism has been verified by XAS and low-resolution RIXS,[110] as discussed previously, the anti-bonding (M–O)* covalency merely imparts oxygen character, and the charge compensation originates from the hybridization band rather than a single oxygen band. However, it lacks sufficient precision. Moreover, the creation of holes on the O 2p bands also exemplifies the oxygen redox in Ni-rich cathodes, and is effectively illustrated by RIXS owing to its sensitivity in probing oxidized oxygen with unoccupied O 2p states. However, the newly formed peroxides/superoxides may only play an intermediate role in the oxygen redox reaction. Therefore, more details on the oxygen redox working mechanism in Ni-rich cathodes should be revealed.

Owing to advanced characterization techniques and the relatively systematic understanding of oxygen redox reactions in Li-rich oxides, a mechanism based on non-bonding O 2p states with the Li(vacancy)–O–Li configuration has been proposed in Ni-rich cathodes.[111] According to the reported studies, the O_2 molecules formed by oxygen redox are trapped in the transition metal vacancy clusters, as shown by the high-resolution RIXS.[112–114] The Ni migration and formation of 8% vacancies enable the generation of an O 2p non-bonding band with a "vacancy–O–Li" configuration, activating the oxygen redox, and facilitating Ni reorganization and formation of vacancy clusters to trap the O_2 molecules. In addition, the inherent Li/Ni mixing in Ni-rich oxides is believed to be another crucial factor in oxygen redox reactions. On one hand, the Li/Ni mixing can create O 2p non-bonding states with the Li–O–Li configuration, activating oxygen oxidization. On the other hand, it induces transition metal migration and accelerates the transition metal reorganization, consequently enabling the formation of vacancy clusters. Furthermore, although Li/Ni mixing can promote charge compensation of the oxygen anion and increase the capacity, it deteriorates the transport kinetics of Li^+ ions. Therefore, a trade-off between Li/Ni mixing and performance should be studied in future research.[115]

4. Challenges and strategies

4.1. Challenges and strategies for high-voltage Li-rich oxides

4.1.1. Voltage fading. Although high-voltage Li-rich oxides have large capacities (>250 mA h g^{-1}), their energy densities and practical application are severely restricted by the continuous voltage fading upon cycling.[4,116–118] Thus, intensive research has been devoted to understanding and alleviate the voltage attenuation. Firstly, it is highly related to the upper cut-off voltage. For example, almost no voltage fading could be observed in the $Li_{1.2}Ni_{0.13}Co_{0.13}Mn_{0.54}O_2$ material when cycled in the voltage range of 2.0–4.4 V; however, the voltage drop became obvious with an increase in the upper cut-off voltage, specially to 4.8 V, showing that the voltage decay is highly related to the activation of Li_2MnO_3 at high voltage.[119] Given that Li^+ ions are extracted from the Li_2MnO_3 component with irreversible oxygen release in the voltage range of 4.4–4.8 V,ref. 120–122 the transfer of transition metals to the Li layer is thermodynamically favoured.[84,123] Thus, new phases (densified layer) are formed on the surface, accompanied by the loss of lattice oxygen, which is widely accepted for being the cause of voltage decay.[123]

Regarding DRXs, although the migration of transition metals to the Li layer is difficult to characterize due to their random distribution in DRXs, a densified layer (rock-salt phase), similar to LM-LRO, is also formed on the particle surface, which has been deemed to be caused by the migration of transition metals and oxygen release.[124,125] In addition, by comparing $Li_{2-x}Ru_{1-y}Ti_yO_3$ and $Li_{2-x}Ru_{1-y}Sn_yO_3$, Tarascon *et al.* proved that the voltage decay is caused by the migration and trapping of cations in the tetrahedral sites of the Li layers.[126] $Li_{2-x}Ru_{1-y}Ti_yO_3$ displays more severe voltage decay because of the presence of a small amount of Ti^{4+}. The low-lying empty Ti (3d) bands increase the O–O anti-bonding band, thus promoting the evolution of oxygen. Therefore, the mitigation of voltage decay can be realized by doping larger-size elements or using a larger electro-active cation than Ru, which has been applied in DRXs.[127] In addition, the uniform distribution of $Li@Mn_6$ superstructure units within layered Li-rich oxides significantly inhibits the irreversible migration of transition metals and oxygen activation, resulting in stable voltage.[128,129] Moreover, O2-type Li-rich oxides are recognized for their ability to mitigate the irreversible migration of transition metals and reduce voltage fading.[130,131] Introducing transition metals, such as Al, into the Li layer to create a capped-honeycomb structure, can suppress the migration of transition metals and oxygen release, thereby significantly minimizing the voltage decay.[58]

According to *in situ* XAS experiments, the issue of voltage fading for $Li_{1.2}Ni_{0.15}Co_{0.1}Mn_{0.55}O_2$ was found to be the undesirable reduction of Mn and Co due to the release of oxygen.[132] As shown in Fig. 5a, during the electrochemical cycles, electrons are mainly captured and lost from the same e_g orbital when Ni^{2+}/Ni^{3+} and Ni^{3+}/Ni^{4+} redox reactions occur. However, the redox processes involving Mn and Co encompass both e_g and t_{2g} orbitals, which exhibit a substantial energy level disparity compared to reactions occurring within a single orbital. Consequently, the $Mn^{2+}/Mn^{3+}/Mn^{4+}$ and $Co^{2+}/Co^{3+}/Co^{4+}$ redox couples contribute to a reduction in the overall voltage. This phenomenon can be attributed to the significant energetic differences between the participating orbitals in the electron transfer processes. In addition, in the reductive coupling mechanism, the charge of oxygen first transfers to transition metals during the oxygen redox process. Different transition metal ions in the layered materials affect the charge transfer kinetics, for example, in comparison with $Ni^{3+/4+}$, Co^{4+} can promote faster charge transfer, thereby increasing the release of oxygen and exacerbating the voltage decay.[89,133] In addition, insufficient Li would prevent the diffusion of Li^+, and excessive Li would induce the reduction of the Mn valence in O2-type Li-rich oxides, resulting in a severe Jahn–Teller effect and accelerated voltage decay.[134]

Regarding high-voltage DRXs, they not only face the problem of voltage attenuation, but also have inferior capacity retention compared to layered Li-rich oxides. Both challenges originate from the same reason discussed above. In addition, the voltage fading is also related to the reduction of Mn^{4+} to Mn^{2+} ions.[125] The reported result shows that as the voltage window is broadened, the content of Mn^{2+} ions increases; meanwhile, the capacity fading and voltage decay become more serious. Therefore, selecting an appropriate voltage window is particularly critical for mitigating the voltage and capacity degradation in Li-rich oxides containing manganese.

According to numerous studies, there is a direct relationship between the voltage attenuation and release of oxygen, whether in LM-LRO or DRXs. Thus, voltage decay inhibition can be realized by applying strategies that suppress oxygen release. To achieve this target, Li *et al.* coated Na_2SiO_3 on the surface of $Li_{1.2}Ni_{0.2}Mn_{0.6}O_2$.[135] The elements in the coating layer can diffuse into the sub-surface of the bulk phase during the sintering process to exert a doping effect. Specifically, the larger-size Na doped into the Li layer has a pinning effect, which enhances the diffusion of Li^+ ions and improves the rate capacity, while stabilizing the crystal structure.[135 137] In addition, the doping of Si into the transition metal layer results in the formation of stronger Si–O bonds, which stabilize the O network. As a result, the release of oxygen is reduced and the migration of Mn is mitigated. Other coating materials, such as Li^+ ion conductors,[138 142] oxides,[143 149] and fluorides,[150 152] have also been applied, showing some benefits. The various coating materials and their effects on electrochemical performance are summarized in Table S1 (ESI†), highlighting of the thickness of the coating layer.[153] Based on these results, it is believed that materials with high Li^+ conductivity and good compatibility with the crystal of the bulk material are excellent candidates for cathode coating. A thin coating layer of less than 10 nm is preferred, and the migration of the elements from the coating material into the bulk is expected. These criteria can be satisfied by high-voltage LCO and Ni-rich oxides.

In addition, Zr, Si, Mg, Fe, Ti, Al, *etc.* element doping can also mitigate voltage fading.[154 159] For example, the incorporation of dopants can effectively control the structural characteristics of Li-rich oxide materials, including the distribution of Li and Ni atoms, M–O coordination environment, layer stability, and Li^+ ion mobility. Specifically, Mg substitution for Ni decreases the Li/Ni disorder, enabling sustainable anionic redox processes, enhancing the Li^+ diffusion pathways, and maintaining interfacial structural integrity, ultimately minimizing both voltage fading and hysteresis.[159] Besides, the design of gradient Li-rich oxides has been proven to be effective in mitigating oxygen release and the reduction of metal oxidation

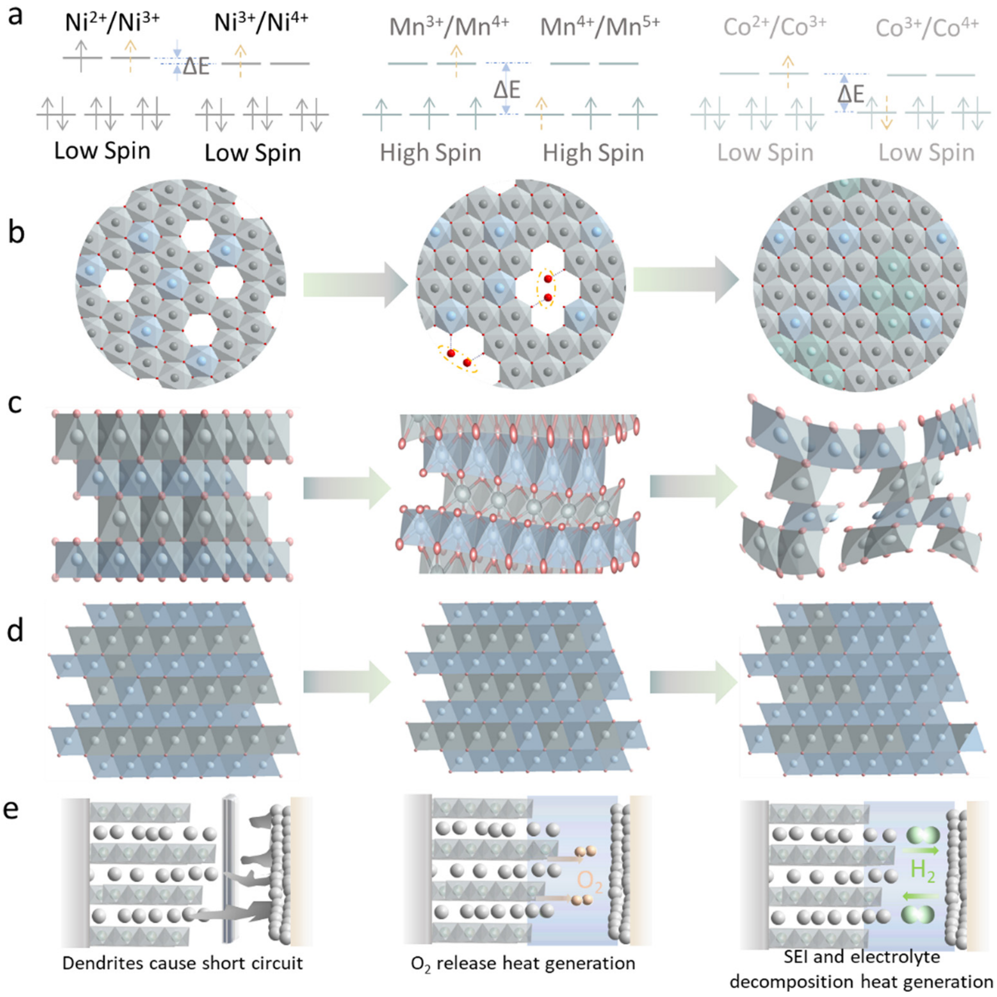

Fig. 5 Challenges associated in high voltage cathodes: (a) schematic of the energy level changes involved in the electron transfer of different redox couples of Ni, Mn and Co. (b) Vacancy clustering within the transition metal layer during the first-cycle charging plateau at approximately 4.5 V for Li-rich oxides. This cluster induces the creation of O_2 molecules and leads to rearrangement of the structure during discharge to the lowest voltage. The grey and light blue represent transition metals and the green and red dots represent Li and O, respectively. (c) Bending and fracture of the crystal structure of high-voltage LCO cathode material at different charging voltages. Light blue, green, red and yellow dots represent Co, Li, O and O vacancy, respectively. (d) Structure evolution of Ni-rich with Li/Ni mixing from layered to spinel to rock salt structure. Light blue, grey and red dots represent Ni, Li and O, respectively. (e) Schematic of three typical causes of thermal runaway. Silver dots represent Li.

states, as well as maintaining the crystal structure.[160,161] Zhu *et al.* synthesized a gradient Li-rich oxide with Li-poor surface and Li-rich core *via* a molten salt method.[162] In this unique structure, the oxygen framework is shared by the bulk and surface region without grain and phase boundaries, which shows a stable charge/discharge voltage plateau and enhanced oxygen redox activities.

As mentioned above, the migration and trapping of transition metals in the tetrahedra of Li layers result in voltage fading. This issue can be inhibited by mitigating the migration of transition metals or improving their reversible migration. Furthermore, research on DRX oxides with varying Mn/Fe/V transition metal arrangements has revealed that the Mn^{4+}–O bond, exhibiting lower covalency, effectively suppresses the charge transfer associated with oxidized oxygen in the Nb^{5+}/Ti^{4+} system. This inhibition prevents oxygen loss and helps maintain the stability of the crystal structure.[163] Additionally, the intricate metal arrangement in high-entropy oxides introduces a high-entropy effect, which effectively addresses many challenges associated with Li-rich oxides.[164 166] The incorporation of multiple elements in layered Li-rich oxides enhances the local structural diversity and the distortion energy of Mn^{4+}, resulting in improved local structural adaptability and greater structural stability. Therefore, the activation of low-potential redox couples and phase transitions are significantly restrained, and then the cycling stability is significantly enhanced.[167] Recently, Eum *et al.* reported that transition metals could reversibly migrate in O2-type Li-rich oxides,[130] thus suppressing the voltage decay phenomenon. Specifically, the migration of transition metals to adjacent LiO_6 octahedra through the intermediate tetrahedral sites is difficult due to the large electrostatic repulsion of face-shared cations, and therefore the cations can return to the transition metal layer through a streamlined path during discharging. In contrast, the edge-shared cations (O3-type) can migrate and be trapped into the octahedral sites in Li layers easily because of their poor electrostatic repulsion. Regulation of the Li^+ ion content also affects the reactivity of the oxygen anionic redox chemistry in O2-type Li-rich oxides, while excess oxygen redox can lead to mechanochemical failure due to asymmetric lattice breathing. An optimized Li content can significantly address the voltage decay in O2-type Li-rich oxides.[131] In addition to surface coating,[168] doping,[169] gradient and structure design strategies,[162] vacancy design,[170] grain size and morphology modifications (single crystal),[11] *etc.*, have been employed to suppress voltage attenuation. Here, we highlight the advantages of small-size single crystals compared to traditional polycrystalline oxides. Firstly, single crystals eliminate the presence of grain boundaries in polycrystalline materials, enhancing their mechanical strength and lowering the energy barrier for Li^+-ion diffusion across these boundaries. This mitigates the formation of structural microcracks during lattice contraction and expansion, and thus can reduce the exposure of fresh crystal surfaces and limit reactions with the electrolyte. Secondly, single crystals help suppress the irreversible release of oxygen. *In situ* DEMS results show that the oxygen release platform for single-crystal Li-rich oxide occurs at 4.98 V compared to 4.75 V for traditional polycrystalline Li-rich oxides. Additionally, single-crystal oxides inhibit the formation of superoxo species and reduce lattice stress within the structure, thereby stabilizing the crystal framework.[54,171 173] Lastly, the modification of electrolyte is also believed to be effective in reducing voltage decay. A recent study indicated that eliminating the polar ethylene carbonate from the electrolyte substantially reduces irreversible oxygen loss at the cathode-electrolyte interface. This alteration favors the *in situ* transformation from a layered to spinel phase, preventing the formation of the common rock-salt phase. The resulting spinel-stabilized surface improves the charge transfer kinetics *via* three-dimensional ion pathways, preserving the reversible redox activities of Ni, Mn, and O, thereby mitigating voltage decay.[57]

4.1.2. Voltage hysteresis. Both high-voltage layered Li-rich oxides and DRXs suffer from serious voltage hysteresis. However, their underlying mechanisms are studied from different perspectives. Firstly, the voltage hysteresis of layered Li-rich oxides is attributed to the formation of O_2 molecules being trapped in the crystal structure. Specifically, in the fully charged state, Li^+ ions are extracted from the transition metal layer, leaving Li vacancies, and the transition metals migrate in-plane to fill these vacancies, creating transition metal vacancies at their original positions. As the transition metal vacancies accumulate, O_2 molecules are formed between adjacent O–O atoms. Then, in the subsequent discharge process, Li^+ ions return to the vacancies previously occupied by transition metals (Fig. 5b), resulting in voltage hysteresis.[11]

Regarding high-voltage DRXs, Tarascon *et al.* proposed that the voltage hysteresis in $Li_{1.17}Ti_{0.33}Fe_{0.5}O_2$ (taken as a research model) is caused by the charge transfer from the O 2p nonbonding states to Fe 3d states with sluggish structural distortion,[25] which is different from the previously proposed formation/decomposition mechanism of O–O dimers,[174] or the mechanisms of redox inversion and sluggish structural rearrangement.[175,176] In this work, it was demonstrated that a large kinetic barrier has to be overcome to rearrange the oxygen network for charge transfer. During the oxygen redox process, electrons are not directly extracted from the O 2p non-bonding states, but through the non-equilibrium Fe^{4+}/O^{2-} intermediate state. Then, this non-equilibrium state continues until the electrons transfer from the O 2p to Fe 3d states and the system returns to the equilibrium $Fe^{3+}/O^{(2-n)-}$ ground state (Fig. 6a and b). This failure analysis may be extended to other transition metal-based DRXs, but this still needs to be verified.

In addition to the two above-mentioned main problems, Li-rich cathode materials face the problem of overall structure failure, leading to reduced electrochemical performance, which is also a problem faced by high-voltage LCO and Ni-rich cathode materials. This problem is mainly caused by the rupture of grains caused by the oxygen dimerization and transition metal migration. Recently, Kang *et al.* demonstrated through theoretical analysis and experimental observation that the rotational stacking faults (RSF) in the crystal structure are key contributors to grain cracking and electrochemical mechanical failure.[177] Fig. 6c shows a structural comparison between a material without RSF, one with a 120° RSF, and one with a 240° RSF. The structure without RSF exhibits minimal change after delithiation. In contrast, the structures with RSF show transition metal layer sliding after delithiation, shortening the bond length between the oxidized oxygens. Additionally, the calculated structure reveals that the oxygen dimerization reduces the migration energy barrier for transition metals and promotes their migration. Further, *ab initio* molecular dynamics (AIMD) simulations indicate that transition metal migration near RSFs promotes the formation of oxygen molecules. As this process progresses, intragranular cracks form near the RSF, as shown in Fig. 6d. This simulation result was corroborated by scanning transmission electron microscopy and collective geometric phase analysis (Fig. 6e).

Based on the above-mentioned analysis, the mitigation of voltage hysteresis can be achieved by increasing the covalency of M–O or tailoring the local changes (superstructure) in the crystal structure or utilizing a new electrolyte.[178 180] For example, the less electronegative S or Se has been doped into the lattice oxygen site.[82,168,181] The resulting structures have been monitored as ribbon and mesh superstructures and O2-type structure.[58,182 187] Among them, the ribbon and mesh superstructures help maintain the orderly arrangement of transition metals and enhance the vacancy formation energy. This stabilization suppresses the migration of transition metals and the formation of vacancy clusters, while facilitating the redox activity of oxygen anions, ultimately minimizing the voltage hysteresis.[11] Meanwhile, the O2-type Li-rich structure enables reversible transition metal migration, further contributing to the reduction in voltage hysteresis.[130] Ionic liquid-based electrolytes avoid the degradation of Li-rich oxides by preventing the leaching of transition metals, which also work for Ni-rich cathodes.[179,180] By substituting a portion of the carbonate solvent in the conventional electrolyte with fluoro-ether, a robust passivation layer

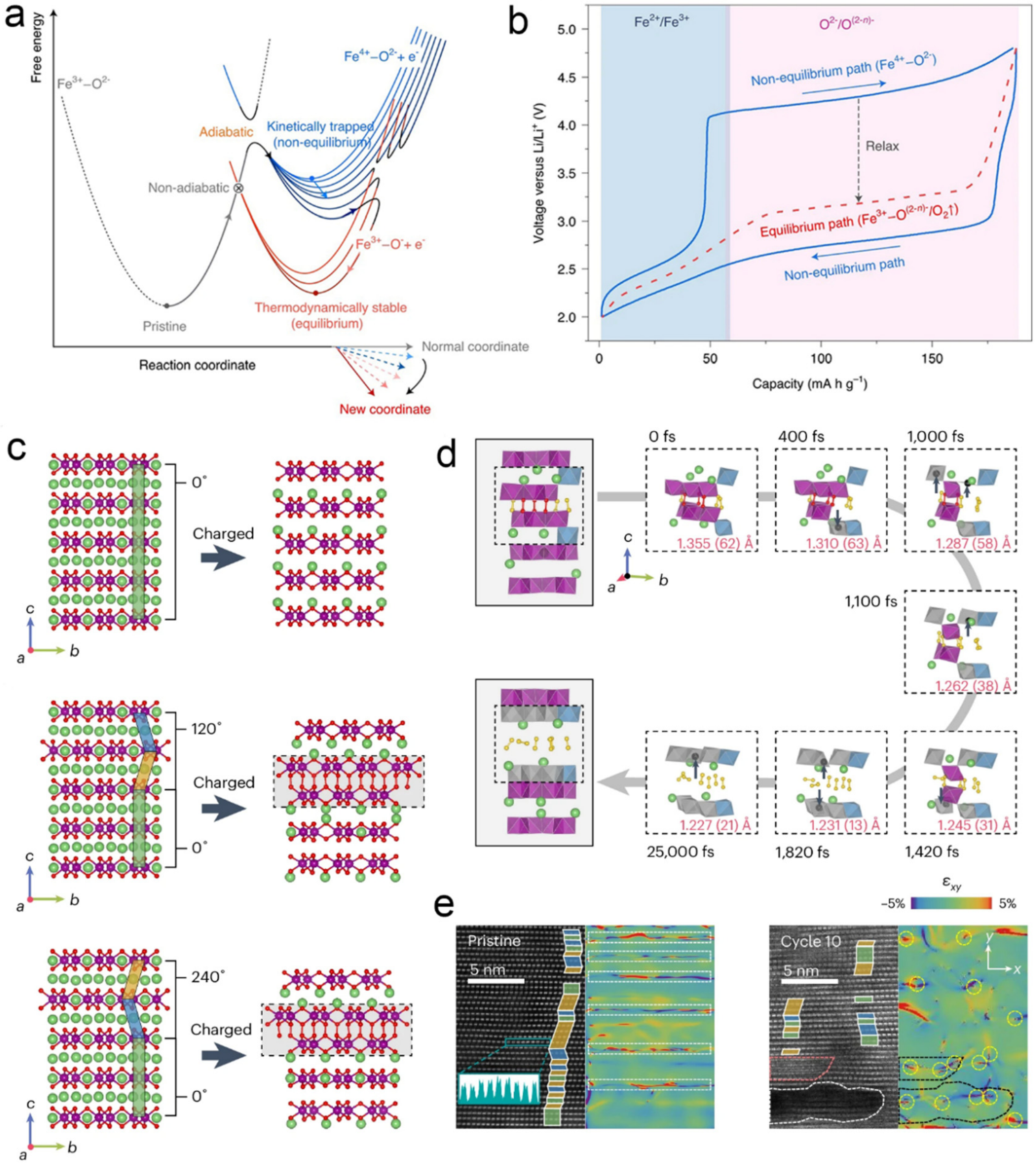

Fig. 6 Voltage hysteresis and electrochemomechanical failure analysis: (a) schematic of the electron transfer pathway during the oxygen redox process. (b) Schematic of voltage hysteresis in DRX. Reproduced with permission.[25] Copyright 2021, Springer Nature. (c) Schematic of rotational stacking fault structure. (d) AIMD simulation of intragranular crack formation near the rotational stacking faults. (e) Scanning transmission electron microscopy and geometric phase analysis of O2-type LM-LRO. Reproduced with permission.[177] Copyright 2024, Springer Nature.

rich in LiF and polymer is formed. This is due to the decomposition of fluoro-ether triggered by nucleophilic attack from oxygen-containing species, which helps maintain the stability of the bulk structure. Additionally, the fluoro-ether serves as "sutures", reinforcing the integrity and stability of both the interfacial and bulk structures. This significantly reduces the severe polarization and improves the cycling capacity.[188] Incorporating vinyltrimethylsilane as a new electrolyte additive substantially enhances the interfacial stability of Li-rich cathodes. Its addition also leads to a marked reduction in voltage hysteresis compared to the Li-rich cathode cycled in additive-free electrolytes.[189] All solutions are aimed to increase the d–p hybridization or favor anionic redox processes, while inhibiting the migration of transition metals to form vacancy clusters.

4.2. Challenges and strategies for high-voltage LCO materials

Despite its widespread use in consumer portable electronics due to its high theoretical energy density, LCO faces several challenges at high operating voltages, where one of the most significant is capacity fading. During cycling, LCO undergoes various phase transitions, especially at high voltages. The irreversible transition from hexagonal to monoclinic phase is the primary cause of structural degradation and loss of active material. Dahn *et al.* proved that LCO undergoes a large crystal structure change when charged to 4.5 V with the *c* axis expanding by 2.6% due to the increased repulsion between oxygen and oxygen, and then it contracts during discharge.[190] This repeated expansion and contraction of the crystal structure during electrochemical cycling induces structural degradation. Consequently, Co may migrate and dissolve in the electrolyte, diminishing the quantity of active material and potentially forming a resistive layer on the electrode and/or plating on the negative electrode, and the vacancy cluster left by its migration will induce oxygen dimer and oxygen release, thereby compromising the battery performance.[191,192] Moreover, this structural deterioration and ionic dissolution can be further attributed to the curvature of cobalt oxide layers in the near-surface region at high voltage.[193] Specifically, during the charging process of LCO, the continuous removal of Li^+ leads to the progressive deterioration of the curvature of the cobalt oxide layer. This escalating curvature introduces high structural stress within the material and promotes oxygen loss. Consequently, the aggravated layer curvature and oxygen deficiency result in further layer breakage, structure collapse, and crystal fragmentation, as illustrated in Fig. 5c. These detrimental effects are particularly severe in the near-surface region of LCO, where the structural changes are more pronounced due to the direct exposure to the electrolyte and the higher lithium extraction rates.

An additional structural concern is the phenomenon of lattice oxygen loss at high voltages, where the cationic redox is Co^{3+}/Co^{4+}. Co^{3+} is relatively stable within the lattice, but Co^{4+} is more reactive and prone to reduction, increasing the specific energy of LCO, but facilitating the loss of lattice oxygen. The latter phenomenon is a critical mechanism for LCO failure, given that it weakens the structural framework of LCO and promotes the formation of cobalt oxide by-products and other decomposition phases that are electrochemically inactive. The loss of oxygen is particularly concerning because it can lead to a positive feedback loop, where upon the release of oxygen, the remaining structure becomes more disordered, further accelerating the degradation process. Furthermore, it is also a major contributor to thermal instability, which is a significant safety concern in high-voltage LIBs.

To address the significant challenges posed by these failure mechanisms, researchers have implemented a range of strategies to mitigate the degradation of LCO at high voltages. A widely adopted method involves the application of surface coatings and the incorporation of dopants into LCO. These coatings, which can be composed of materials such as LiF,[104] lithium zirconate (Li_2ZrO_3),[141] and other metal oxides and elements,[194,195] act as a protective barrier separating LCO from the electrolyte. An $AlPO_4$-5 zeolite layer was coated onto LCO, and this coating layer could mitigate the phase transition by suppressing oxygen release and achieving fast Li^+ diffusion.[196] The protective interphase minimized the direct contact between the electrolyte and the reactive cathode surface, effectively limiting surface degradation and Co dissolution. The recent results on coating-modified high-voltage LCO are summarized in Table S2 (ESI†). The criteria for selecting coating materials are the same as that discussed above for Li-rich oxides. Alternatively, dopants, such as Mg, can contribute to stabilizing the cathode structure by preventing phase transitions under high voltage conditions.[195] The introduction of La and Ca in LCO achieves both surface coating and subsurface gradient doping, which can jointly create an oxygen ion reservoir on its surface, effectively suppressing oxygen release and enhancing the stability of the crystal structure.[197] The high-entropy strategy has also be applied in high-voltage LCO to overcome the corresponding challenges. La–Al–Mg–Y high-entropy doping can improve the stability of LCO and suppress phase transitions at high voltage operation.[198] Co-doping LCO with Mg, Al, and Eu generates a near-surface high-entropy oxide layer, which significantly mitigates oxygen release and structural degradation.[199] Aiming to address different issues, various candidates have been proposed as dopants for LCO. Among them, W, Zr, and Nb have been widely investigated. W can be doped into either the Co or Li sites depending on the synthesis method. When doped into the Li sites, it acts as a pillar, enhancing the Li^+ ion diffusion.[200,201] The W doping can also reduce the surface energy of LCO, leading to a decrease in the particle size of LCO and improvement in the rate performance.[202] Zr doping can increase the electron density at the Fermi level, thereby slowing down the charge transfer from O to Co and suppressing the formation of Co^{2+} and O_2.[203] Additionally, Zr doping enhances the crystal structural stability, promotes Li^+ diffusion, and suppresses lattice oxygen oxidation.[204,205] Nb^{5+} doping enhances the stability of LCO, decreases the charge transfer resistance and promotes Li^+ ion diffusion.[206] It can also mitigate the release of oxygen and migration of Co due to the strong Nb–O bond energy, while inhibiting electrolyte decomposition and contributing to a stable cathode electrolyte interphase (CEI).[200,204] Furthermore, Nb doping can significantly improve the electronic conductivity due to the high overlapping of the Co 3d-O 2p orbitals at the valence band maximum induced by the strong Nb 4d-O 2p hybridization.[207] The comparative analysis of the above-mentioned element doping modifications is shown in Table S3 (ESI†). An additional approach includes the incorporation of electrolyte additives designed to enhance the stability of the CEI.[208] Additives such as fluoroethylene carbonate (FEC) have been shown to form a more stable and less resistive CEI layer, which can reduce the impedance growth and improve the long-term cycling stability of high-voltage LCO cells.[209] Lithium bis(oxalato)borate (LiBOB) and tris(trimethylsilyl)phosphite (TMSPi) are incorporated into the carbonate-based electrolyte, where they can decompose before the carbonate solvent, enhancing the electrolyte stability. The breakdown of TMSPi produces Li^+-conductive phosphorus-containing species and helps prevent the over-decomposition of LiBOB. The synergistic effect of the durable B-containing species and the Li^+-conductive phosphorus-containing species in the CEI contribute to the outstanding performance of the LCO cathode at a high operating voltage of 4.5 V.[210] These additives function by decomposing preferentially on the cathode surface, creating a protective layer that inhibits further electrolyte degradation and prevents Co dissolution. In addition, the regulation of band and magnetic structures can also improve the stability of LCO.[20,211] For example, the optimization of O → Co charge transfer can be achieved through precise regulation of Li/Co anti-site defects *via* the simultaneous incorporation of Mg^{2+} and $(PO_4)^{3-}$ ions. Meanwhile, properly regulated Li/Co anti-site defects enhance the redox activity of Co ions, while suppressing the irreversibility of the oxygen redox and the associated Co reduction.[211] Oxygen vacancies lead to the formation of an oxygen magnetic moment, and the combined effect of oxygen vacancies and V doping stabilizes the oxygen magnetic moment during charge/discharge cycles. This synergy reduces the oxidation state of oxygen and enhances the reversibility of oxygen redox reactions, effectively preventing irreversible oxygen release. Additionally, oxygen vacancies decrease the overlapping of the electron cloud and lower the O 2p band center, thereby reducing the oxygen redox activity.[20] Recent studies on single-crystal LCO have demonstrated that it can significantly reduce the release of oxygen and the generation of microcracks in the crystal structure.[212 214] The oxygen release is significantly reduced in gradient single-crystal LCO, as determined by DEMS.[213] In addition, various single crystal shapes can effectively inhibit the release of oxygen and suppress lattice strain, for example, spherical single crystal LCO can better suppress phase transformations than plate single crystal LCO, as confirmed by *in situ* XRD.[214,215]

The above discussion is a comprehensive overview of the main challenges faced by LCO and the corresponding strategies to address them. Regarding how to reversibly utilize the redox of oxygen anions in LCO, we believe that the following aspects can provide inspiration. Initially, a thorough surface-to-bulk depth-delithiation method that incorporates trace amounts of Mg–Nb–Al co-doping at lithium sites, in combination with interfacial hierarchical fluorination, can help reduce side reactions, limit Co migration, and improve the reversibility of anionic redox reactions.[216] The enhanced reversibility of oxygen redox processes and the reduced loss of lattice oxygen can be linked to the presence of Nb, given that this element can lessen the formation of electronic holes in oxygen by modifying the strength of the Co–O octahedral field. Next, a comprehensive approach involves Al–Mg–Zr co-doping in LCO, paired with regulation of the solvation structure. This method ensures that co-doping stabilizes the crystal structure and limits irreversible phase transitions as well as the loss of lattice oxygen. The solvation structure adjustments provided by zeolite films improve the oxidation resistance of the electrolyte and reduce side reactions at elevated voltages. Consequently, the stable crystal structure and minimized oxygen loss improve the reversibility of oxygen anionic redox processes.[67] Lastly, substituting oxygen with selenium, a less electronegative and anti-aging element, can help prevent oxygen loss and increase the reversibility of oxygen redox reactions. The introduction of Se can elevate the energy levels of the non-bonding orbitals in the ligand, bringing them closer to the transition metal d bands. This facilitates the transfer of charges from oxidized oxygen, reducing it to O_2, which enhances the reversibility of oxygen redox chemistry.[217]

In conclusion, although LCO remains a critical material for LIBs, its performance at high voltages is limited by a series of complex and interrelated failure mechanisms, including structural degradation due to phase transitions and oxygen loss, surface degradation from electrolyte oxidation and Co dissolution. Addressing these challenges requires a multifaceted approach, including the use of protective coatings and doping, electrolyte additives, and controlled synthesis of the material structures. A synergistic combination of these approaches will likely be the most effective in harnessing the benefits of reversible oxygen anionic redox chemistry within LCO. By understanding and mitigating these failure mechanisms, it is possible to extend the life of high-voltage LCO batteries and enhance their safety and performance in demanding applications.

4.3. Challenges and strategies for high-voltage Ni-rich materials

Although high-voltage Ni-rich cathode materials are being gradually promoted in electric vehicles, these materials face significant challenges related to their long-term stability and safety, which are caused by intricate reasons, involving surface degradation, irreversible structural changes, oxygen evolution, cation mixing, *etc.* Among them, surface degradation stands out as a particularly significant factor.[218] At elevated voltages, Ni-rich cathodes become increasingly susceptible to parasitic interactions with the electrolyte. The high Ni content contained inside exacerbates the reactions, leading to the formation of a surficial layer composed of not only favorable products such as lithium carbonate (Li_2CO_3) and lithium fluoride (LiF), but also various organic by-products, which are not ideal components for CEI. Therefore, the CEI on Ni-rich cathodes is generally prone to instability, exhibiting continuous growth throughout the cycling process. This progressive CEI formation contributes to increased cell impedance and diminished ionic conductivity, both of which negatively impact the battery performance. Additionally, the formation of a CEI depletes the active Li^+ ions, reducing the amount of Li^+ ions available for electrochemical reactions, which ultimately leads to capacity fading over time.

The structural change in Ni-rich cathode materials at high voltage also generates cell degradation. During delithiation, Ni ions, which are present in large quantities, can migrate from their original octahedral sites to tetrahedral sites within the crystal lattice. This ion migration phenomenon frequently induces irreversible structural transformations, most notably the conversion of the layered architecture to spinel or rock-salt configurations (Fig. 5d).[219] These phase transitions are particularly deleterious given that they typically result in the deterioration of crystallographic coherence, subsequently leading to the nucleation and propagation of microcracks within the cathode particles. The formation of these microcracks not only exposes the pristine surfaces to the electrolyte, thereby exacerbating undesirable side reactions, but also compromises the mechanical integrity of the cathode particles. Over time, this can lead to pulverization of the particles, further accelerating the capacity loss and impedance growth in the cells. Furthermore, the transformation of the layered structure into a rock-salt structure, which lacks electrochemical activity, significantly limits the quantity of active material available for electrochemical reactions, thereby decreasing the overall capacity of the battery. Another critical issue with high-voltage Ni-rich cathodes, similar to Li-rich cathodes and high-voltage LCO, is their thermal instability, which is closely linked to the release of oxygen from the lattice during extensive delithiation.[220] Oxygen release is primarily driven by the high oxidation state of Ni ions (Ni^{4+}), which destabilizes the oxygen sublattice. The liberated oxygen can react with the electrolyte, resulting in the release of heat, which elevates the cell temperature, and thus further triggers a self-sustaining thermal runaway process, posing serious safety risks.[221] The loss of lattice oxygen also leads to a reduction in the M–O bond strength, further destabilizing the structure and promoting phase transitions, *e.g.*, from layered to spinel or rock-salt phases, as discussed earlier. This thermal instability is a significant challenge for the safe operation of high-voltage Ni-rich, LCO and Li-rich cathodes.

Cation mixing, where Ni^{2+} ions migrate into the Li layers of the crystal structure, is another critical degradation mechanism in Ni-rich cathodes. This phenomenon is particularly pronounced during high-voltage cycling. Cation mixing reduces the availability of Li sites in the crystal structure, impeding Li^+ ion diffusion during cycling, which not only decreases the rate capability but also contributes to capacity fading of the cathode material.[222] Moreover, cation mixing can lead to the formation of a disordered structure, which further compromises the electrochemical performance of the cathode material. The presence of Ni^{2+} in the Li layers also creates local stress within the crystal structure, which can further exacerbate the structural degradation and lead to the formation of defects and microcracks.

To address the challenges in high-voltage Ni-rich cathodes, various strategies have been proposed, and some of them have been practically achieved. Similar to the other two high-voltage materials, surface coatings and bulk doping are also adopted to prepare Ni-rich cathode materials. Materials such as metal oxides and Li^+ ion conductors (*e.g.*, solid-state electrolytes) are often used as coating materials,[66,218,223 225] which serve as a physical barrier between the cathode particle and the electrolyte, and therefore can effectively suppress side reactions and minimize the formation of resistive surface layers. Surface coatings are also helpful to improve the thermal stability of the cathode, reducing the likelihood of oxygen evolution and thermal runaway.[221,224] The studies on various coating materials and their corresponding thicknesses are summarized in Table S4.[226 229] According to these studies, we can derive selection criteria similar to that for high-voltage Li-rich and LCO coatings, namely, Li^+ conducting properties, compatibility with the Ni-rich oxide crystal structure, a controlled thickness of no more than 10 nm, and ideally the coating element should be partially incorporated into the coated materials. Doping can stabilize the crystal structure and reduce the extent of cation mixing and cracks.[230 233] Recently, the innovative high-entropy strategy has been employed to stabilize Ni-rich materials through entropy stabilization, while incorporating coating and doping techniques. For instance, introducing Zr and Al into Ni-rich single-crystal $LiNi_{0.92}Co_{0.05}Mn_{0.03}O_2$ or Ce/Gd into single-crystal $LiNi_{0.83}Co_{0.07}Mn_{0.10}O_2$ enables surface modification with high entropy, effectively mitigating lattice oxygen loss and preventing unfavorable transition metal migration and structural degradation.[234,235] It has been noted that the efficacy of coatings depends on their uniformity, thickness, and adhesion to the cathode surface. Alternatively, the impact of doping is influenced by both the concentration and spatial distribution of dopants within the cathode materials. In addition, doping with high-valent cations, such as W^{6+}, induces the formation of a superstructure in Ni-rich oxides (*e.g.* $Li_{1.06}Ni_{0.90}W_{0.04}O_2$).[236] This structural modification facilitates the reversible migration of transition metals and enhances the reversible redox activity of oxygen anions. A protective CEI can also be generated by incorporating specific additives into the electrolyte.[208,237,238] For instance, the inclusion of ethyl 2-butene phosphite (EBP) in a standard carbonate electrolyte has been shown to facilitate the formation of a robust CEI on Ni-rich cathodes. This occurs prior to electrolyte breakdown, which helps maintain the cathode structural integrity and contributes to high capacity retention, even when operating at a high cut-off voltage of 4.6 V.[239] An alternative strategy, grain boundary engineering has been proposed to mitigate microcrack formation and improve the mechanical stability of Ni-rich cathodes.[240] Techniques such as solid-state sintering and the utilization of sintering aids can enhance the cohesion of grain boundaries within cathode particles, thereby diminishing the risk of particle pulverization and improving the overall durability of the material.[241,242] By strategically modifying the grain boundaries, the accumulation of microcracks and defects can be reduced, which frequently initiates structural degradation and capacity fading.[243] Additionally, advancements in grain boundary engineering can boost the ionic conductivity of cathode materials, enhancing both the rate capability and overall performance of batteries.[242,244] The single crystal structure eliminates the unstable grain boundaries in polycrystals, and thus problems such as microcracks and oxygen release caused by grain boundaries can be significantly limited.[7,245] Ma *et al.* demonstrated through SEM analysis that single-crystalline Ni-rich cathode materials remained free of visible cracks even after 300 cycles, whereas the polycrystalline materials developed significant microcracks along the grain boundaries.[246] The effects of single-crystal and polycrystalline Ni-rich cathode materials on gas release were quantitatively analyzed using *in situ* DEMS. The analysis revealed that single-crystal oxides demonstrated greater stability, producing less gas than polycrystalline materials even at higher voltages. This finding highlights the superior structural stability of single-crystal materials.[247] In addition, considering that the highly oxidized Ni^{4+} can strongly reduce the surface stability of Ni-rich cathode particles at high voltage, the synthesis of gradient particles, *i.e.*, with a lower Ni content on the surface and higher Ni content in the bulk, is another strategy that has been explored to improve their performance.[248] By reducing the surface Ni content, side reactions between the electrode and electrolyte can be minimized, thereby mitigating the growth of resistive surface layers. Concurrently, the high Ni content in the bulk ensures a high capacity and energy density. This approach has shown promise in improving the cycle life and thermal stability of high-voltage Ni-rich cathodes, and further research is ongoing to optimize the composition gradients for different applications.

To suppress the release of oxygen at high voltage and better utilize the reversible oxygen redox, doping is emphasized as a simple and effective strategy. For example, Al doping mitigates irreversible oxygen release, while promoting lattice oxygen redox chemistry. This modulation of oxygen redox activity significantly enhances the reversibility of the structural phase transition in Ni-rich cathodes.[110] In addition, to enhance the reversibility of the oxygen redox, it is necessary to maintain the lattice oxygen, *i.e.*, suppress oxygen evolution. Therefore, strategies such as surface coating and gradient particle design can significantly reduce the release of oxygen, and especially inhibit the loss of lattice oxygen at the surface, thereby enhancing the oxygen redox reversibility.[111]

In summary, high-voltage Ni-rich cathodes offer significant potential for high-energy-density applications, but their widespread adoption is hindered by various failure mechanisms, including surface degradation, structural changes, oxygen evolution and cation mixing. Thus, to address these challenges, several strategies, such as surface coating, doping, electrolyte additive, grain boundary engineering, and gradient compositions, have been proposed and are being actively researched. Continued research and development in this area are essential for unlocking the full potential of Ni-rich cathodes and advancing the next generation of LIBs.

4.4. Oxygen release cross-reaction with the anode

For the release of oxygen, McCloskey *et al.*, through ^{18}O isotope labelling and quantitative DEMS analysis, concluded that oxygen release primarily stems from anion redox reactions and phase transitions in the cathode material at voltages exceeding 4.55 V.[249] They found that Li_2CO_3 on the surface of the cathode does not directly emit oxygen, but instead generates reactive oxygen species, which interact with the electrolyte to form a solid electrolyte interphase (SEI) and cause electrolyte degradation.[250] Importantly, the release of oxygen can have several detrimental effects on the anode from chemical, electrochemical, and mechanical aspects, leading to performance degradation, safety concerns, and reduced battery life. Firstly, one of the primary chemical effects of oxygen release is the potential oxidation of the anode material. In commercialized LIBs and next-generation lithium–metal batteries (LMBs), graphite and lithium metal are and will be employed as the anode material, respectively, both of which are highly reactive with oxygen. The relevant reactions lead to the formation of insulating oxide layers on the anode surface. For instance, on lithium metal anodes, oxygen can react with the electrolyte to form a passivation layer, leading to increased interfacial resistance, and thus hindering the electrochemical performance of the anode.[251] Moreover, these reactions can also lead to the consumption of active lithium, reducing the overall capacity of the battery over time. In the case of graphite anodes, their interaction with oxygen can lead to the formation of various carbon–oxygen compounds, further increasing the resistance and leading to capacity fading.[252,253] Secondly, the release of oxygen can influence the stability of the SEI on the anode, which is crucial for the stable operation of conventional LIBs as well as LMBs. The presence of reactive oxygen species can lead to the oxidation of the SEI components, destabilizing the layer and leading to its continuous reformation.[254] This process depletes both the electrolyte and active lithium, leading to capacity loss and elevated impedance.

In addition, the released oxygen can instigate side reactions between the electrolyte and anode, particularly in the presence of liquid electrolytes. These side reactions can generate gaseous by-products such as carbon dioxide (CO_2) and volatile organic compounds, leading to the swelling of the battery and potential safety hazards such as venting and thermal runaway.[255–257] Regarding the release of CO_2, through isotope labelling with ^{18}O, Bruce *et al.* investigated oxygen evolution in Li-rich layered materials using *in situ* DEMS. Their analysis revealed that the oxygen extracted from the crystal lattice underwent reactions with the electrolyte, resulting in the formation of $C^{16/18}O_2$.[83,258] In addition, the decomposition of residual lithium carbonate on the positive electrode surface will also produce CO_2.[250,259] The electrochemical potential at the anode can be altered as a result of these reactions, which complicates the battery performance and may create problems such as lithium deposition and dendrite growth. Moreover, the release of oxygen and the ensuing chemical reactions can induce mechanical stress within the battery. The formation of oxide layers or gaseous by-products can cause volumetric expansion at the anode, leading to mechanical deformation. This stress is particularly concerning in LMBs, where the anode is susceptible to dendrite formation. It is reported that the generated mechanical stress exacerbates dendrite growth, increasing the risk of short circuits and failure.[260,261] Furthermore, the continuous formation and breakdown of the surface layers due to oxygen interactions can lead to particle cracking and electrode pulverization,[260] particularly in high-energy-density batteries where the electrodes undergo significant volume changes during cycling. These mechanical failures contribute to the overall degradation of the structural integrity and performance of the battery over time.

Given the significant impact of oxygen release on the anode and overall battery performance, several strategies have been developed to mitigate its effects. Firstly, given that oxygen release is generated from the cathode, modifying the cathode material to stabilize the oxygen lattice is necessary. This has been achieved by doping cathode materials with elements that strengthen the M–O bonds[262,263] and insertion of protective coatings on the cathode particles to prevent oxygen from escaping into the electrolyte.[63] Secondly, advancing electrolytes to reduce their reactivity with oxygen is another approach. In particular, solid-state electrolytes are advantageous due to their inherent non-flammability and diminished susceptibility to side reactions triggered by oxygen.[264,265] These electrolytes can also provide mechanical support to the electrode structure, mitigating the mechanical effects of oxygen release. In liquid electrolytes, additives can be introduced to stabilize the SEI layer and reduce its reactivity with oxygen, *e.g.*, fluorinated compounds.[179,180,266,267] Thirdly, it is imperative to shield the anode from degradation caused by oxygen exposure. This can be effectively accomplished by employing artificial SEI layers or protective coatings on the anode surface.[268 270] These barriers mitigate the direct contact between the anode and the released oxygen, thereby safeguarding the electrochemical properties of the anode and extending the overall battery lifespan.

In conclusion, the release of oxygen from anionic redox reactions has a profound impact on the anode in battery systems, influencing their chemical, electrochemical, and mechanical properties. The effects of oxygen release can lead to performance degradation, safety risks, and reduced battery life. However, although various strategies are being developed to mitigate these harmful effects, the management of oxygen release remains a critical challenge in the development of high-voltage Li-rich, LCO and Ni-rich cathodes. Thus, continued research and innovation are needed to fully address these challenges and enable the safe and efficient operation of future battery technologies.

4.5. Thermal runaway

Despite their various specific issues, the critical common challenge encountered with all high-voltage cathode materials is safety, where the thermal runaway is the main cause. The occurrence of thermal runaway is accompanied by a series of chain reactions, and the reactions among battery components happen sequentially. As shown in Fig. 5e, three aspects are considered to be reasons of thermal runaway. Firstly, lithium dendrites can puncture the separator and cause a short circuit of the battery, and then further thermal runway. Short circuit and spontaneous combustion may occur when batteries are damaged by external extrusion. Secondly, when overcharging, Li^+ ions are continuously extracted from the cathode materials, causing structural collapse and oxygen release, accompanied by a large amount of heat generation; therefore, the organic electrolyte will be ignited. Thirdly, the SEI film and electrolyte decompose at high voltage, generating a lot of heat and flammable gas. In general, a high cell voltage will introduce a high risk in thermal runaway. The heat release in LIBs is measured using two common methods, accelerated-rate calorimetry (ARC) and isothermal heat conduction calorimetry (IHC). ARC measures the rate of heat generation and provides kinetic parameters such as enthalpy and the triggering temperature of the heat release process. Meanwhile, IHC is utilized to assess the thermal stability of materials.[271] According to relevant research, three characteristic temperatures (T_1, T_2, and T_3) serve as key parameters for assessing the thermal runaway in batteries. T_1 marks the onset of thermal stability loss, where the heating rate surpasses 0.02 °C min^{-1}. T_2 indicates the triggering temperature of thermal instability, with the heating rate exceeding 1 °C min^{-1}. Finally, T_3 represents the peak temperature of thermal instability, at which the heating rate exceeds 60 °C min^{-1}.[272,273] For example, Ni-rich cathode materials such as $LiNi_{0.8}Co_{0.1}Mn_{0.1}O_2$ (NCM811) and $LiNi_{0.6}Co_{0.2}Mn_{0.2}O_2$ (NCM622) exhibit a similar T_1 temperature of ≈158 °C. However, the T_2 temperature of NCM622 is 185 °C, which is approximately 20 °C higher than that of NCM811. Both materials share a T_3 temperature of ≈290 °C. It should be noted that the decomposition temperature of the SEI is below 100 °C, and the separator begins to melt and shrink between 130 °C and 160 °C, which can lead to short circuits and thermal runaway.[272,274] Therefore, researchers have proposed a series of solutions to solve the thermal runaway problem, including tailoring electrolyte formulation, separator, current collector, electrode material and battery manage system. For example, regarding the electrolyte, flame retardants are introduced as electrolyte additives, or non-flammable electrolytes are used in high-voltage cells, such as organophosphate flame retardant,[275,276] phosphazene flame retardant[277] and room temperature ionic liquids,[278 280] and others.[281 283]

Numerous studies have been conducted to investigate how the modification of the battery components reduces thermal runaway,[271,284,285] but the research on the thermal safety of high-voltage cathode materials is limited.[286 288] Compared with traditional cathode materials such as $LiFePO_4$ and ternary oxides, the study of thermal runaway for high-voltage cathode materials is more important but challenging because they have highly reactive oxygen species, more active and high-valent metal ion dissolution and even crosstalk with other battery components. The release of oxygen from the lattice exacerbates this risk, given that it can react with the electrolyte to produce flammable gases or act as an oxidizer for any flammable compound. These gases can accumulate within the battery, leading to an increase in internal pressure, and eventually cell rupture. Based on a previous study, the thermal runaway is highly related to the type of cathode materials by accelerating the rate calorimetry, where that with a single crystal structure could enhance the thermal stability.[272] Moreover, Sun and colleagues proved that the reason for the poor thermal safety of the $LiNi_{0.8}Co_{0.1}Mn_{0.1}O_2$ cathode is due to the generation of a large amount of oxygen at the voltage of ≥4.7 V. They also pointed out that the single crystalline cathode could significantly mitigate oxygen release and improve the thermal safety.[289] Chen and colleagues claimed that the ultra-conformal coating layers on both secondary and primary particles of high-voltage oxide cathodes could obviously enhance their thermal stability and reduce the thermal runaway.[290] Overall, although there are many challenges to overcome, the thermal stability and safety of high-voltage cathode materials are unescapable targets to be achieved for the practical deployment of high-energy-density batteries.

5. Characterization of high-voltage cathode materials

Advanced, accurate and comprehensive *ex situ* or *in situ* characterization methods are vital for understanding the oxidation–reduction reaction, internal ion transportation, and structure transformations occurring in the cell during cycling. Complete and multi-scale analysis of the morphology, structure and composition of the electrode materials is helpful to explore

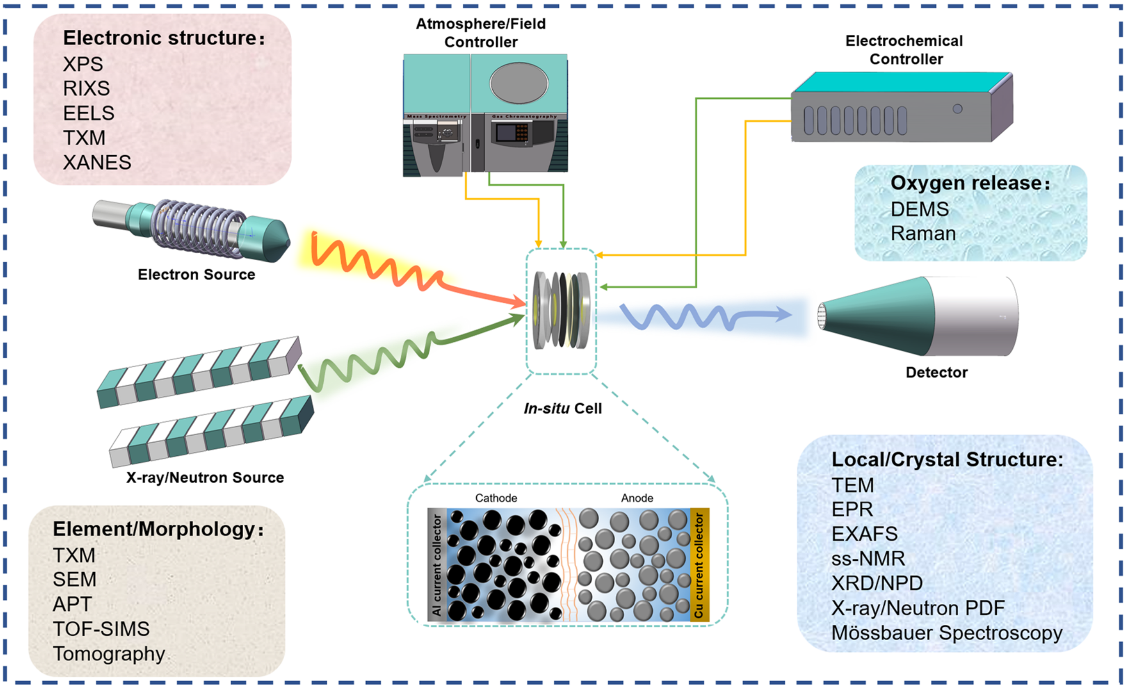

Fig. 7 Classification of characterization techniques based on different study purposes.

the electrochemical reaction details and provide new insights for material and cell design. Depending on the applied energy source (electron, X-ray, neutron, *etc.*), various destructive or nondestructive characterization techniques have been developed. In the following, we mainly introduce the fundamental and critical techniques used in research on high-voltage cathode materials according to their expertise, as shown in Fig. 7.

5.1. Crystal structure and atom arrangement

XRD is the most commonly used characterization method in determining the atomic and molecular structure of crystals in both powder and thin-film states. By measuring the angles and intensities of the diffracted X-ray beams from the lattice, the crystallographer can produce a 3D picture of the density of electrons within the crystal, where the crystallinity, purity, and their crystallographic disorder, as well as other structural information can be determined. For instance, Sun and colleagues demonstrated the change in lattice parameters and phase transition in an $Li_{1.23}Ni_{0.09}Co_{0.12}Mn_{0.56}O_2$ LM-LRO by *in situ* XRD.[291] Firstly, they proved the existence of β-MnO_2 at approximately 4.54 V in the initial charge process, followed by its transformation to layered $Li_{0.9}MnO_2$ during discharge. Different from XRD, neutron diffraction (ND) uses neutrons as the source, which interact with the nuclei, and thus presents a high penetration depth and sensitivity to light elements such as O and Li. Benefitting from its superior scattering abilities, ND is a powerful tool to conduct nondestructive *in situ* structural characterization of batteries during cycling under different environments, especially in identifying the atomic occupation, vacancies, lattice parameters, space symmetry and phase ratio.[292,293] By applying *in situ* ND on LM-LROs, it was revealed for the first time by Meng and colleagues that the lithium migration rates at different sites were highly dependent on the voltage regions.[294] Employing the maximum entropy method, Xiao *et al.* visualized that Li^+ ions migrated through the tetrahedral site hopping path at the beginning of charge, and then moved *via* the indirect zigzag hopping path in a ternary oxide material.[295]

Based on the XRD and ND techniques, the corresponding PDF method has been developed, which describes the distribution of distances between pairs of particles contained within a given volume combining information from both Bragg peaks and diffusion scattering. Therefore, it can not only give the local structure variation in different phases or nanoclusters, but also provide the short-range change from atom to atom. Zhao *et al.* directly showed the variation in the O–O distance caused by oxygen redox in the bulk structure of an $Li_{1.2}Ti_{0.35}$-$Ni_{0.35}Nb_{0.1}O_{1.8}F_{0.2}$ DRX during the charging/discharging process.[43] In addition, Hu *et al.* revealed that the O–O pair distance underwent a pronounced reduction through the lattice in a highly charged LCO.[16] In short, PDF is a powerful tool to investigate the short-range configuration in not-well defined phases, especially for the samples with light elements or trace doping.

Unlike X-rays and neutrons, when an accelerated and concentrated electron beam is transmitted onto an ultrathin specimen, electrons collide with the atoms in the sample and change the moving directions, resulting in solid angle scattering. In detail, the size of the scattering angle is related to the density and thickness of the specimen, and thus different light and dark images can be formed, which will be enlarged and focused on the imaging device. Based on this principle, TEM can provide the intuitive crystal structure in the local site, which is different from XRD and ND showing the macroscopic structure. In addition, the atomic arrangement can be visualized based on differences in atomic number.[296] For example, Yan *et al.* observed the spatial distribution and diffusion of oxygen vacancies in the bulk lattice of an $Li_{1.2}Ni_{0.2}Mn_{0.6}O_2$ LM-LRO through spherical aberration TEM and 3D reconstructed tomography,[297] which offer a precious opportunity for understanding the performance degradation mechanism of high-voltage materials. Combined with theoretical calculation, the results showed that both the decrease in the formation energy for oxygen vacancies and diffusion barrier energy of $O_2{}^{n-}$ species accelerated the formation of oxygen vacancies at the particle surface and diffusion toward the bulk lattice. Therefore, to improve the electrochemical performance of LM-LRO, modifying the cavity band of particle surfaces and doping heteroatoms to form stronger bonding are two effective strategies to inhibit the production of oxygen vacancies and block the migration of oxygen vacancies. Moreover, Freire *et al.* used high-resolution TEM (HRTEM) to evidence the formation of a well-crystallized DRX $Li_4Mn_2O_5$,[298] which was free from any defects and secondary phases. This material showed the highest discharge capacity among the known Li–Mn–O oxides at that time, opening a door for research on high-voltage cathode materials.

Although TEM can give important information, batteries need to be disassembled for their analysis, thereby destroying their real operating environment. Therefore, *in situ* TEM has been developed. *In situ* TEM refers to the process of observing and characterizing the microstructure evolution of samples directly at the atomic level in real-time under force, heat, electricity, magnetism and chemical reactions. Accordingly, researchers can obtain more data about the dynamic structural evolution details of materials during the charge/discharge process of batteries compared to the traditional *ex situ* microscopy. Wu and colleagues studied the evolution of crystal structures in Ni-rich cathode materials using *in situ* TEM.[299] They revealed the continuous lattice collapse during lithium and electron extraction. The collapsed and expanded regions corresponded to the H3 and H2 phases, respectively. According to this observation, the lattice collapse interface was ascribed to a dynamic H2–H3 phase transition process. In addition, Gong *et al.* demonstrated through *in situ* TEM that after high-voltage delithiation in a solid-state battery, the original single-crystalline LCO transformed into a nano polycrystalline structure with coherent twin and antiphase domain boundaries, unlike the multiple phase changes observed in liquid electrolyte battery cathodes.[300]

The change in the local coordinate environment for light elements such as Li can be tracked by solid-state nuclear magnetic resonance (ss-NMR) spectroscopy at the atomic level, which focuses on a target nucleus in solid materials, *e.g.*, powder, single crystal and amorphous samples. The migration of a single atom, differences in the local environment and structural evolution of metastable structures can be identified during electrochemical processes.[301,302] Zhou and colleagues conducted ^{7}Li ss-NMR to investigate the underlying relation between structural stability and reversibility of the oxygen redox in an O3-type $Li_{0.6}[Li_{0.2}Mn_{0.8}]O_2$ (Fig. 8a),[301] which showed that most Li ions were removed from the alkali metal layer during charging. This resulted in the formation of O–Li and O-vacancies in the remaining $Li_{0.2}Mn_{0.8}O_2$ structure, which was beneficial for the oxygen redox reactions according to DFT calculations. When the cell was discharged to 2.0 V, almost all the Li ions returned to their original positions, confirming the effectiveness of lithium defects in stabilizing the bulk structure during long cycles. Moreover, Grey's group performed in-depth research on the application of ss-NMR in batteries, and their work and corresponding reviews are worthy of study.[302–304]

Mössbauer spectroscopy is a spectroscopic technique based on the Mössbauer effect discovered in 1958 by Rudolf Mössbauer, which is exquisitely sensitive to tiny changes in certain nuclei. The nearly recoil-free emission and absorption of nuclear gamma rays in solids directly reflect the chemical environment transformation. Tarascon *et al.* performed extensive research on batteries by applying Mössbauer spectroscopy. For example, they systematically studied the local structure and redox activity evolution of Sn, Fe, Sb, *etc.* elements in Li-rich oxides.[25,89,306] Taking $Li_2Ru_{0.5}Sn_{0.5}O_3$ as an example, the isomer shift for Sn remained unchanged during the charge/discharge process, indicating that Sn^{4+} is electrochemically inert. A change in quadrupole splitting was only observed in the initial charge process, and the spectrum absorption area was proportional to the Lamb-Mössbauer factor in all cycles, indicating that there is an irreversible local structure distortion around Sn in the first charge process, and the bond between Sn and O decreases when Li ions are removed.

Besides the direct detection of crystal structure changes using the above-mentioned techniques, changes in the elements in the material itself can also indirectly reflect the crystal structure evolutions. In the field of battery research, the newly developed DEMS can provide qualitative and quantitative information on materials by detecting volatile products during electrochemical cycling. It is one of the indispensable tools for studying the electrochemical reaction mechanism of the anionic redox process. The volatile products generated by the electrochemical reaction enter the vacuum system pipeline of the mass spectrometer from the hydrophobic and permeable membrane interface, and the changes in the current of ions with different mass to charge ratios with time are obtained through the mass spectrometer. By using DEMS combined with soft XAS, Xu *et al.* performed a comprehensive study, capturing the oxygen activity in $Li_{1.2}Ni_{0.2}Mn_{0.6}O_2$ and $Li_{1.2}Ni_{0.2}Ru_{0.6}O_2$, which proved that the loss of lattice oxygen ions, O^{2-}, in the form of oxygen was one of the main reasons for the irreversible capacity loss.[307] Moreover, by labeling the oxygen in the oxides or electrolyte with isotope, it is possible to quantitatively determine the origin of the released oxygen at different voltages, which will have critical guiding significance for the design of battery materials, especially for high-voltage cathode materials with oxygen redox activities.[258]

5.2. Element/morphology characterization

The morphology and element distribution in cathodes have a significant impact on the battery performance. Besides the

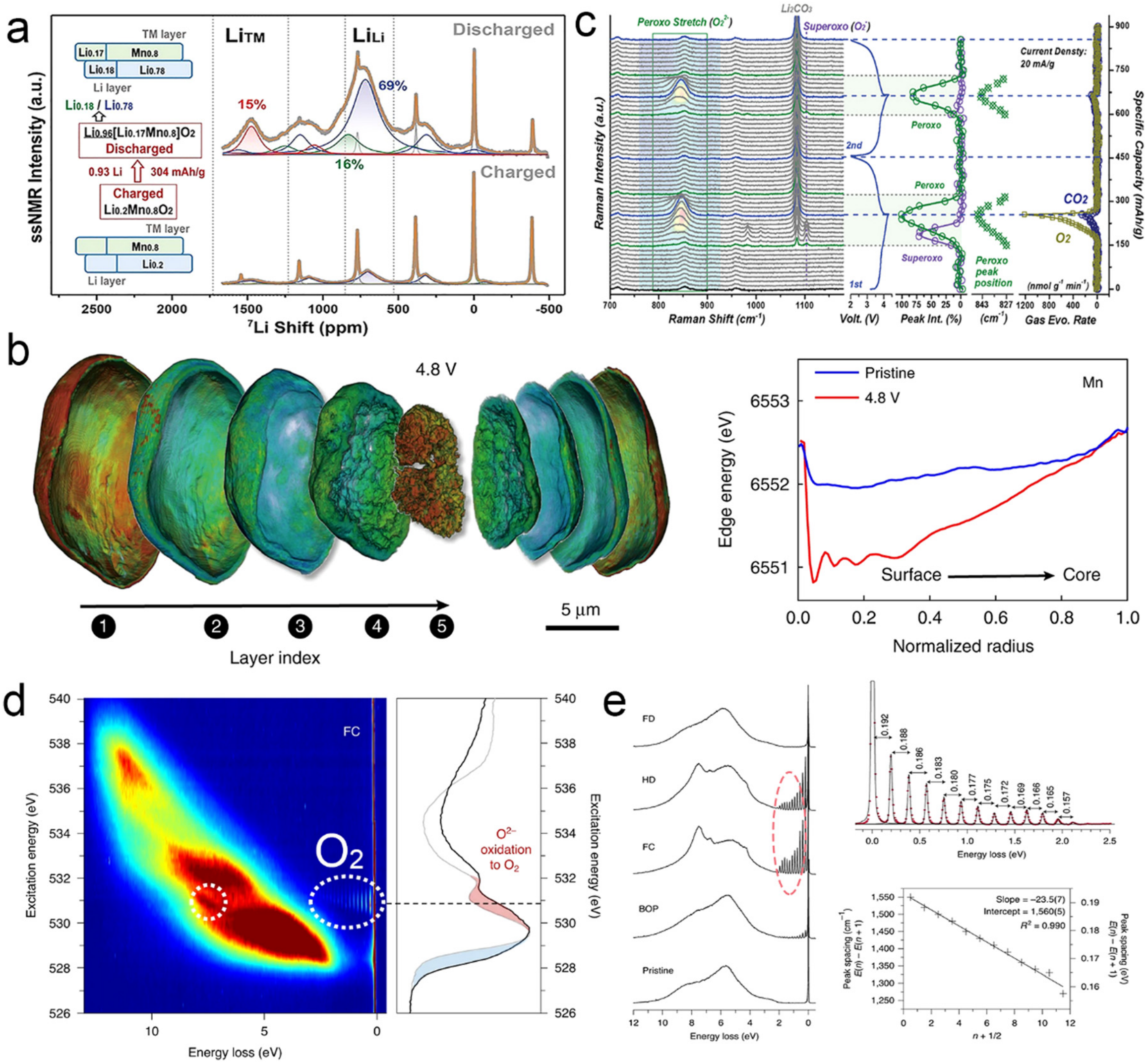

Fig. 8 Typical advanced characterization experimental results: (a) solid-state NMR results of ^{7}Li at different lithium contents. Reproduced with permission.[301] Copyright 2021, Wiley-VCH. (b) Detailed layer-by-layer analysis of the Mn valence states in the charged particles. Reproduced with permission.[305] Copyright 2021, Wiley-VCH. (c) *In situ* Raman spectroscopy of oxygen redox reactions. Reproduced with permission.[90] Copyright 2019, Wiley-VCH. (d) High-resolution RIXS mapping and oxygen partial fluorescence yield soft XAS data. Reproduced with permission.[11] Copyright 2020, Springer Nature. (e) High-resolution RIXS spectra under different charge–discharge states and oxygen molecular vibration spectra demonstrating the formation of oxygen molecules in the full-charged (FC) and half-discharged states (HD). Reproduced with permission.[11] Copyright 2020, Springer Nature.

traditional scanning electron microscopy (SEM) and TEM, many other advanced techniques have been applied to characterize the electrodes. As a representative, 3D-atomic probe tomography (3D-APT) is capable of performing 3D mapping and chemical composition analysis at the atomic scale (depth resolution of ≈0.1–0.3 nm and transverse 0.3–0.5 nm). By accurately recording the time of flight and position of each atom, the 3D structure of the entire sample can be reconstructed. Using 3D-APT, it was directly observed that the loss of Li on the surface of $Li_{1.2}Ni_{0.2}Mn_{0.6}O_2$ led to the migration of Ni from the bulk to the surface, thereby forming an inactive rock-salt structure and deteriorating the battery performance.[308] In addition, time-of-flight secondary ion mass spectrometry (TOF-SIMS) is another newly applied surface-sensitive analytical technique used in battery research, which utilizes a pulsed ion beam to eject molecules from the outermost surface of a sample. After ejection, the particles are accelerated into a "flight tube" and their mass is determined by measuring the exact time they reach the detector. The mass/charge ratios are also measured with a mass spectrometer to determine the elemental, isotopic, or molecular composition of the surface to a depth of 1–2 nm. Through the analysis of the secondary ions, the surface molecules and inorganic elements can be analyzed. Compared with energy-dispersive X-ray spectroscopy (EDS) in SEM/TEM, TOF-SIMS is more accurate and can be used for quantitatively analysis. For instance, Zhu *et al.* conducted a postmortem analysis of a surface Se-substituted $LiCo[O_{2-\delta}Se_{\delta}]$ cathode after 120 cycles by TOF-SIMS. According to the 3D surface reconstruction results, the existence of Se suppressed oxygen evolution and side reactions between oxygen and the electrolyte at high voltage;

therefore the CEI was thinner and contained less fluorides, indicating faster Li^+ ion diffusion channels.[217]

Besides the traditional laboratory-level instruments, recently advanced morphology and valence state characterization techniques based on synchrotron radiation have been increasingly used to obtain more information on electrodes and cells. Scanning transmission X-ray microscopy (STXM) is one type of X-ray microscopy, where X-rays are focused on the sample by a focusing mirror, and then amplified by a Fresnel zone plate and projected onto a detector,[309] forming a projected image with a 2D spatial resolution of 20–30 nm.[310,311] By combining TXM and X-ray absorption near edge structure (XANES), it can not only probe the morphology of the electrode particles but also characterize the elementary valence state distribution present inside.[63] Based on TXM characterization, Jena *et al.* found that the valence state of Mn in $Li_{1.2}Ni_{0.13}Mn_{0.54}Co_{0.13}O_2$ changed with depth.[312] They observed the valence of +4 in the core and surface layer and a valence lower than +4 in the medium part of the charged sample. The charging-induced depth-dependent and non-monotonic change in the transition metal valence in $Li_{1.2}Ni_{0.13}Co_{0.13}Mn_{0.54}O_2$ was different from that in traditional ternary oxide materials, which might be associated with the depth-dependent oxygen redox reactions (Fig. 8b).[305] In addition, it could be clearly seen from TXM-XANES that in $Li_{1.2}Ni_{0.13}Co_{0.13}Mn_{0.54}O_2$, Mn underwent obvious chemical phase separation with the progress of the cycle, while Ni showed almost no change. Therefore, the inhomogeneous phase change in high-voltage LM-LROs exacerbated the deterioration of the material properties.[313]

5.3. Electronic/local structure characterization

The electronic structure and active redox couple of the cathode are highly related to its specific capacity. Currently, the most commonly used technique for probing electronic structure is X-ray photoelectron spectroscopy (XPS). Using an X-ray beam, XPS can identify elements and their chemical state within a material or on its surface. Besides, the overall electronic structure and density of electronic states can also be determined. Tarascon and colleagues studied the voltage fading in Li-rich oxides, $Li_2Ru_{1-y}Sn_yO_3$, and oxygen redox activities in these materials by XPS.[89] Specifically, they found the existence of O_2^{2-} species at 530.5 eV with a lower electronic density compared with O^{2-} ions. Further, the reversible appearance and disappearance of this characteristic peak proved the redox activities of oxygen during the subsequent charge–discharge process. It should be noted that they proposed the reductive coupling mechanism using XPS combined with other techniques, which had an important impact on the progress of anionic redox chemistry.[89,314 318] However, there are some Auger electron peaks associated with certain transition metals, which adversely affect the analysis of the results. Therefore, special silver/magnesium targets or synchrotron radiation XPS are urgently required.

Raman spectroscopy is frequently used to recognize the vibrational modes of molecules. By immersing the electrode into the measuring chamber, *in situ* Raman measurement becomes a powerful technique for dynamically detecting the structure and phase constitution evolution during charge/discharge. Zhou *et al.* were the first to directly visualize the reversible formation of O^-–O^- (peroxo oxygen dimer) bonds in $Li_{1.2}Ni_{0.2}Mn_{0.6}O_2$, with a crucial O–O bond length of 1.3 Å along the *c*-axis direction, using *in situ* surface-enhanced Raman spectroscopy. This observation corresponds to the reversible redox reaction between the O^{2-} and O^- species.[319] They also conducted *in situ* Raman spectroscopy to reveal the oxygen behavior in $Li_2Ni_{1/3}Ru_{2/3}O_3$ (Fig. 8c).[90] A new peak at 827 cm^{-1} was observed due to the formation of O_2^{2-} species during the charging process, which was difficult to be detected by *ex situ* Raman spectroscopy. With continuous charging to high voltage, it shifted to a higher wavenumber, illustrating the shortening of the peroxo O–O bond. However, it disappeared and reappeared in the second cycle, implying the reversibility of O^{2-}/O_2^{2-} redox reactions. Moreover, the superoxo (O_2^-) species appeared at 1104 cm^{-1}, accompanied with the emergence of peroxo O_2^{2-} but were absent in the subsequent cycle, showing unstable behavior.

Another routine laboratory technique for electronic structure clarification is EPR, which is derived from the magnetic resonance of materials with unpaired electrons. Compared to NMR, the spins are excited from the electrons instead of the atomic nuclei in EPR. Tang *et al.* applied EPR for the simultaneous monitoring of both cationic and anionic redox processes in LM-LRO cathode materials, in which they demonstrated the evolution of both transition metal and oxygen redox reactions as well as their intertwined coupling in different LM-LROs.[320] The results showed that the reversible oxygen redox could be stabilized by delocalized Mn and electron holes in Mn-containing oxides. In addition, EPR is an important method to investigate the oxygen defects in the fields of batteries and catalysis.[321,322]

In the case of electron energy loss spectroscopy (EELS) based on TEM, after exposing the specimen to an electron beam with a known, narrow range of kinetic energies, the energy loss of the inelastic scattered electrons is measured. By studying the energy loss distribution of inelastic scattered electrons, detailed chemical environment information of electrons in target atoms can be obtained, which is similar to the characterization method of soft XAS from a synchrotron light source. The biggest advantage of EELS is that the device is feasible for universities and academies, but sacrifices the signal-to-noise ratio. Meng and colleagues studied in detail the surface and bulk changes in the $Li[Ni_xLi_{1/3-2x/3}Mn_{2/3-x/3}]O_2$ cathode before and after cycling using EELS.[323] It was found that the corresponding peak of Mn shifted to a lower energy and displayed a higher L_3/L_2 ratio due to the decrease in oxidation state for surface Mn. Moreover, originating from the oxygen loss and surface rearrangement at high voltage, the pre-edge peak disappeared in the cycled sample, manifesting the readjustment of the unoccupied state of the surface transition metal 3d orbital and M–M bond length during cycling.

XAS is a widely used element-selective technique for determining the local geometric and/or electronic structure of target atoms by measuring the changes in absorption coefficient before and after the sample in a certain energy range.[324–326] Given that the attenuation of X-rays is closely related to the chemical environments of the elements present in the sample, qualitative and quantitative analysis employing XANES and extended X-ray absorption fine structure (EXAFS) can give the bonding states of different atomic bonds, which are suitable for clarifying the redox reactivity and local structural disorder in batteries during charge and discharge. Based on this technique, Tarascon and colleagues found that peroxo species were formed in the charge process of $Li_2Ru_{0.75}Sn_{0.25}O_3$ due to the change in the local bond length of the O–O bond by the anionic redox reaction.[327] Koga *et al.* systematically investigated the correspondence between the atomic and electronic local structures of all three transition metals as well as the voltage decay behavior for $Li_{1.2}Ni_{0.13}Co_{0.13}Mn_{0.54}O_2$ during the initial and second charge/discharge processes by conducting *operando* hard XAS.[328] It demonstrated that oxygen reversibly participated in the redox reactions and released as O_2 partially. Yu *et al.* used XAS to elucidate the changes in the electronic transitions and local structure of $Li_{1.2}Ni_{0.15}Co_{0.1}Mn_{0.55}O_2$ at various state-of-charges. The results indicated that the original Li_2MnO_3 domain in the mixed structure was responsible for the slow Li^+ ion diffusion in LM-LROs.[329]

Compared to hard XAS (photon energy > 3000 eV), soft XAS (photon energy < 1500 eV) has poor penetration ability and is more sensitive to the environment due to the strong absorption of air. Thus, soft XAS experiments have to be performed under high vacuum, making it challenging to perform *operando* characterization. However, comprehensive information can be derived from the surface and bulk of the sample by performing soft XAS in different modes, such as partial fluorescence yield (PFY < 2 nm), total electron yield (TEY: ≈ 10 nm) and total fluorescence yield (TFY > 50 nm).[330–333] In Hy's report employing $Li_{1.2}Mn_{0.6}Ni_{0.2}O_2$ as the research sample, the spectral ratio of oxygen K-edge recording from fluorescent yield (FY, detection depth ≈ 200 nm) mode decreased obviously at the charging plateau of ≈ 4.5 V, while the peak intensities of the Ni and Mn L-edges increased significantly in TEY mode, which was consistent with the transition metal densification model, in which oxygen was released from the surface, accompanied with the migration of transition metals to the bulk.[331]

Unlike XAS, the absorption process in RIXS gives information on the empty electronic states of the central atoms, while the emission gives information about the occupied states. Thus, it is sensitive to measure the valence band structure and related features from the empty band, which can be used to determine the redox reactions for battery materials. For example, conventional O K-edge XAS cannot separate the lattice oxygen signal due to the strong hybridization between the transition metal 3d and O 2p states; however, RIXS can give more detailed chemical state information on the lattice oxygen given that it can further resolve the soft XAS signals. Yang and Devereaux reviewed the difference between soft XAS and RIXS, and they concluded that RIXS is the tool-of-choice to study both the practical issue on reversibility of oxygen redox and the fundamental nature of the bulk.[334] As proven by RIXS mapping under different charge/discharge states, Xu *et al.* demonstrated that the origin of the distinct electrochemical characteristics for $Li_{1.2}Ni_{0.2}Mn_{0.6}O_2$ and $Li_{1.2}Ni_{0.2}Ru_{0.6}O_2$ cathodes was due to the different reactivities of the oxygen redox during cycling.[307] In addition, through detailed analysis of the ultrafine structure near the elastic peak, it was believed that the inelastic peaks appearing at 4.8 V was associated with the O–O vibration of the oxygen molecule, which further confirmed the formation of O_2 along with oxygen redox reactions during the charging process and highlighted the crucial role of RIXS in studying anionic redox activities (Fig. 8d and e).

5.4. Theoretical calculation

Theoretical calculation can unravel the structural stability thermodynamically and clarify the structural evolution from a kinetic point of view, which is beneficial to understand the elusive electrochemical reaction happening in the "black box". As one of the most used and versatile methods in condensed matter physics and computational chemistry, density functional theory (DFT) is adapted in studying the electronic structure of multi-electron systems, especially for molecules and condensed matter. Xia and colleagues compared the stability of regular Li_2RuO_3 and intra-layer disordered Li_2RuO_3 by DFT calculation.[335] Specifically, the length of the Ru–O bond decreased for both regular and intra-layer disordered Li_2RuO_3 during delithiation, but O–O dimerization was absent for the intra-layer disordered one. Then, the relationship between oxygen release and lithium content was calculated based on the Gibbs free energy, and the results further confirmed the superior oxygen stability in intra-layer disordered Li_2RuO_3, even when the Li^+ ions were completely removed. Moreover, Kang and colleagues calculated the migration energy barriers for the transition metals along different crystal planes in O2-type $Li_{0.83}[Li_{0.2}Ni_{0.2}Mn_{0.6}]O_2$ and O3-type $Li[Li_{0.2}Ni_{0.2}Mn_{0.6}]O_2$ cathode materials by DFT.[130] They found that different from O3-type $Li[Li_{0.2}Ni_{0.2}Mn_{0.6}]O_2$, the transition metals in the O2-type structure not only migrated through the tetrahedral intermediate site to the final octahedral site of the Li layer, but also moved to the octahedral intermediate site, and subsequently migrated to the tetrahedral sites of the Li layer. Based on this model, they illustrated that the migration of transition metals was more difficult for the O2-type structure because of its higher site energy. Specifically, the migration of transition metals in the O2-type $Li_{0.83}[Li_{0.2}Ni_{0.2}Mn_{0.6}]O_2$ was more reversible because the transition metals were more likely to stay in the intermediate sites rather than migrate to the final sites in the Li layers due to the stronger repulsion of M–M. F-containing DRXs can stabilize their own structure, but the strong mutual attraction between Li–F limits the intercalation and extraction of lithium ions, and thus providing more Li^+ ions based on a stable structure is the main problem for these types of materials. Ceder and colleagues revealed that Mg doping in F-containing DRXs could strongly alleviate the Li–F locking effect in high-voltage DRXs due to the similar ionic radii between Mg and Li, resulting in a noticeably improved specific capacity.[336] In addition, DFT and other related theoretical calculations have shown great potential and played an important role in the prediction of new high-voltage cathode materials and reaction mechanism analysis.[77,337–341]

6. Conclusions and perspectives

Considering the goal of carbon neutrality, energy storage devices are experiencing unprecedented growth, and thus materials with high energy density are urgently needed. In this case, Li-rich and Ni-rich oxides and LCO represent three of the most promising candidates for high-voltage cathode materials. However, these materials are all subject to anionic redox reaction at high voltage, making a comprehensive and unified understanding of their underlying mechanisms crucial for advancing their practical applications. Although considerable studies have demonstrated the existence of O 2p non-bonding states as a mechanism for anionic redox activity in high-voltage Li-rich cathodes, a significant knowledge gap persists regarding the impact of anionic redox activities on the structural evolution of high-voltage LCO and Ni-rich cathodes. In this review, we propose two-stage anion redox chemistry for LCO with the initial stage being dominated by Co–O covalency, followed by a non-bonding state of vacancies/Li–O–Li resulting from Co migration. Furthermore, we emphasize the origin of anion redox activity in Ni-rich cathodes, specifically the formation of O 2p non-bonding states through Li/Ni mixing and Ni migration during electrochemical cycling. Based on the discussion, we emphasize the unified theoretical framework for anionic redox activity across the three high-voltage cathodes, primarily characterized by the formation of O 2p non-bonding states within the crystal structure, whether arising from the intrinsic crystal structure or from transition metal-lithium mixing during electrochemical cycling.

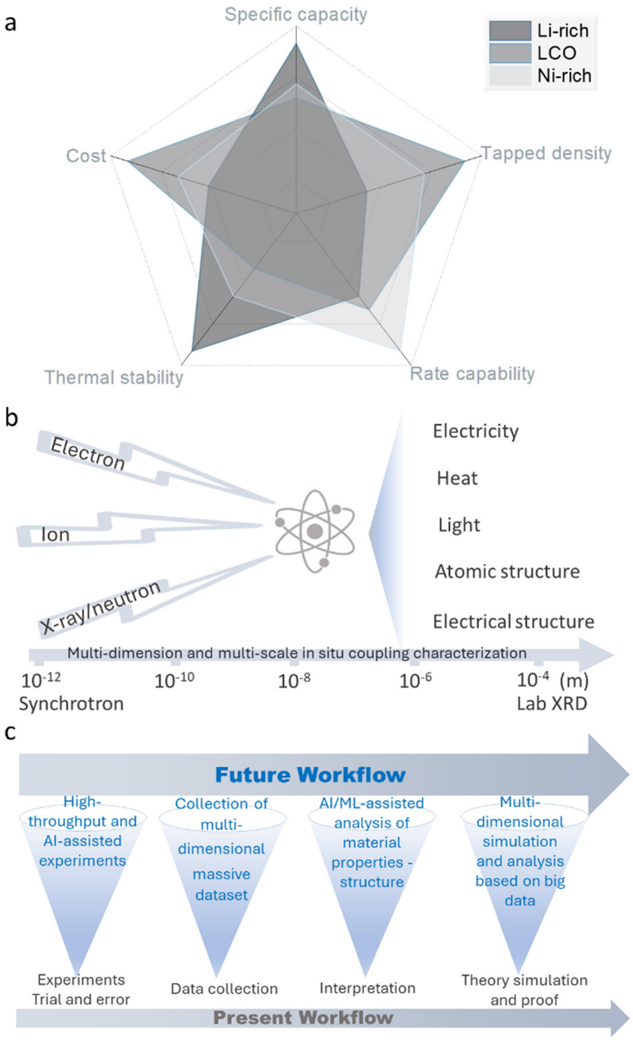

Fig. 9 Comparison of the three high-voltage cathode materials across different dimensions and the future directions of AI and *in situ* characterization in these materials: (a) radar chart comparing Li-rich, LCO and Ni-rich high-voltage cathode materials in terms of specific capacity, tap density, rate capacity, thermal stability and cost. (b) Coupling of multiscale *in situ*/*operando* characterization. (c) Comparative exhibition of the present workflow on cathode materials and a future workflow integrated with AI/ML.

Fig. 9a shows a comparison of the three typical high-voltage cathode materials, *i.e.*, Li-rich and nickel-rich oxides, and LCO, in terms of cost, energy density, specific capacity, thermal stability and rate performance. Purely from the perspective of overcoming mileage anxiety, that is, high capacity, the high-voltage Li-rich oxide cathode material family is the most promising candidates. However, they experience a series of disadvantages, in which voltage attenuation and voltage hysteresis are the most prominent. The origin of these issues is recognized to be oxygen redox reactions. Together with oxygen redox reactions, oxygen evolution occurs, and transition metals undergo migration, both of which cause a phase transition on the surface of the crystal structure. High-voltage LCO materials have the obvious advantage of tap density, which is beneficial for improving the volumetric energy density and reducing production costs. Nevertheless, the structure breakdown and the capacity degradation at high voltage lead to a serious lack of cycle stability. In addition, the high cost of Co also limits its further large-scale promotion in electric vehicles. Lastly, Ni-rich cathode materials exhibit an excellent rate performance, which is crucial for electric vehicles given that they require rapid energy release and charging capabilities during acceleration and braking. These materials enable rapid acceleration, enhance the driving experience, and reduce the charging time. However, Ni-rich cathode materials are prone to structural stability issues under high-voltage and high-rate operations. Their elevated nickel content leads to significant volumetric changes during charge and discharge cycles, and high-voltage cycling induces irreversible phase transformations, which result in structural collapse and capacity degradation.

Nowadays, different development routes should be adopted in view of the difference in the crystal structure of high-voltage cathode materials. Firstly, for high-voltage Li-rich oxides, the anionic redox reaction induces the release of oxygen, transition metal migration, structural reorganization, lattice microcracks, *etc.* All these issues are responsible for the degradation of the electrochemical performance. Therefore, strategies that can

Table 2 Comprehensive overview of the failure mechanisms, their corresponding mitigation strategies, and suitable characterization techniques

	Li-rich cathodes	Ni-rich cathodes	LCO cathodes
Mechanisms	• Voltage fading attributed to oxygen release, transition metal migration, and reduction of Mn and Co. • Voltage hysteresis caused by trapped O_2 molecules and charge transfer with sluggish structural distortion.	• Surface degradation caused by parasitic electrolyte reactions. • Structural changes: cation mixing, phase transition and microcrack. • Thermal instability: oxygen release and active Ni^{4+}.	• Capacity fading caused by phase transitions. • Structural degradation: cobalt dissolution crack of crystal structure. • Thermal instability: oxygen loss.
Strategies	• Surface coatings to suppress side reactions and improve thermal stability. • Doping to stabilize the crystal structure and reduce cation mixing. • Grain boundary engineering to mitigate microcrack formation and improve mechanical stability. • Gradient compositions to minimize surface reactions and maintain high capacity. • Electrolyte additives to enhance CEI stability. New crystal structures such as O2-type Li-rich, ribbon and mesh superstructure to mitigate irreversible transition metal migration and oxygen release.		
Characterizations	• XRD and ND for crystal structure and phase transitions. • TEM and ss-NMR for local crystal structures and the distribution of oxygen vacancies. • DEMS for volatile products and oxygen activity, offering a deeper understanding of the anionic redox processes. Raman spectroscopy for oxygen behaviour during cycling. • TOF-SIMS for elements distribution. • XAS for electronic structure. • RIXS for anion redox chemistry.		

stabilize the oxygen network and suppress oxygen evolution will be effective in improving their cycling performance and capacity retention. In addition, the design of new crystal structures (O2-type Li-rich oxides, ribbon or mesh structures) or element gradient particles is also beneficial for mitigating the voltage decay.

The capacity degradation of high-voltage LCO and Ni-rich cathode materials is primarily caused by their structural instability and cobalt dissolution due to crystal structure bending, cracking and phase transformation. Strategies such as surface coating, doping, and electronic structure regulation can mitigate oxygen release, enhance the structure stability and effectively slow down capacity fading. In addition to the development of high-voltage cathode materials, to achieve their successful application, tailoring proper liquid electrolytes that can withstand high voltage is considered a feasible route. Then, a transition to solid-state and/or ionic liquid electrolytes with higher safety is necessary, although they currently suffer from low conductivity and decomposition at high voltage. Moreover, creating a unified failure theory for various high-voltage cathode materials will greatly promote the development of high-energy-density batteries. To promote the application of high-voltage cathode materials in electric vehicles, their safety must be addressed, especially the concerns related to thermal runaway. Therefore, thermal runaway models, thermal runaway prediction and methods to control thermal runaway without affecting the battery energy density will be the focus of future research.

Obviously, the above-mentioned development goals cannot be achieved without help from advanced characterization techniques.

Although various characterization methods (*in situ* and *ex situ*) have been discussed in detail with respect to crystal structure, element/morphology and electronic/local structure, most of them are operated independently. Thus, to obtain more realistic structural changes during the charging and discharging process and reveal the dynamic reaction mechanism, *in situ* multi-scale non-destructive characterization techniques will be imperative (Fig. 9b). The realization of *in situ* hybrid characterization, especially combinations between techniques from lab and large facilities, such as *in situ* XRD-XAS-Raman and *in situ* tomography-XRD-DEMS, is welcomed by the battery community. Table 2 provides a comprehensive overview of the predominant failure mechanisms, the corresponding mitigation strategies, and the suitable characterization techniques for their identification and analysis. Moreover, with the development of artificial intelligence (AI), machine learning (ML) and material genome databases, material development has moved beyond traditional trial-and-error experimentation methods. In particular, ML can predict the properties of materials and discover new structures suitable for batteries to reduce the experimental time. Moreover, it plays an important role in understanding the reaction mechanism details. However, although theoretical calculation has been widely used, advanced, time-saving and accurate AI/ML algorithms still need to be pushed forward (Fig. 9c). We believe that the combination of experiments, AI/ML and material genome databases will greatly promote the development of the battery industry.

Author contributions

Qingyuan Li: conceptualization (equal), writing – original draft (lead), writing – reviewing and editing (lead), visualization (lead); Dong Zhou: conceptualization (equal), writing – original draft (equal), writing – reviewing and editing (equal), visualization (supporting), visualization (equal); Mihai Chu: writing –

reviewing and editing (supporting), formal analysis (equal); Zhongqing Liu: writing – reviewing and editing (supporting), formal analysis (supporting); Liangtao Yang: writing – reviewing and editing (supporting), formal analysis (equal); Wei Wu: writing – reviewing and editing (supporting), formal analysis (equal); De Ning: writing – reviewing and editing (supporting); Wenyuan Li: writing – reviewing and editing (supporting); Xingbo Liu: writing – reviewing and editing (supporting); Jie Li: conceptualization (equal), formal analysis (equal); writing – reviewing and editing (lead), visualization (equal); Stefano Passerini: conceptualization (equal), formal analysis (equal); writing – reviewing and editing (lead), visualization (equal); Jun Wang: conceptualization (lead), formal analysis (equal); writing – reviewing and editing (lead), visualization (equal).

Data availability

Data availability is not applicable to this article as no new data were created or analysed in this study.

Conflicts of interest

There are no conflicts to declare.

Acknowledgements

The authors are grateful for the financial supports from the National Natural Science Foundation of China (52372211 and 52371225), Shenzhen Basic Research Foundation (JCYJ20230807112503007) and Guangdong Province Major Talent Introducing Program (2021QN020687).

Notes and references

1 Q. Zheng, Y. Yamada, R. Shang, S. Ko, Y.-Y. Lee, K. Kim, E. Nakamura and A. Yamada, *Nat. Energy*, 2020, **5**, 291–298.
2 R. Schmuch, R. Wagner, G. Horpel, T. Placke and M. Winter, *Nat. Energy*, 2018, **3**, 267–278.
3 G. Assat and J.-M. Tarascon, *Nat. Energy*, 2018, **3**, 373–386.
4 M. H. Zhang, D. A. Kitchaev, Z. Lebens-Higgins, J. Vinckeviciute, M. Zuba, P. J. Reeves, C. P. Grey, M. S. Whittingham, L. F. J. Piper, A. van der Ven and Y. S. Meng, *Nat. Rev. Mater.*, 2022, **7**, 522–540.
5 L. Liang, M. Su, Z. Sun, L. Wang, L. Hou, H. Liu, Q. Zhang and C. Yuan, *Sci. Adv.*, 2024, **10**, eado4472.
6 Z. Sun, J. Pan, W. Chen, H. Chen, S. Zhou, X. Wu, Y. Wang, K. Kim, J. Li, H. Liu, Y. Yuan, J. Wang, D. Su, D. L. Peng and Q. Zhang, *Adv. Energy Mater.*, 2023, **14**, 2303165.
7 F. Zhang, Y. Liang, Z. Ye, L. Deng, Y. Guo, P. Qiu, P. Jia, Q. Zhang and L. Zhang, *Chin. Chem. Lett.*, 2024, **35**, 108655.
8 L. Li, L. Fu, M. Li, C. Wang, Z. Zhao, S. Xie, H. Lin, X. Wu, H. Liu, L. Zhang, Q. Zhang and L. Tan, *J. Energy Chem.*, 2022, **71**, 588–594.
9 B. Zhang, Y. Zhang, H. Wu, L. Zeng, X. Wang, H. Liu, X. Wu, J. Chen, H. Zhang, Y. Yan, Y. Tang, H. Huang, L. Zheng, Q. Zhang, Q. Xie, D.-L. Peng, C. Li, Y. Qiao and S.-G. Sun, *Energy Storage Mater.*, 2023, **62**, 102926.
10 W. Ding, H. Ren, Z. Li, M. Shang, Y. Song, W. Zhao, L. Chang, T. Pang, S. Xu, H. Yi, L. Zhou, H. Lin, Q. Zhao and F. Pan, *Adv. Energy Mater.*, 2024, **14**, 2303926.
11 R. A. House, G. J. Rees, M. A. Pérez-Osorio, J.-J. Marie, E. Boivin, A. W. Robertson, A. Nag, M. Garcia-Fernandez, K.-J. Zhou and P. G. Bruce, *Nat. Energy*, 2020, **5**, 777–785.
12 X. Liu, G.-L. Xu, V. S. C. Kolluru, C. Zhao, Q. Li, X. Zhou, Y. Liu, L. Yin, Z. Zhuo, A. Daali, J.-J. Fan, W. Liu, Y. Ren, W. Xu, J. Deng, I. Hwang, D. Ren, X. Feng, C. Sun, L. Huang, T. Zhou, M. Du, Z. Chen, S.-G. Sun, M. K. Y. Chan, W. Yang, M. Ouyang and K. Amine, *Nat. Energy*, 2022, **7**, 808–817.
13 J. J. Marie, R. A. House, G. J. Rees, A. W. Robertson, M. Jenkins, J. Chen, S. Agrestini, M. Garcia-Fernandez, K. J. Zhou and P. G. Bruce, *Nat. Mater.*, 2024, **23**, 818–825.
14 T. Liu, J. Liu, L. Li, L. Yu, J. Diao, T. Zhou, S. Li, A. Dai, W. Zhao, S. Xu, Y. Ren, L. Wang, T. Wu, R. Qi, Y. Xiao, J. Zheng, W. Cha, R. Harder, I. Robinson, J. Wen, J. Lu, F. Pan and K. Amine, *Nature*, 2022, **606**, 305–312.
15 Z. X. Wu, G. F. Zeng, J. H. Yin, C. L. Chiang, Q. H. Zhang, B. D. Zhang, J. K. Chen, Y. W. Yan, Y. L. Tang, H. T. Zhang, S. Y. Zhou, Q. S. Wang, X. X. Kuai, Y. G. Lin, L. Gu, Y. Qiao and S. G. Sun, *ACS Energy Lett.*, 2023, **8**, 4806–4817.
16 E. Hu, Q. Li, X. Wang, F. Meng, J. Liu, J.-N. Zhang, K. Page, W. Xu, L. Gu, R. Xiao, H. Li, X. Huang, L. Chen, W. Yang, X. Yu and X.-Q. Yang, *Joule*, 2021, **5**, 720–736.
17 J. Zhang, D. Wong, Q. Zhang, N. Zhang, C. Schulz, M. Bartkowiak, K. An, L. Gu, Z. Hu and X. Liu, *J. Am. Chem. Soc.*, 2023, **145**, 10208–10219.
18 D. H. Seo, J. Lee, A. Urban, R. Malik, S. Kang and G. Ceder, *Nat. Chem.*, 2016, **8**, 692–697.
19 W. D. Johnston, R. R. Heikes and D. Sestrich, *J. Phys. Chem. Solids*, 1958, **7**, 1–13.
20 W. Kong, D. Wong, K. An, J. Zhang, Z. Chen, C. Schulz, Z. Xu and X. Liu, *Adv. Funct. Mater.*, 2022, **32**, 2202679.
21 C. Nithya, R. Thirunakaran, A. Sivashanmugam and S. Gopukumar, *J. Power Sources*, 2011, **196**, 6788–6793.
22 Q. Liu, X. Su, D. Lei, Y. Qin, J. Wen, F. Guo, Y. A. Wu, Y. Rong, R. Kou, X. Xiao, F. Aguesse, J. Bareño, Y. Ren, W. Lu and Y. Li, *Nat. Energy*, 2018, **3**, 936–943.
23 Z. Dai, Z. Li, R. Chen, F. Wu and L. Li, *Nat. Commun.*, 2023, **14**, 8087.
24 J. Zhang, Q. Zhang, D. Wong, N. Zhang, G. Ren, L. Gu, C. Schulz, L. He, Y. Yu and X. Liu, *Nat. Commun.*, 2021, **12**, 3071.
25 B. Li, M. T. Sougrati, G. Rousse, A. V. Morozov, R. Dedryvere, A. Iadecola, A. Senyshyn, L. Zhang, A. M. Abakumov, M. L. Doublet and J. M. Tarascon, *Nat. Chem.*, 2021, **13**, 1070–1080.
26 T. Ohzuku, A. Ueda and M. Nagayama, *J. Electrochem. Soc.*, 1993, **140**, 1862–1870.
27 T. Ohzuku and Y. Makimura, *Chem. Lett.*, 2001, 642–643.
28 M. Li and J. Lu, *Science*, 2020, **367**, 979–980.
29 A. C. Johnston-Peck, I. Levin, A. A. Herzing and L. A. Bendersky, *Mater. Charact.*, 2016, **119**, 120–128.

30 H. Fujii, K. Ozawa and T. Mochiku, *J. Solid State Chem.*, 2013, **203**, 345–352.

31 Y. Meng, G. Ceder, C. Grey, W.-S. Yoon, M. Jiang, J. Breger and Y. Shao-Horn, *Chem. Mater.*, 2005, **17**, 2386–2394.

32 P. Rozier and J. M. Tarascon, *J. Electrochem. Soc.*, 2015, **162**, A2490–A2499.

33 L. Li, K. S. Lee and L. Lu, *Funct. Mater. Lett.*, 2014, **07**, 1430002.

34 Z. Lu, D. D. MacNeil and J. R. Dahn, *Electrochem. Solid-State Lett.*, 2001, **4**, A191–A194.

35 Y. Zuo, B. Li, N. Jiang, W. Chu, H. Zhang, R. Zou and D. Xia, *Adv. Mater.*, 2018, **30**, e1707255.

36 J. Hong, W. E. Gent, P. Xiao, K. Lim, D. H. Seo, J. Wu, P. M. Csernica, C. J. Takacs, D. Nordlund, C. J. Sun, K. H. Stone, D. Passarello, W. Yang, D. Prendergast, G. Ceder, M. F. Toney and W. C. Chueh, *Nat. Mater.*, 2019, **18**, 256–265.

37 A. J. Perez, Q. Jacquet, D. Batuk, A. Iadecola, M. Saubanère, G. Rousse, D. Larcher, H. Vezin, M.-L. Doublet and J.-M. Tarascon, *Nat. Energy*, 2017, **2**, 954–962.

38 B. Li, R. Shao, H. Yan, L. An, B. Zhang, H. Wei, J. Ma, D. Xia and X. Han, *Adv. Funct. Mater.*, 2016, **26**, 1330–1337.

39 E. C. Self, L. Zou, M.-J. Zhang, R. Opfer, R. E. Ruther, G. M. Veith, B. Song, C. Wang, F. Wang, A. Huq and J. Nanda, *Chem. Mater.*, 2018, **30**, 5061–5068.

40 J. Lee, D. A. Kitchaev, D.-H. Kwon, C.-W. Lee, J. K. Papp, Y.-S. Liu, Z. Lun, R. J. Clément, T. Shi, B. D. McCloskey, J. Guo, M. Balasubramanian and G. Ceder, *Nature*, 2018, **556**, 185–190.

41 J. Lee, A. Urban, X. Li, D. Su, G. Hautier and G. Ceder, *Science*, 2014, **343**, 519–522.

42 W. D. Richards, S. T. Dacek, D. A. Kitchaev and G. Ceder, *Adv. Energy Mater.*, 2018, **8**, 1701533.

43 E. Zhao, Q. Li, F. Meng, J. Liu, J. Wang, L. He, Z. Jiang, Q. Zhang, X. Yu, L. Gu, W. Yang, H. Li, F. Wang and X. Huang, *Angew. Chem., Int. Ed.*, 2019, **58**, 4323–4327.

44 M. A. Cambaz, A. Urban, S. A. Pervez, H. Geßwein, A. Schiele, A. A. Guda, A. L. Bugaev, A. Mazilkin, T. Diemant, R. J. Behm, T. Brezesinski and M. Fichtner, *Chem. Mater.*, 2020, **32**, 3447–3461.

45 R. Sharpe, R. A. House, M. J. Clarke, D. Forstermann, J. J. Marie, G. Cibin, K. J. Zhou, H. Y. Playford, P. G. Bruce and M. S. Islam, *J. Am. Chem. Soc.*, 2020, **142**, 21799–21809.

46 H. Chung, Z. Lebens-Higgins, B. Sayahpour, C. Mejia, A. Grenier, G. E. Kamm, Y. Li, R. Huang, L. F. J. Piper, K. W. Chapman, J.-M. Doux and Y. S. Meng, *J. Mater. Chem. A*, 2021, **9**, 1720–1732.

47 B. Li, K. Kumar, I. Roy, A. V. Morozov, O. V. Emelyanova, L. Zhang, T. Koc, S. Belin, J. Cabana, R. Dedryvere, A. M. Abakumov and J. M. Tarascon, *Nat. Mater.*, 2022, **21**, 1165–1174.

48 A. Urban, I. Matts, A. Abdellahi and G. Ceder, *Adv. Energy Mater.*, 2016, **6**, 1600488.

49 D. Chen, J. Ahn and G. Chen, *ACS Energy Lett.*, 2021, **6**, 1358–1376.

50 K. Kang and G. Ceder, *Phys. Rev. B: Condens. Matter Mater. Phys.*, 2006, **74**, 094105.

51 K. Kang, Y. S. Meng, J. Breger, C. P. Grey and G. Ceder, *Science*, 2006, **311**, 977–980.

52 G. Zhao, T. Zhang, R. Wang, N. Zhang, L. Zheng, X. Ma, J. Yang and X. Liu, *Small*, 2024, **20**, e2401839.

53 H. Liu, W. Hua, S. Kunz, M. Bianchini, H. Li, J. Peng, J. Lin, O. Dolotko, T. Bergfeldt, K. Wang, C. Kubel, P. Nagel, S. Schuppler, M. Merz, B. Ying, K. Kleiner, S. Mangold, D. Wong, V. Baran, M. Knapp, H. Ehrenberg and S. Indris, *Nat. Commun.*, 2024, **15**, 9981.

54 J. Sun, C. Sheng, X. Cao, P. Wang, P. He, H. Yang, Z. Chang, X. Yue and H. Zhou, *Adv. Funct. Mater.*, 2021, **32**, 2110295.

55 Z. Hao, H. Sun, Y. Ni, G. Yang, Z. Yang, Z. Hao, R. Wang, P. Yang, Y. Lu, Q. Zhao, W. Xie, Z. Yan, W. Zhang and J. Chen, *Adv. Mater.*, 2024, **36**, e2307617.

56 Y. Yang, T. Luo, Y. Zuo, H. Wang, C. Gao, J. Cai, T. Yang, W. Xiao, Y. Yu and D. Xia, *Adv. Mater.*, 2024, e2414786, DOI: 10.1002/adma.202414786.

57 G. Lim, M. K. Cho, J. Choi, K.-J. Zhou, D. Shin, S. Jeon, M. Kwon, A. R. Jeon, J. Choi, S. S. Sohn, M. Lee and J. Hong, *Energy Environ. Sci.*, 2024, **17**, 9623–9634.

58 D. Luo, H. Zhu, Y. Xia, Z. Yin, Y. Qin, T. Li, Q. Zhang, L. Gu, Y. Peng, J. Zhang, K. M. Wiaderek, Y. Huang, T. Yang, Y. Tang, S. Lan, Y. Ren, W. Lu, C. M. Wolverton and Q. Liu, *Nat. Energy*, 2023, **8**, 1078–1087.

59 H.-Y. Jang, D. Eum, J. Cho, J. Lim, Y. Lee, J.-H. Song, H. Park, B. Kim, D.-H. Kim and S.-P. Cho, *Nat. Commun.*, 2024, **15**, 1288.

60 Z. Cai, B. Ouyang, H.-M. Hau, T. Chen, R. Giovine, K. P. Koirala, L. Li, H. Ji, Y. Ha, Y. Sun, J. Huang, Y. Chen, V. Wu, W. Yang, C. Wang, R. J. Clément, Z. Lun and G. Ceder, *Nat. Energy*, 2023, **9**, 27–36.

61 J. Qian, Y. Ha, K. P. Koirala, D. Huang, Z. Huang, V. S. Battaglia, C. Wang, W. Yang and W. Tong, *Adv. Funct. Mater.*, 2023, **33**, 2205972.

62 J. Huang, B. Ouyang, Y. Zhang, L. Yin, D. H. Kwon, Z. Cai, Z. Lun, G. Zeng, M. Balasubramanian and G. Ceder, *Nat. Mater.*, 2023, **22**, 353–361.

63 T. Liu, L. Yu, J. Liu, A. Dai, T. Zhou, J. Wang, W. Huang, L. Li, M. Li, T. Li, X. Huang, X. Xiao, M. Ge, L. Ma, Z. Zhuo, R. Amine, Y. S. Chu, W.-K. Lee, J. Wen and K. Amine, *Nat. Energy*, 2024, **9**, 1252–1263.

64 Y. Gao, J. Park and X. Liang, *ACS Appl. Energy Mater.*, 2020, **3**, 8978–8987.

65 J. Zheng, S. Myeong, W. Cho, P. Yan, J. Xiao, C. Wang, J. Cho and J.-G. Zhang, *Adv. Energy Mater.*, 2017, **7**, 1601284.

66 K. Wu, Z. Li and X. Chen, *Adv. Funct. Mater.*, 2024, **34**, 2315327.

67 Z. Zhang, J. Wang, X. Sun, C. Sheng, M. Cheng, H. Liu, Y. Wang, H. Zhou and P. He, *Adv. Funct. Mater.*, 2024, **34**, 2411409.

68 Z. Zhuang, J. Wang, K. Jia, G. Ji, J. Ma, Z. Han, Z. Piao, R. Gao, H. Ji, X. Zhong, G. Zhou and H. M. Cheng, *Adv. Mater.*, 2023, **35**, e2212059.

69 Q. Wang, Z. Yao, J. Wang, H. Guo, C. Li, D. Zhou, X. Bai, H. Li, B. Li, M. Wagemaker and C. Zhao, *Nature*, 2024, **629**, 341–347.

70 J. Hong, H.-D. Lim, M. Lee, S.-W. Kim, H. Kim, S.-T. Oh, G.-C. Chung and K. Kang, *Chem. Mater.*, 2012, **24**, 2692–2697.

71 J.-S. Kim, C. S. Johnson, J. T. Vaughey, M. M. Thackeray, S. A. Hackney, W. Yoon and C. P. Grey, *Chem. Mater.*, 2004, **16**, 1996–2006.

72 S. Hy, F. Felix, J. Rick, W.-N. Su and B. J. Hwang, *J. Am. Chem. Soc.*, 2014, **136**, 999–1007.

73 K. Hu, H. Tang, B. Zheng, L. Yu, F. Xiong, H. Li, L. Qiu, F. Wan, Y. Song, B. Zhong, Z. Wu and X. Guo, *Angew. Chem., Int. Ed.*, 2025, **64**, e202413563.

74 B. Kim, P. Zhong, Y. Choi, S. Anand, H. M. Hau, B. Deng and G. Ceder, *J. Am. Chem. Soc.*, 2025, **147**, 223–233.

75 H. Koga, L. Croguennec, M. Ménétrier, K. Douhil, S. Belin, L. Bourgeois, E. Suard, F. Weill and C. Delmas, *J. Electrochem. Soc.*, 2013, **160**, A786–A792.

76 M. C. López, G. F. Ortiz, P. Lavela, J. L. Tirado, R. Stoyanova and E. Zhecheva, *Chem. Mater.*, 2013, **25**, 4025–4035.

77 M. Ben Yahia, J. Vergnet, M. Saubanere and M. L. Doublet, *Nat. Mater.*, 2019, **18**, 496–502.

78 Y. Xie, M. Saubanère and M. L. Doublet, *Energy Environ. Sci.*, 2017, **10**, 266–274.

79 M. Okubo and A. Yamada, *ACS Appl. Mater. Interfaces*, 2017, **9**, 36463–36472.

80 M. M. Rahman and F. Lin, *Matter*, 2021, **4**, 490–527.

81 Y. Zhang, M. Wu, J. Ma, G. Wei, Y. Ling, R. Zhang and Y. Huang, *ACS Cent. Sci.*, 2020, **6**, 232–240.

82 K. Zhang, J. Qi, J. Song, Y. Zuo, Y. Yang, T. Yang, T. Chen, X. Liu, L. Chen and D. Xia, *Adv. Mater.*, 2022, **34**, e2109564.

83 K. Luo, M. R. Roberts, N. Guerrini, N. Tapia-Ruiz, R. Hao, F. Massel, D. M. Pickup, S. Ramos, Y. S. Liu, J. Guo, A. V. Chadwick, L. C. Duda and P. G. Bruce, *J. Am. Chem. Soc.*, 2016, **138**, 11211–11218.

84 Q. Li, D. Ning, D. Zhou, K. An, D. Wong, L. Zhang, Z. Chen, G. Schuck, C. Schulz, Z. Xu, G. Schumacher and X. Liu, *J. Mater. Chem. A*, 2020, **8**, 7733–7745.

85 L. Nie, Z. Wang, X. Zhao, S. Chen, Y. He, H. Zhao, T. Gao, Y. Zhang, L. Dong, F. Kim, Y. Yu and W. Liu, *Nano Lett.*, 2021, **21**, 8370–8377.

86 J. Zhang, F. Cheng, S. Chou, J. Wang, L. Gu, H. Wang, H. Yoshikawa, Y. Lu and J. Chen, *Adv. Mater.*, 2019, **31**, 1901808.

87 S. Kim, M. Aykol, V. I. Hegde, Z. Lu, S. Kirklin, J. R. Croy, M. M. Thackeray and C. Wolverton, *Energy Environ. Sci.*, 2017, **10**, 2201–2211.

88 E. McCalla, A. M. Abakumov, M. Saubanere, D. Foix, E. J. Berg, G. Rousse, M. L. Doublet, D. Gonbeau, P. Novak, G. Van Tendeloo, R. Dominko and J. M. Tarascon, *Science*, 2015, **350**, 1516–1521.

89 M. Sathiya, G. Rousse, K. Ramesha, C. P. Laisa, H. Vezin, M. T. Sougrati, M. L. Doublet, D. Foix, D. Gonbeau, W. Walker, A. S. Prakash, M. Ben Hassine, L. Dupont and J. M. Tarascon, *Nat. Mater.*, 2013, **12**, 827–835.

90 X. Li, Y. Qiao, S. Guo, K. Jiang, M. Ishida and H. Zhou, *Adv. Mater.*, 2019, **31**, 1807825.

91 Z. Liu, Y. Zeng, J. Tan, H. Wang, Y. Zhu, X. Geng, P. Guttmann, X. Hou, Y. Yang, Y. Xu, P. Cloetens, D. Zhou, Y. Wei, J. Lu, J. Li, B. Liu, M. Winter, R. Kostecki, Y. Lin and X. He, *Nat. Nanotechnol.*, 2024, **19**, 1821–1830.

92 H. Zheng, M. Fan, C. Zhang, W. He, G. Gao, Y. Liu, L. Wang, Q. Xie, D. L. Peng and J. Lu, *Adv. Mater.*, 2024, **36**, e2414443.

93 F. Li, Y. Lin, J. Liu, J. Chen, X. Wan, L. Zhao, L. Xi, Z. Li, H. Zhang, X. Xu, Z. Zhou, B. Su, M. Zhu and J. Liu, *Energy Environ. Sci.*, 2025, **18**, 1241–1254.

94 K. Zhang, Y. Chen, Y. Zhu, Q. Zheng, Y. Tang, D. Yu, Q. Liu, H. Luo, J. Yin, L. Zeng, W. Jiao, N. Liu, Q. Wang, L. Zheng, J. Zhang, Y. Wang, B. Zhang, Y. Yan, H. Huang, C. H. Shen, Y. Qiao and S. G. Sun, *Angew. Chem., Int. Ed.*, 2024, e202419909, DOI: 10.1002/anie.202419909.

95 Z. Jiang, K. Zhang, Q. Ding, C. Gao, Y. Zuo, H. Wang, J. Cai, B. Li, X. Ai and D. Xia, *J. Am. Chem. Soc.*, 2025, **147**, 3062–3071.

96 P. M. Csernica, K. McColl, G. M. Busse, K. Lim, D. F. Rivera, D. A. Shapiro, M. S. Islam and W. C. Chueh, *Nat. Mater.*, 2025, **24**, 92–100.

97 R. A. House, G. J. Rees, K. McColl, J. J. Marie, M. Garcia-Fernandez, A. Nag, K. J. Zhou, S. Cassidy, B. J. Morgan, M. S. Islam and P. G. Bruce, *Nat. Energy*, 2023, **8**, 351–360.

98 T. Cui, J. Xu, X. Wang, L. Liu, Y. Xiang, H. Zhu, X. Li and Y. Fu, *Nat. Commun.*, 2024, **15**, 4742.

99 K. McColl, S. W. Coles, P. Zarabadi-Poor, B. J. Morgan and M. S. Islam, *Nat. Mater.*, 2024, **23**, 826–833.

100 F. Zou, S. Lee, L. Lyu, J. Zhang, S. Kang, G. Kim, H. Lee, S. Park, G.-H. Lee, K.-W. Nam and Y.-M. Kang, *ACS Energy Lett.*, 2024, **9**, 6011–6021.

101 B. Chu, Y.-J. Guo, J.-L. Shi, Y.-X. Yin, T. Huang, H. Su, A. Yu, Y.-G. Guo and Y. Li, *J. Power Sources*, 2022, **544**, 231873.

102 T. Mizokawa, Y. Wakisaka, T. Sudayama, C. Iwai, K. Miyoshi, J. Takeuchi, H. Wadati, D. G. Hawthorn, T. Z. Regier and G. A. Sawatzky, *Phys. Rev. Lett.*, 2013, **111**, 056404.

103 X.-H. Long, Y.-R. Wu, N. Zhang, P.-F. Yu, X.-F. Feng, S. Zheng, J.-M. Fu, X.-S. Liu, N. Liu, M. Wang, L.-M. Xu, J.-M. Chen and J.-M. Lee, *Chin. Phys. B*, 2018, **27**, 107802.

104 Z. Bi, Z. Yi, L. Zhang, G. Wang, A. Zhang, S. Liao, Q. Zhao, Z. Peng, L. Song, Y. Wang, Z. Zhao, S. Wei, W. Zhao, X. Shi, M. Li, N. Ta, J. Mi, S. Li, P. Das, Y. Cui, C. Chen, F. Pan and Z.-S. Wu, *Energy Environ. Sci.*, 2024, **17**, 2765–2775.

105 B. Hu, F. Geng, M. Shen, C. Zhao, Q. Qiu, Y. Lin, C. Chen, W. Wen, S. Zheng, X. Hu, C. Li and B. Hu, *J. Power Sources*, 2021, **516**, 230661.

106 Z. Yao, T. Fu, T. Pan, Z. Jiang, X. Fan, S. Liu, Q. Guo, Y. Li, C. Zheng and W. Sun, *Adv. Funct. Mater.*, 2024, **34**, 2408152.

107 Z. W. Lebens-Higgins, N. V. Faenza, M. D. Radin, H. Liu, S. Sallis, J. Rana, J. Vinckeviciute, P. J. Reeves, M. J. Zuba, F. Badway, N. Pereira, K. W. Chapman, T.-L. Lee, T. Wu, C. P. Grey, B. C. Melot, A. Van Der Ven, G. G. Amatucci,

W. Yang and L. F. J. Piper, *Mater. Horiz.*, 2019, **6**, 2112–2123.

108 J. Liu, Z. Du, X. Wang, S. Tan, X. Wu, L. Geng, B. Song, P.-H. Chien, S. M. Everett and E. Hu, *Energy Environ. Sci.*, 2021, **14**, 6441–6454.

109 A. R. Genreith-Schriever, H. Banerjee, A. S. Menon, E. N. Bassey, L. F. J. Piper, C. P. Grey and A. J. Morris, *Joule*, 2023, **7**, 1623–1640.

110 G.-H. Lee, S. Lee, J. Zhang, B. L. D. Rinkel, M. J. Crafton, Z. Zhuo, Y. Choi, J. Li, J. Yang, J. W. Heo, B. Park, B. D. McCloskey, M. Avdeev, W. Yang and Y.-M. Kang, *Energy Environ. Sci.*, 2024, **17**, 9154–9163.

111 L. An, J. E. N. Swallow, P. Cong, R. Zhang, A. D. Poletayev, E. Bjorklund, P. N. Didwal, M. W. Fraser, L. A. H. Jones, C. M. E. Phelan, N. Ramesh, G. Harris, C. J. Sahle, P. Ferrer, D. C. Grinter, P. Bencok, S. Hayama, M. S. Islam, R. House, P. D. Nellist, R. J. Green, R. J. Nicholls and R. S. Weatherup, *Energy Environ. Sci.*, 2024, **17**, 8379–8391.

112 M. Juelsholt, J. Chen, M. A. Pérez-Osorio, G. J. Rees, S. De Sousa Coutinho, H. E. Maynard-Casely, J. Liu, M. Everett, S. Agrestini, M. Garcia-Fernandez, K.-J. Zhou, R. A. House and P. G. Bruce, *Energy Environ. Sci.*, 2024, **17**, 2530–2540.

113 Z. Lu, J. Zhang, Q. Zhang, D. Wong, W. Yin, N. Zhang, Z. Chen, L. Gu, Z. Hu and X. Liu, *Adv. Sci.*, 2023, **10**, e2206442.

114 M. J. W. Ogley, A. S. Menon, G. C. Pandey, G. J. Páez Fajardo, B. J. Johnston, I. McClelland, V. Majherova, S. Huband, D. Tripathy, I. Temprano, S. Agrestini, V. Celorrio, G. E. Pérez, S. G. Booth, C. P. Grey, S. A. Cussen and L. F. J. Piper, *Joule*, 2025, **9**, 101775.

115 Y. Jia, X. Hou, K. Li, L. Wang, M. Zhang, Z. Li, X. Xu and J. Zheng, *Energy Storage Mater.*, 2024, **71**, 103632.

116 M. Li, J. Lu, Z. Chen and K. Amine, *Adv. Mater.*, 2018, **30**, 1800561.

117 W. He, W. Guo, H. Wu, L. Lin, Q. Liu, X. Han, Q. Xie, P. Liu, H. Zheng, L. Wang, X. Yu and D. L. Peng, *Adv. Mater.*, 2021, **33**, e2005937.

118 S. Zhao, Z. Guo, K. Yan, S. Wan, F. He, B. Sun and G. Wang, *Energy Storage Mater.*, 2021, **34**, 716–734.

119 Y. Wu, C. Ma, J. Yang, Z. Li, L. F. Allard, C. Liang and M. Chi, *J. Mater. Chem. A*, 2015, **3**, 5385–5391.

120 J. Wang, X. He, E. Paillard, N. Laszczynski, J. Li and S. Passerini, *Adv. Energy Mater.*, 2016, **6**, 1600906.

121 E. Boivin, N. Guerrini, R. A. House, J. G. Lozano, L. Y. Jin, G. J. Rees, J. W. Somerville, C. Kuss, M. R. Roberts and P. G. Bruce, *Adv. Funct. Mater.*, 2021, **31**, 2003660.

122 Z. Yang, J. Zhong, J. Li, Y. Liu, B. Niu and F. Kang, *Ceram. Int.*, 2019, **45**, 439–448.

123 H. Yu, Y. G. So, Y. Ren, T. Wu, G. Guo, R. Xiao, J. Lu, H. Li, Y. Yang, H. Zhou, R. Wang, K. Amine and Y. Ikuhara, *J. Am. Chem. Soc.*, 2018, **140**, 15279–15289.

124 E. Zhao, L. He, B. Wang, X. Li, J. Zhang, Y. Wu, J. Chen, S. Zhang, T. Liang, Y. Chen, X. Yu, H. Li, L. Chen, X. Huang, H. Chen and F. Wang, *Energy Storage Mater.*, 2019, **16**, 354–363.

125 D. Chen, W. H. Kan and G. Chen, *Adv. Energy Mater.*, 2019, **9**, 1901255.

126 M. Sathiya, A. M. Abakumov, D. Foix, G. Rousse, K. Ramesha, M. Saubanere, M. L. Doublet, H. Vezin, C. P. Laisa, A. S. Prakash, D. Gonbeau, G. VanTendeloo and J. M. Tarascon, *Nat. Mater.*, 2015, **14**, 230–238.

127 W. H. Kan, B. Deng, Y. Xu, A. K. Shukla, T. Bo, S. Zhang, J. Liu, P. Pianetta, B.-T. Wang, Y. Liu and G. Chen, *Chem*, 2018, **4**, 2108–2123.

128 Y. Li, S. Xu, W. Zhao, Z. Chen, Z. Chen, S. Li, J. Hu, B. Cao, J. Li, S. Zheng, Z. Chen, T. Zhang, M. Zhang and F. Pan, *Energy Storage Mater.*, 2022, **45**, 422–431.

129 G. Choi, U. Chang, J. Lee, K. Park, H. Kwon, H. Lee, Y.-I. Kim, J. H. Seo, Y.-C. Park, I. Park, J. Kim, S. Lee, J. Choi, B. Yu, J.-H. Song, H. Shin, S.-W. Baek, S. K. Lee, H. Park and K. Jung, *Energy Environ. Sci.*, 2024, **17**, 4634–4645.

130 D. Eum, B. Kim, S. J. Kim, H. Park, J. Wu, S. P. Cho, G. Yoon, M. H. Lee, S. K. Jung, W. Yang, W. M. Seong, K. Ku, O. Tamwattana, S. K. Park, I. Hwang and K. Kang, *Nat. Mater.*, 2020, **19**, 419–427.

131 H. Y. Jang, D. Eum, J. Cho, J. Lim, Y. Lee, J. H. Song, H. Park, B. Kim, D. H. Kim, S. P. Cho, S. Jo, J. H. Heo, S. Lee, J. Lim and K. Kang, *Nat. Commun.*, 2024, **15**, 1288.

132 E. Hu, X. Yu, R. Lin, X. Bi, J. Lu, S. Bak, K.-W. Nam, H. L. Xin, C. Jaye, D. A. Fischer, K. Amine and X.-Q. Yang, *Nat. Energy*, 2018, **3**, 690–698.

133 B. Li, Z. Zhuo, L. Zhang, A. Iadecola, X. Gao, J. Guo, W. Yang, A. V. Morozov, A. M. Abakumov and J. M. Tarascon, *Nat. Mater.*, 2023, **22**, 1370–1379.

134 J. Feng, Y.-S. Jiang, F.-D. Yu, W. Ke, L.-F. Que, J.-G. Duh and Z.-B. Wang, *J. Energy Chem.*, 2022, **66**, 666–675.

135 Q. Li, D. Ning, D. Zhou, K. An, G. Schuck, D. Wong, W. Kong, C. Schulz, G. Schumacher and X. Liu, *Chem. Mater.*, 2020, **32**, 9404–9414.

136 S. Sharifi-Asl, J. Lu, K. Amine and R. Shahbazian-Yassar, *Adv. Energy Mater.*, 2019, **9**, 1900551.

137 R.-P. Qing, J.-L. Shi, D.-D. Xiao, X.-D. Zhang, Y.-X. Yin, Y.-B. Zhai, L. Gu and Y.-G. Guo, *Adv. Energy Mater.*, 2016, **6**, 1501914.

138 M. Zhao and Q. Chen, *Ionics*, 2021, **27**, 961–971.

139 Z. Zhu, R. Gao, I. Waluyo, Y. Dong, A. Hunt, J. Lee and J. Li, *Adv. Energy Mater.*, 2020, **10**, 2001120.

140 C. Chen, W. Yao, Q. He, M. Ashuri, J. Kaduk, Y. Liu and L. Shaw, *ACS Appl. Energy Mater.*, 2019, **2**, 3098–3113.

141 J. Zhang, R. Gao, L. Sun, H. Zhang, Z. Hu and X. Liu, *Electrochim. Acta*, 2016, **209**, 102–110.

142 P. Guan, L. Zhou, Z. Yu, Y. Sun, Y. Liu, F. Wu, Y. Jiang and D. Chu, *J. Energy Chem.*, 2020, **43**, 220–235.

143 W. Zhang, Y. Sun, H. Deng, J. Ma, Y. Zeng, Z. Zhu, Z. Lv, H. Xia, X. Ge, S. Cao, Y. Xiao, S. Xi, Y. Du, A. Cao and X. Chen, *Adv. Mater.*, 2020, **32**, e2000496.

144 S. Maiti, H. Sclar, R. Sharma, N. Vishkin, M. Fayena-Greenstein, J. Grinblat, M. Talianker, L. Burstein, N. Solomatin, O. Tiurin, Y. Ein-Eli, M. Noked, B. Markovsky and D. Aurbach, *Adv. Funct. Mater.*, 2020, **31**, 2008083.

145 X. Wen, K. Liang, L. Tian, K. Shi and J. Zheng, *Electrochim. Acta*, 2018, **260**, 549–556.

146 P. Zhou, Z. Zhang, H. Meng, Y. Lu, J. Cao, F. Cheng, Z. Tao and J. Chen, *Nanoscale*, 2016, **8**, 19263–19269.

147 Y. Seok Jung, A. S. Cavanagh, Y. Yan, S. M. George and A. Manthiram, *J. Electrochem. Soc.*, 2011, **158**, A1298–A1302.

148 Y. Wei, J. Cheng, D. Li, Y. Li, Z. Zeng, H. Liu, H. Zhang, F. Ji, X. Geng, J. Lu and L. Ci, *Adv. Funct. Mater.*, 2023, **33**, 2214775.

149 L. Wang, G. Liu, R. Xu, X. Wang, L. Wang, Z. Yao, C. Zhan and J. Lu, *Adv. Energy Mater.*, 2023, **13**, 2203999.

150 M. Li, H. Wang, L. Zhao, F. Zhang and D. He, *J. Solid State Chem.*, 2019, **272**, 38–46.

151 J. Zheng, M. Gu, J. Xiao, B. J. Polzin, P. Yan, X. Chen, C. Wang and J.-G. Zhang, *Chem. Mater.*, 2014, **26**, 6320–6327.

152 J. M. Zheng, Z. R. Zhang, X. B. Wu, Z. X. Dong, Z. Zhu and Y. Yang, *J. Electrochem. Soc.*, 2008, **155**, A775–A782.

153 Q. Wang, L. Liu, H. Li, G. Yang, A. N. Alodhayb and J. Ma, *J. Mater. Sci. Technol.*, 2025, **207**, 274–294.

154 P. P. Dahiya, C. Ghanty, K. Sahoo, S. Basu and S. B. Majumder, *J. Electrochem. Soc.*, 2018, **165**, A3114–A3124.

155 L. Nation, Y. Wu, X. Liu, M. Chi, Y. Wu, Y. Qi and B. W. Sheldon, *Phys. Chem. Chem. Phys.*, 2021, **23**, 2780–2791.

156 Y. Liu, B. He, Q. Li, H. Liu, L. Qiu, J. Liu, W. Xiang, Y. Liu, G. Wang, Z. Wu and X. Guo, *Mater. Res. Bull.*, 2020, **130**, 110923.

157 J. Billaud, D. Sheptyakov, S. Sallard, D. Leanza, M. Talianker, J. Grinblat, H. Sclar, D. Aurbach, P. Novák and C. Villevieille, *J. Mater. Chem. A*, 2019, **7**, 15215–15224.

158 N. Phattharasupakun, C. Geng, M. B. Johnson, R. Väli, A. Liu, Y. Liu, M. Sawangphruk and J. R. Dahn, *J. Electrochem. Soc.*, 2020, **167**, 120531.

159 B. Zhang, Y. Zhang, X. Wang, H. Liu, Y. Yan, S. Zhou, Y. Tang, G. Zeng, X. Wu, H. G. Liao, Y. Qiu, H. Huang, L. Zheng, J. Xu, W. Yin, Z. Huang, Y. Xiao, Q. Xie, D. L. Peng, C. Li, Y. Qiao and S. G. Sun, *J. Am. Chem. Soc.*, 2023, **145**, 8700–8713.

160 J. Wu, Z. Ju, X. Zhang, A. C. Marschilok, K. J. Takeuchi, H. Wang, E. S. Takeuchi and G. Yu, *Adv. Mater.*, 2022, **34**, e2202780.

161 X. Ju, X. Hou, Z. Liu, H. Zheng, H. Huang, B. Qu, T. Wang, Q. Li and J. Li, *J. Power Sources*, 2019, **437**, 226902.

162 Z. Zhu, D. Yu, Y. Yang, C. Su, Y. Huang, Y. Dong, I. Waluyo, B. Wang, A. Hunt, X. Yao, J. Lee, W. Xue and J. Li, *Nat. Energy*, 2019, **4**, 1049–1058.

163 N. Yabuuchi, M. Nakayama, M. Takeuchi, S. Komaba, Y. Hashimoto, T. Mukai, H. Shiiba, K. Sato, Y. Kobayashi, A. Nakao, M. Yonemura, K. Yamanaka, K. Mitsuhara and T. Ohta, *Nat. Commun.*, 2016, **7**, 13814.

164 Y. Ma, Y. Ma, Q. Wang, S. Schweidler, M. Botros, T. Fu, H. Hahn, T. Brezesinski and B. Breitung, *Energy Environ. Sci.*, 2021, **14**, 2883–2905.

165 Q. Wang, A. Sarkar, D. Wang, L. Velasco, R. Azmi, S. S. Bhattacharya, T. Bergfeldt, A. Düvel, P. Heitjans, T. Brezesinski, H. Hahn and B. Breitung, *Energy Environ. Sci.*, 2019, **12**, 2433–2442.

166 S. Schweidler, M. Botros, F. Strauss, Q. S. Wang, Y. J. Ma, L. Velasco, G. C. Marques, A. Sarkar, C. Kübel, H. Hahn, J. Aghassi-Hagmann, T. Brezesinski and B. Breitung, *Nat. Rev. Mater.*, 2024, **9**, 266–281.

167 J. Song, F. Ning, Y. Zuo, A. Li, H. Wang, K. Zhang, T. Yang, Y. Yang, C. Gao, W. Xiao, Z. Jiang, T. Chen, G. Feng and D. Xia, *Adv. Mater.*, 2023, **35**, e2208726.

168 Z. Xu, X. Guo, W. Song, J. Wang, T. Qin, Y. Yuan and J. Lu, *Adv. Mater.*, 2024, **36**, e2303612.

169 C. Zheng, J. Feng, D. Zhang, D. Zhang and J. Li, *ACS Energy Lett.*, 2024, **9**, 1339–1345.

170 K. Wang, J. Qiu, F. Hou, M. Yang, K. Nie, J. Wang, Y. Hou, W. Huang, W. Zhao, P. Zhang, J. Lin, J. Hu, F. Pan and M. Zhang, *Adv. Energy Mater.*, 2023, **13**, 2301216.

171 M. Yoon, Y. Dong, Y. Huang, B. Wang, J. Kim, J.-S. Park, J. Hwang, J. Park, S. J. Kang, J. Cho and J. Li, *Nat. Energy*, 2023, **8**, 482–491.

172 X. Zhao, X. Cao, C. Sheng, L. Xu, P. Wu, Y. Zhou, P. He, Y. Tang and H. Zhou, *ACS Appl. Mater. Interfaces*, 2024, **16**, 24147–24161.

173 J. Z. Wan, C. Ma, J. S. Chen and K. X. Wang, *Small*, 2024, e2408839, DOI: 10.1002/smll.202408839.

174 Z. N. Taylor, A. J. Perez, J. A. Coca-Clemente, F. Braga, N. E. Drewett, M. J. Pitcher, W. J. Thomas, M. S. Dyer, C. Collins, M. Zanella, T. Johnson, S. Day, C. Tang, V. R. Dhanak, J. B. Claridge, L. J. Hardwick and M. J. Rosseinsky, *J. Am. Chem. Soc.*, 2019, **141**, 7333–7346.

175 G. Assat, S. L. Glazier, C. Delacourt and J.-M. Tarascon, *Nat. Energy*, 2019, **4**, 647–656.

176 Q. Jacquet, A. Iadecola, M. Saubanere, H. Li, E. J. Berg, G. Rousse, J. Cabana, M. L. Doublet and J. M. Tarascon, *J. Am. Chem. Soc.*, 2019, **141**, 11452–11464.

177 D. Eum, S. O. Park, H. Y. Jang, Y. Jeon, J. H. Song, S. Han, K. Kim and K. Kang, *Nat. Mater.*, 2024, **23**, 1093–1099.

178 Y. Sun, S. Jiao, J. Wang, Y. Zhang, J. Liu, X. Wang, L. Kang, X. Yu, H. Li, L. Chen and X. Huang, *J. Am. Chem. Soc.*, 2023, **145**, 11717–11726.

179 F. Wu, S. Fang, M. Kuenzel, A. Mullaliu, J.-K. Kim, X. Gao, T. Diemant, G.-T. Kim and S. Passerini, *Joule*, 2021, **5**, 2177–2194.

180 F. Wu, G. T. Kim, T. Diemant, M. Kuenzel, A. R. Schür, X. Gao, B. Qin, D. Alwast, Z. Jusys, R. J. Behm, D. Geiger, U. Kaiser and S. Passerini, *Adv. Energy Mater.*, 2020, **10**, 2001830.

181 Q. Shao, P. Gao, C. Yan, M. Gao, W. Du, J. Chen, Y. Yang, J. Gan, Z. Wu, C. Zhang, G. Chen, X. Zheng, Y. Lin, Y. Jiang, W. Sun, Y. Liu, M. Gao and H. Pan, *Adv. Mater.*, 2022, **34**, e2108543.

182 R. A. House, U. Maitra, M. A. Perez-Osorio, J. G. Lozano, L. Jin, J. W. Somerville, L. C. Duda, A. Nag, A. Walters, K. J. Zhou, M. R. Roberts and P. G. Bruce, *Nature*, 2020, **577**, 502–508.

183 C. Yin, L. Wan, B. Qiu, F. Wang, W. Jiang, H. Cui, J. Bai, S. Ehrlich, Z. Wei and Z. Liu, *Energy Storage Mater.*, 2021, **35**, 388–399.

184 M. M. Rahman, S. McGuigan, S. Li, L. Gao, D. Hou, Z. Yang, Z. Xu, S.-J. Lee, C.-J. Sun, J. Liu, X. Huang, X. Xiao, Y. Chu, S. Sainio, D. Nordlund, X. Kong, Y. Liu and F. Lin, *ACS Energy Lett.*, 2021, **6**, 2882–2890.

185 J. Vergnet, M. Saubanere, M. L. Doublet and J. M. Tarascon, *Joule*, 2020, **4**, 420–434.

186 Y. Zuo, H. Shang, J. Hao, J. Song, F. Ning, K. Zhang, L. He and D. Xia, *J. Am. Chem. Soc.*, 2023, **145**, 5174–5182.

187 D. Eum, H.-Y. Jang, B. Kim, J. Chung, D. Kim, S.-P. Cho, S. H. Song, S. Kang, S. Yu, S.-O. Park, J.-H. Song, H. Kim, O. Tamwattana, D.-H. Kim, J. Lim and K. Kang, *Energy Environ. Sci.*, 2023, **16**, 673–686.

188 B. Zhang, H. Zhang, H. Luo, H. Hua, X. Wu, Y. Chen, S. Zhou, J. Yin, K. Zhang, H.-G. Liao, Q. Wang, Y. Zou, Y. Qiao and S.-G. Sun, *Angew. Chem., Int. Ed.*, 2024, **63**, e202316790.

189 B. Jiang, H. Li, B. Luo, L. Liu, L. Chu, Q. Zhang and M. Li, *Chin. Chem. Lett.*, 2024, **35**, 108649.

190 J. N. Reimers and J. R. Dahn, *J. Electrochem. Soc.*, 1992, **139**, 2091.

191 T. Hu, F. Z. Dai, G. Zhou, X. Wang and S. Xu, *J. Phys. Chem. Lett.*, 2023, **14**, 3677–3684.

192 Y. Lyu, X. Wu, K. Wang, Z. Feng, T. Cheng, Y. Liu, M. Wang, R. Chen, L. Xu, J. Zhou, Y. Lu and B. Guo, *Adv. Energy Mater.*, 2021, **11**, 2000982.

193 J. Li, C. Lin, M. Weng, Y. Qiu, P. Chen, K. Yang, W. Huang, Y. Hong, J. Li, M. Zhang, C. Dong, W. Zhao, Z. Xu, X. Wang, K. Xu, J. Sun and F. Pan, *Nat. Nanotechnol.*, 2021, **16**, 599–605.

194 Z. Chen and J. Dahn, *Electrochem. Solid-State Lett.*, 2003, **6**, A221.

195 W. Kong, D. Zhou, N. De, W. Yang, D. Wong, J. Zhang, Q. Li, J. Yang, C. Schulz and X. Liu, *J. Electrochem. Soc.*, 2021, **168**, 030528.

196 Z. Lin, Y. Ying, Z. Xu, G. Chen, X. Gong, Z. Wang, D. Guan, L. Zhao, M. Yang, K. Fan, T. Liu, H. Li, H. Zhang, H. Li, X. Zhang, Y. Zhu, Z. Lu, Z. Shao, P. Hou and H. Huang, *Energy Environ. Sci.*, 2025, **18**, 334–346.

197 M. Cai, Y. Dong, M. Xie, W. Dong, C. Dong, P. Dai, H. Zhang, X. Wang, X. Sun, S. Zhang, M. Yoon, H. Xu, Y. Ge, J. Li and F. Huang, *Nat. Energy*, 2023, **8**, 159–168.

198 S. Zeng, Y. Zhu, J. Si, H. Liu, Y. Wang, Y. Hu and C. Chen, *J. Power Sources*, 2025, **626**, 235726.

199 X. Tan, Y. Zhang, S. Xu, P. Yang, T. Liu, D. Mao, J. Qiu, Z. Chen, Z. Lu, F. Pan and W. Chu, *Adv. Energy Mater.*, 2023, **13**, 2300147.

200 S.-X. Chen, C.-W. Wang, Y. Zhou, J.-K. Liu, C.-G. Shi, G.-Z. Wei, B.-Y. Yin, H.-T. Deng, S.-Y. Pan, M.-J. Guo, W.-C. Zheng, H.-Z. Wang, Y.-H. Jiang, L. Huang, H.-G. Liao, J.-T. Li and S.-G. Sun, *J. Mater. Chem. A*, 2022, **10**, 5295–5304.

201 J.-N. Zhang, Q.-H. Li, Q. Li, X.-Q. Yu and H. Li, *Chin. Phys. B*, 2018, **27**, 088202.

202 X. Li, L. Zhou, H. Wang, D. Meng, G. Qian, Y. Wang, Y. He, Y. Wu, Z. Hong, Z.-F. Ma and L. Li, *J. Mater. Chem. A*, 2021, **9**, 19675–19680.

203 M. Wen, W. Kong, J. Zhang, Q. Zhang, W. Yin, N. Zhang, K. Chai, Y. Yu, H. Chen and X. Liu, *ACS Energy Lett.*, 2022, **7**, 4185–4189.

204 Y. Yao, Z. Xue, C. Li, J. Li, J. He, X. Zhang and Y. Xiang, *Energy Storage Mater.*, 2024, **71**, 103666.

205 W. Dong, B. Ye, M. Cai, Y. Bai, M. Xie, X. Sun, Z. Lv and F. Huang, *ACS Energy Lett.*, 2023, **8**, 881–888.

206 K. Wu, Q. Li, M. Chen, D. Chen, M. Wu, Z. Hu, F. Li and X. Xiao, *J. Solid State Electrochem.*, 2018, **22**, 3725–3734.

207 S. A. Razek and W.-C. Lee, *Ceram. Int.*, 2023, **49**, 24446–24453.

208 X. Fan and C. Wang, *Chem. Soc. Rev.*, 2021, **50**, 10486–10566.

209 X. Yang, M. Lin, G. Zheng, J. Wu, X. Wang, F. Ren, W. Zhang, Y. Liao, W. Zhao, Z. Zhang, N. Xu, W. Yang and Y. Yang, *Adv. Funct. Mater.*, 2020, **30**, 2004664.

210 X. Fang, Y. Peng, G. Liu, J. Chen, G. Li and X. Dong, *Energy Storage Mater.*, 2025, **74**, 103942.

211 W. Kong, D. Zhou, Q. Zhang, D. Wong, K. An, C. Schulz, N. Zhang, J. Zhang and X. Liu, *Adv. Funct. Mater.*, 2022, **33**, 2211033.

212 D. Kim, J. Hwang, P. Byeon, W. Kim, D. G. Kang, H. B. Bae, S. G. Lee, S. M. Han, J. Lee and S. Y. Chung, *Adv. Mater.*, 2023, **35**, e2212098.

213 Z. Zhu, D. Yu, Z. Shi, R. Gao, X. Xiao, I. Waluyo, M. Ge, Y. Dong, W. Xue, G. Xu, W.-K. Lee, A. Hunt and J. Li, *Energy Environ. Sci.*, 2020, **13**, 1865–1878.

214 J. G. Bae, J. H. Lee, M. S. Kim, B. G. Kim, H. J. Lee and J. H. Lee, *ACS Appl. Mater. Interfaces*, 2023, **15**, 7939–7948.

215 Y. Han, Y. Lei, J. Ni, Y. Zhang, Z. Geng, P. Ming, C. Zhang, X. Tian, J. L. Shi, Y. G. Guo and Q. Xiao, *Small*, 2022, **18**, e2107048.

216 Z. Bi, Z. Yi, A. Zhang, C. Dong, G. Wang, L. Xie, S. Liao, H. Liu, C. Chen and Z.-S. Wu, *Energy Environ. Sci.*, 2024, **17**, 5706–5718.

217 Z. Zhu, H. Wang, Y. Li, R. Gao, X. Xiao, Q. Yu, C. Wang, I. Waluyo, J. Ding, A. Hunt and J. Li, *Adv. Mater.*, 2020, **32**, e2005182.

218 H.-H. Ryu, H.-W. Lim, S. G. Lee and Y.-K. Sun, *Nat. Energy*, 2023, **9**, 47–56.

219 L. Wang, T. Liu, T. Wu and J. Lu, *Nature*, 2022, **611**, 61–67.

220 A. S. Menon, B. J. Johnston, S. G. Booth, L. Zhang, K. Kress, B. E. Murdock, G. Paez Fajardo, N. N. Anthonisamy, N. Tapia-Ruiz, S. Agrestini, M. Garcia-Fernandez, K. Zhou, P. K. Thakur, T. L. Lee, A. J. Nedoma, S. A. Cussen and L. F. J. Piper, *PRX Energy*, 2023, **2**, 013005.

221 B. Cui, Z. Xiao, S. Cui, S. Liu, X. Gao and G. Li, *Electrochem. Energy Rev.*, 2024, **7**, 27.

222 H. Li, L. Wang, Y. Song, Y. Wu, H. Zhang, A. Du and X. He, *Small*, 2023, **19**, e2302208.

223 Q. Sun, X. Liu, L. Chang, Y. Liu, J. Zhang, Y. Yuan, X. Lu and H. Cheng, *ACS Appl. Energy Mater.*, 2024, **7**, 6236–6247.

224 K.-E. Kim, J. Jeong, Y. Lee, H. Lim, K. Y. Chung, H. Kim and S.-O. Kim, *J. Power Sources*, 2024, **601**, 234300.

225 C. Zhao, C. Wang, X. Liu, I. Hwang, T. Li, X. Zhou, J. Diao, J. Deng, Y. Qin, Z. Yang, G. Wang, W. Xu, C. Sun, L. Wu, W. Cha, I. Robinson, R. Harder, Y. Jiang, T. Bicer, J.-T. Li, W. Lu, L. Li, Y. Liu, S.-G. Sun, G.-L. Xu and K. Amine, *Nat. Energy*, 2024, **9**, 345–356.

226 Y. Shao, J. Xu, A. Amardeep, Y. Xia, X. Meng, J. Liu and S. Liao, *Small Methods*, 2024, **8**, e2400256.

227 Q. Fan, Z. Chen, W. Ma and Z. Shi, *Appl. Mater. Today*, 2025, **42**, 102559.

228 C. Li, J. Liu, Y. Su, J. Dong, H. Zhang, M. Wang, Y. Guan, K. Yan, N. Liu, Y. Lu, N. Li, Y. Su, F. Wu and L. Chen, *Energy Storage Mater.*, 2025, **74**, 103893.

229 R. Wang, Y. Zhang, Z. Li, L. Wu, J. Chen, X. Liu, H. Hu, H. Ding, S. Cao, Q. Wei and X. Wang, *J. Energy Chem.*, 2025, **101**, 630–640.

230 U.-H. Kim, S.-T. Myung, C. S. Yoon and Y.-K. Sun, *ACS Energy Lett.*, 2017, **2**, 1848–1854.

231 R. Zhang, C. Wang, P. Zou, R. Lin, L. Ma, L. Yin, T. Li, W. Xu, H. Jia, Q. Li, S. Sainio, K. Kisslinger, S. E. Trask, S. N. Ehrlich, Y. Yang, A. M. Kiss, M. Ge, B. J. Polzin, S. J. Lee, W. Xu, Y. Ren and H. L. Xin, *Nature*, 2022, **610**, 67–73.

232 J. Yang, D. Gao, D. Zhang and C. Chang, *Ceram. Int.*, 2023, **49**, 22294–22303.

233 Y. Li, D. Gao, C. Chang and J. Zheng, *J. Energy Storage*, 2023, **73**, 109139.

234 Z. Xu, X. Chen, W. Fan, M. Zhan, X. Mu, H. Cao, X. Wang, H. Xue, Z. Gao, Y. Liang, J. Liu, X. Tan and F. Pan, *ACS Nano*, 2024, **18**, 33706–33717.

235 J. Li, H. Yang, Q. Deng, W. Li, Q. Zhang, Z. Zhang, Y. Chu and C. Yang, *Angew. Chem., Int. Ed.*, 2024, **63**, e202318042.

236 X. Gao, B. Li, G. Rousse, A. V. Morozov, M. Deschamps, E. Elkaïm, L. Zhang, K. Kummer, A. M. Abakumov and J. M. Tarascon, *Adv. Energy Mater.*, 2024, **15**, 2402793.

237 J. Lu, C. Xu, W. Dose, S. Dey, X. Wang, Y. Wu, D. Li and L. Ci, *Chem. Soc. Rev.*, 2024, **53**, 4707–4740.

238 T. He, Y. Han, B. Shi, J. Wang and H. Yang, *J. Mater. Chem. A*, 2024, **12**, 32593–32612.

239 J. Liu, J. Cao, B. Li, X. Xing and G. Cui, *J. Power Sources*, 2025, **629**, 235966.

240 D. Rathore, C. Geng, N. Zaker, I. Hamam, Y. Liu, P. Xiao, G. A. Botton, J. Dahn and C. Yang, *J. Electrochem. Soc.*, 2021, **168**, 120514.

241 F. Zhang, Y. Guo, C. Li, T. Tan, X. Zhang, J. Zhao, P. Qiu, H. Zhang, Z. Rong, D. Zhu, L. Deng, Z. Ye, Z. Yu, P. Jia, X. Liu, J. Huang and L. Zhang, *J. Energy Chem.*, 2023, **84**, 467–475.

242 L. Cai, Q. Han, H. Zhu, H. Yu, Y. Hu and H. Jiang, *J. Mater. Chem. A*, 2023, **11**, 8352–8358.

243 M. Yoon, Y. Dong, J. Hwang, J. Sung, H. Cha, K. Ahn, Y. Huang, S. J. Kang, J. Li and J. Cho, *Nat. Energy*, 2021, **6**, 362–371.

244 P. Yan, J. Zheng, J. Liu, B. Wang, X. Cheng, Y. Zhang, X. Sun, C. Wang and J.-G. Zhang, *Nat. Energy*, 2018, **3**, 600–605.

245 Y. Bi, J. Tao, Y. Wu, L. Li, Y. Xu, E. Hu, B. Wu, J. Hu, C. Wang, J.-G. Zhang, Y. Qi and J. Xiao, *Science*, 2020, **370**, 1313–1317.

246 G. Qian, Y. Zhang, L. Li, R. Zhang, J. Xu, Z. Cheng, S. Xie, H. Wang, Q. Rao, Y. He, Y. Shen, L. Chen, M. Tang and Z.-F. Ma, *Energy Storage Mater.*, 2020, **27**, 140–149.

247 J. Hu, L. Li, Y. Bi, J. Tao, J. Lochala, D. Liu, B. Wu, X. Cao, S. Chae, C. Wang and J. Xiao, *Energy Storage Mater.*, 2022, **47**, 195–202.

248 Y. K. Sun, Z. Chen, H. J. Noh, D. J. Lee, H. G. Jung, Y. Ren, S. Wang, C. S. Yoon, S. T. Myung and K. Amine, *Nat. Mater.*, 2012, **11**, 942–947.

249 S. E. Renfrew and B. D. McCloskey, *J. Am. Chem. Soc.*, 2017, **139**, 17853–17860.

250 L. A. Kaufman and B. D. McCloskey, *Chem. Mater.*, 2021, **33**, 4170–4176.

251 S.-J. Yang, J.-K. Hu, F.-N. Jiang, X.-B. Cheng, S. Sun, H.-J. Hsu, D. Ren, C.-Z. Zhao, H. Yuan, M. Ouyang, L.-Z. Fan, J.-Q. Huang and Q. Zhang, *eTransportation*, 2023, **18**, 100279.

252 J. Tzadikov, M. Auinat, J. Barrio, M. Volokh, G. Peng, C. Gervais, Y. Ein-Eli and M. Shalom, *ChemSusChem*, 2018, **11**, 2912–2920.

253 X. Ji, N. J. Fritz, H. Jeong, P. Lu, J.-W. Lin, P. V. Braun and D. G. Cahill, *J. Power Sources*, 2024, **614**, 235039.

254 E. W. C. Spotte-Smith, S. Vijay, T. B. Petrocelli, B. L. D. Rinkel, B. D. McCloskey and K. A. Persson, *J. Phys. Chem. Lett.*, 2024, **15**, 391–400.

255 J. Zhang, Q. Guo, S. Liu, C. Zhou, Z. Huang and D. Han, *J. Energy Storage*, 2024, **80**, 110201.

256 K. Homlamai, N. Anansuksawat, T. Sangsanit, S. Prempluem, K. Santisuk, W. Tejangkura and M. Sawangphruk, *J. Power Sources*, 2024, **617**, 235150.

257 T. Zheng, M. Muneeswara, H. Bao, J. Huang, L. Zhang, D. S. Hall, S. T. Boles and W. Jin, *ChemElectroChem*, 2024, **11**, e202400065.

258 K. Luo, M. R. Roberts, R. Hao, N. Guerrini, D. M. Pickup, Y. S. Liu, K. Edstrom, J. Guo, A. V. Chadwick, L. C. Duda and P. G. Bruce, *Nat. Chem.*, 2016, **8**, 684–691.

259 S. E. Renfrew and B. D. McCloskey, *ACS Appl. Energy Mater.*, 2019, **2**, 3762–3772.

260 C. H. Zhang, Y. J. Guo, S. J. Tan, Y. H. Wang, J. C. Guo, Y. F. Tian, X. S. Zhang, B. Z. Liu, S. Xin, J. Zhang, L. J. Wan and Y. G. Guo, *Sci. Adv.*, 2024, **10**, eadl4842.

261 J. Pokharel, A. Cresce, B. Pant, M. Y. Yang, A. Gurung, W. He, A. Baniya, B. S. Lamsal, Z. Yang, S. Gent, X. Xian, Y. Cao, W. A. Goddard, 3rd, K. Xu and Y. Zhou, *Nat. Commun.*, 2024, **15**, 3085.

262 S.-B. Lee, N.-Y. Park, G.-T. Park, U.-H. Kim, S.-J. Sohn, M.-S. Kang, R. M. Ribas, R. S. Monteiro and Y.-K. Sun, *ACS Energy Lett.*, 2024, **9**, 740–747.

263 Z. Liao, Y. Li, X. Yang, X. Li, J. Liu, W. Fu, W. Qiu and X. Zhao, *J. Phys. Chem. C*, 2024, **128**, 10308–10316.

264 H. Huo, M. Jiang, Y. Bai, S. Ahmed, K. Volz, H. Hartmann, A. Henss, C. V. Singh, D. Raabe and J. Janek, *Nat. Mater.*, 2024, **23**, 543–551.

265 Y. Wang, H. Qu, B. Liu, X. Li, J. Ju, J. Li, S. Zhang, J. Ma, C. Li, Z. Hu, C. K. Chang, H. S. Sheu, L. Cui, F. Jiang, E. R. H. van Eck, A. P. M. Kentgens, G. Cui and L. Chen, *Nat. Commun.*, 2023, **14**, 669.

266 N. Xu, J. Shi, G. Liu, X. Yang, J. Zheng, Z. Zhang and Y. Yang, *J. Power Sources Adv.*, 2021, **7**, 100043.

267 P. Janssen, J. Kasnatscheew, B. Streipert, C. Wendt, P. Murmann, M. Ponomarenko, O. Stubbmann-Kazakova, G.-V. Röschenthaler, M. Winter and I. Cekic-Laskovic, *J. Electrochem. Soc.*, 2018, **165**, A3525–A3530.

268 G. X. Li, P. Lennartz, V. Koverga, R. Kou, A. Nguyen, H. Jiang, M. Liao, D. Wang, N. Dandu, M. Zepeda, H. Wang, K. Wang, A. T. Ngo, G. Brunklaus and

D. Wang, *Proc. Natl. Acad. Sci. U. S. A.*, 2024, **121**, e2311732121.

269 T. Naren, G. C. Kuang, R. Jiang, P. Qing, H. Yang, J. Lin, Y. Chen, W. Wei, X. Ji and L. Chen, *Angew. Chem., Int. Ed.*, 2023, **62**, e202305287.

270 Y. Feng, Y. Li, J. Lin, H. Wu, L. Zhu, X. Zhang, L. Zhang, C. F. Sun, M. Wu and Y. Wang, *Nat. Commun.*, 2023, **14**, 3639.

271 Z. Y. Jiang, H. B. Li, Z. G. Qu and J. F. Zhang, *Int. J. Hydrogen Energy*, 2022, **47**, 9428–9459.

272 Y. Sun, D. Ren, G. Liu, D. Mu, L. Wang, B. Wu, J. Liu, N. Wu and X. He, *Int. J. Energy Res.*, 2021, **45**, 20867–20877.

273 H. Li, H. Wang, Z. Xu, K. Wang, M. Ge, L. Gan, Y. Zhang, Y. Tang and S. Chen, *Small*, 2021, **17**, e2103679.

274 X. Feng, D. Ren, X. He and M. Ouyang, *Joule*, 2020, **4**, 743–770.

275 S.-J. Tan, J. Yue, Y.-F. Tian, Q. Ma, J. Wan, Y. Xiao, J. Zhang, Y.-X. Yin, R. Wen and S. Xin, *Energy Storage Mater.*, 2021, **39**, 186–193.

276 H. K. Hu, W. D. Xue, Y. Li and P. Jiang, *Acta Polym. Sin.*, 2022, **53**, 457–473.

277 T. Tsujikawa, K. Yabuta, T. Matsushita, T. Matsushima, K. Hayashi and M. Arakawa, *J. Power Sources*, 2009, **189**, 429–434.

278 H. Nakagawa, Y. Fujino, S. Kozono, Y. Katayama, T. Nukuda, H. Sakaebe, H. Matsumoto and K. Tatsumi, *J. Power Sources*, 2007, **174**, 1021–1026.

279 S. Abada, G. Marlair, A. Lecocq, M. Petit, V. Sauvant-Moynot and F. Huet, *J. Power Sources*, 2016, **306**, 178–192.

280 Y. Wang, X. Feng, W. Huang, X. He, L. Wang and M. Ouyang, *Adv. Energy Mater.*, 2023, **13**, 2203841.

281 H.-Z. Jin, X.-F. Han, P. M. Radjenovic, J.-H. Tian and J.-F. Li, *J. Phys. Chem. C*, 2021, **125**, 1761–1766.

282 W. Ji, F. Wang, D. Liu, J. Qian, Y. Cao, Z. Chen, H. Yang and X. Ai, *J. Mater. Chem. A*, 2016, **4**, 11239–11246.

283 H. Zhong, C. Kong, H. Zhan, C. Zhan and Y. Zhou, *J. Power Sources*, 2012, **216**, 273–280.

284 Y. Zhang, F. Liang, S. Li, C. Zhang, S. Zhang, X. Liu, S. Zhao, S. Yang, Y. Xia, J. Lin, B. Guo, H. Cheng, M. Wang, M. Jiang and D. Wang, *Int. J. Energy Res.*, 2022, **46**, 11529–11555.

285 R. Mahamud and C. Park, *Energies*, 2022, **15**, 3930.

286 J. Wang, R. Chen, L. Yang, M. Zan, P. Chen, Y. Li, W. Li, H. Yu, X. Yu, X. Huang, L. Chen and H. Li, *Adv. Mater.*, 2022, **34**, e2200655.

287 X. Liu, X. Zhou, Q. Liu, J. Diao, C. Zhao, L. Li, Y. Liu, W. Xu, A. Daali, R. Harder, I. K. Robinson, M. Dahbi, J. Alami, G. Chen, G. L. Xu and K. Amine, *Adv. Mater.*, 2022, **34**, e2107326.

288 M. Cianciullo, G. Vilardi, B. Mazzarotta and R. Bubbico, *Energies*, 2022, **15**, 4169.

289 C. G. Shi, X. Peng, P. Dai, P. Xiao, W. C. Zheng, H. Y. Li, H. Li, S. Indris, S. Mangold, Y. H. Hong, C. X. Luo, C. H. Shen, Y. M. Wei, L. Huang and S. G. Sun, *Adv. Energy Mater.*, 2022, **12**, 2200569.

290 G.-L. Xu, Q. Liu, K. K. S. Lau, Y. Liu, X. Liu, H. Gao, X. Zhou, M. Zhuang, Y. Ren, J. Li, M. Shao, M. Ouyang, F. Pan, Z. Chen, K. Amine and G. Chen, *Nat. Energy*, 2019, **4**, 484–494.

291 C. H. Shen, Q. Wang, F. Fu, L. Huang, Z. Lin, S. Y. Shen, H. Su, X. M. Zheng, B. B. Xu, J. T. Li and S. G. Sun, *ACS Appl. Mater. Interfaces*, 2014, **6**, 5516–5524.

292 Q. Gu, J. A. Kimpton, H. E. A. Brand, Z. Wang and S. Chou, *Adv. Energy Mater.*, 2017, **7**, 1602831.

293 H. Wang, D. Ning, L. Wang, H. Li, Q. Li, M. Ge, J. Zou, S. Chen, H. Shao, Y. Lai, Y. Zhang, G. Xing, W. K. Pang and Y. Tang, *Small*, 2022, **18**, e2107491.

294 H. Liu, Y. Chen, S. Hy, K. An, S. Venkatachalam, D. Qian, M. Zhang and Y. S. Meng, *Adv. Energy Mater.*, 2016, **6**, 1502143.

295 C. Wang, R. Wang, Z. Huang, M. Chu, W. Ji, Z. Chen, T. Zhang, J. Zhai, H. Lu, S. Deng, J. Chen, L. He, T. Liang, F. Wang, J. Wang, Y. Deng, W. Cai and Y. Xiao, *Energy Storage Mater.*, 2022, **44**, 1–9.

296 W. Song, M. A. Pérez-Osorio, J.-J. Marie, E. Liberti, X. Luo, C. O'Leary, R. A. House, P. G. Bruce and P. D. Nellist, *Joule*, 2022, **6**, 1049–1065.

297 P. Yan, J. Zheng, Z. K. Tang, A. Devaraj, G. Chen, K. Amine, J. G. Zhang, L. M. Liu and C. Wang, *Nat. Nanotechnol.*, 2019, **14**, 602–608.

298 M. Freire, N. V. Kosova, C. Jordy, D. Chateigner, O. I. Lebedev, A. Maignan and V. Pralong, *Nat. Mater.*, 2016, **15**, 173–177.

299 R. Yu, W. Zeng, L. Zhou, G. Van Tendeloo, L. Mai, Z. Yao and J. Wu, *Cell Rep. Phys. Sci.*, 2023, **4**, 101480.

300 Y. Gong, J. Zhang, L. Jiang, J. A. Shi, Q. Zhang, Z. Yang, D. Zou, J. Wang, X. Yu, R. Xiao, Y. S. Hu, L. Gu, H. Li and L. Chen, *J. Am. Chem. Soc.*, 2017, **139**, 4274–4277.

301 X. Cao, H. Li, Y. Qiao, M. Jia, X. Li, J. Cabana and H. Zhou, *Adv. Mater.*, 2021, **33**, e2004280.

302 O. Pecher, J. Carretero-González, K. J. Griffith and C. P. Grey, *Chem. Mater.*, 2016, **29**, 213–242.

303 C. Li, C. Zhao, B. Hu, W. Tong, M. Shen and B. Hu, *Chem. Mater.*, 2020, **32**, 1054–1063.

304 F. Blanc, M. Leskes and C. P. Grey, *Acc. Chem. Res.*, 2013, **46**, 1952–1963.

305 J. Zhang, Q. Wang, S. Li, Z. Jiang, S. Tan, X. Wang, K. Zhang, Q. Yuan, S. J. Lee, C. J. Titus, K. D. Irwin, D. Nordlund, J. S. Lee, P. Pianetta, X. Yu, X. Xiao, X. Q. Yang, E. Hu and Y. Liu, *Nat. Commun.*, 2020, **11**, 6342.

306 E. McCalla, M. T. Sougrati, G. Rousse, E. J. Berg, A. Abakumov, N. Recham, K. Ramesha, M. Sathiya, R. Dominko, G. Van Tendeloo, P. Novak and J. M. Tarascon, *J. Am. Chem. Soc.*, 2015, **137**, 4804–4814.

307 J. Xu, M. Sun, R. Qiao, S. E. Renfrew, L. Ma, T. Wu, S. Hwang, D. Nordlund, D. Su, K. Amine, J. Lu, B. D. McCloskey, W. Yang and W. Tong, *Nat. Commun.*, 2018, **9**, 947.

308 A. Devaraj, M. Gu, R. Colby, P. Yan, C. M. Wang, J. M. Zheng, J. Xiao, A. Genc, J. G. Zhang, I. Belharouak, D. Wang, K. Amine and S. Thevuthasan, *Nat. Commun.*, 2015, **6**, 8014.

309 J. Wang, Y. C. Chen-Wiegart and J. Wang, *Angew. Chem., Int. Ed.*, 2014, **53**, 4460–4464.

310 L. G. Wang, J. J. Wang and P. J. Zuo, *Small Methods*, 2018, **2**, 1700293.

311 J. Wang, Y. C. Chen-Wiegart and J. Wang, *Nat. Commun.*, 2014, **5**, 4570.

312 A. Jena, C.-H. Lee, W. K. Pang, V. K. Peterson, N. Sharma, C.-C. Wang, Y.-F. Song, C.-C. Lin, H. Chang and R.-S. Liu, *Electrochim. Acta*, 2017, **236**, 10–17.

313 L. Wang, T. Liu, A. Dai, V. De Andrade, Y. Ren, W. Xu, S. Lee, Q. Zhang, L. Gu, S. Wang, T. Wu, H. Jin and J. Lu, *Nat. Commun.*, 2021, **12**, 5370.

314 P. E. Pearce, A. J. Perez, G. Rousse, M. Saubanere, D. Batuk, D. Foix, E. McCalla, A. M. Abakumov, G. Van Tendeloo, M. L. Doublet and J. M. Tarascon, *Nat. Mater.*, 2017, **16**, 580–586.

315 G. Assat, D. Foix, C. Delacourt, A. Iadecola, R. Dedryvere and J. M. Tarascon, *Nat. Commun.*, 2017, **8**, 2219.

316 Y. Qiao, S. Guo, K. Zhu, P. Liu, X. Li, K. Jiang, C.-J. Sun, M. Chen and H. Zhou, *Energy Environ. Sci.*, 2018, **11**, 299–305.

317 Q. Li, Y. Qiao, S. Guo, K. Jiang, Q. Li, J. Wu and H. Zhou, *Joule*, 2018, **2**, 1134–1145.

318 K. Shimoda, T. Minato, K. Nakanishi, H. Komatsu, T. Matsunaga, H. Tanida, H. Arai, Y. Ukyo, Y. Uchimoto and Z. Ogumi, *J. Mater. Chem. A*, 2016, **4**, 5909–5916.

319 X. Li, Y. Qiao, S. Guo, Z. Xu, H. Zhu, X. Zhang, Y. Yuan, P. He, M. Ishida and H. Zhou, *Adv. Mater.*, 2018, **30**, e1705197.

320 M. Tang, A. Dalzini, X. Li, X. Feng, P. H. Chien, L. Song and Y. Y. Hu, *J. Phys. Chem. Lett.*, 2017, **8**, 4009–4016.

321 G. Ou, Y. Xu, B. Wen, R. Lin, B. Ge, Y. Tang, Y. Liang, C. Yang, K. Huang, D. Zu, R. Yu, W. Chen, J. Li, H. Wu, L. M. Liu and Y. Li, *Nat. Commun.*, 2018, **9**, 1302.

322 B. Qiu, M. Zhang, L. Wu, J. Wang, Y. Xia, D. Qian, H. Liu, S. Hy, Y. Chen, K. An, Y. Zhu, Z. Liu and Y. S. Meng, *Nat. Commun.*, 2016, **7**, 12108.

323 B. Xu, C. R. Fell, M. Chi and Y. S. Meng, *Energy Environ. Sci.*, 2011, **4**, 2223–2233.

324 J. Evans, *X-ray absorption spectroscopy for the chemical and materials sciences*, John Wiley & Sons, 2018.

325 J. Yano and V. K. Yachandra, *Photosynth. Res.*, 2009, **102**, 241–254.

326 K. Chai, J. Zhang, Q. Li, D. Wong, L. Zheng, C. Schulz, M. Bartkowiak, D. Smirnov and X. Liu, *Small*, 2022, **18**, e2201014.

327 G. Assat, A. Iadecola, C. Delacourt, R. Dedryvère and J.-M. Tarascon, *Chem. Mater.*, 2017, **29**, 9714–9724.

328 H. Koga, L. Croguennec, M. Ménétrier, P. Mannessiez, F. Weill, C. Delmas and S. Belin, *J. Phys. Chem. C*, 2014, **118**, 5700–5709.

329 X. Yu, Y. Lyu, L. Gu, H. Wu, S.-M. Bak, Y. Zhou, K. Amine, S. N. Ehrlich, H. Li, K.-W. Nam and X.-Q. Yang, *Adv. Energy Mater.*, 2014, **4**, 1300950.

330 S. Hy, J.-H. Cheng, J.-Y. Liu, C.-J. Pan, J. Rick, J.-F. Lee, J.-M. Chen and B. J. Hwang, *Chem. Mater.*, 2014, **26**, 6919–6927.

331 S. Hy, W.-N. Su, J.-M. Chen and B.-J. Hwang, *J. Phys. Chem. C*, 2012, **116**, 25242–25247.

332 M. Oishi, C. Yogi, I. Watanabe, T. Ohta, Y. Orikasa, Y. Uchimoto and Z. Ogumi, *J. Power Sources*, 2015, **276**, 89–94.

333 R. Qiao, Y. Wang, P. Olalde-Velasco, H. Li, Y.-S. Hu and W. Yang, *J. Power Sources*, 2015, **273**, 1120–1126.

334 W. Yang and T. P. Devereaux, *J. Power Sources*, 2018, **389**, 188–197.

335 F. Ning, B. Li, J. Song, Y. Zuo, H. Shang, Z. Zhao, Z. Yu, W. Chu, K. Zhang, G. Feng, X. Wang and D. Xia, *Nat. Commun.*, 2020, **11**, 4973.

336 P. Zhong, Z. Cai, Y. Zhang, R. Giovine, B. Ouyang, G. Zeng, Y. Chen, R. Clément, Z. Lun and G. Ceder, *Chem. Mater.*, 2020, **32**, 10728–10736.

337 B. Kim, J. H. Song, D. Eum, S. Yu, K. Oh, M. H. Lee, H. Y. Jang and K. Kang, *Nat. Sustainability*, 2022, **5**, 708–716.

338 C. Lv, X. Zhou, L. Zhong, C. Yan, M. Srinivasan, Z. W. Seh, C. Liu, H. Pan, S. Li, Y. Wen and Q. Yan, *Adv. Mater.*, 2021, **34**, e2101474.

339 T. Lombardo, M. Duquesnoy, H. El-Bouysidy, F. Aren, A. Gallo-Bueno, P. B. Jorgensen, A. Bhowmik, A. Demortiere, E. Ayerbe, F. Alcaide, M. Reynaud, J. Carrasco, A. Grimaud, C. Zhang, T. Vegge, P. Johansson and A. A. Franco, *Chem. Rev.*, 2022, **122**, 10899–10969.

340 D. D. Sarma, J.-H. Sim, J.-M. Tarascon and S. Biermann, 2023, DOI: **10.48550/arXiv.2305.08526**.

341 Z. Yao, Y. Lum, A. Johnston, L. M. Mejia-Mendoza, X. Zhou, Y. Wen, A. Aspuru-Guzik, E. H. Sargent and Z. W. Seh, *Nat. Rev. Mater.*, 2023, **8**, 202–215.